Fall 12-2021

Space Charge Effects in Low Energy Magnetized Electron Beams

W. M. Sajini Anushika Kumari Wijethunga
Old Dominion University, wwije001@odu.edu

SPACE CHARGE EFFECTS IN LOW ENERGY MAGNETIZED ELECTRON BEAMS

by

W. M. Sajini Anushika Kumari Wijethunga
B.S. May 2015, University of Peradeniya, Sri Lanka
M.S. May 2017, Old Dominion University

A Dissertation Submitted to the Faculty of
Old Dominion University in Partial Fulfillment of the
Requirements for the Degree of

DOCTOR OF PHILOSOPHY

PHYSICS

OLD DOMINION UNIVERSITY
December 2021

Approved by:

Jean R. Delayen (Director)

Geoffrey A. Krafft (Member)

Riad Suleiman (Member)

Sebastian E. Kuhn (Member)

Helmut Baumgart (Member)

ABSTRACT

SPACE CHARGE EFFECTS IN LOW ENERGY MAGNETIZED ELECTRON BEAMS

W. M. Sajini Anushika Kumari Wijethunga
Old Dominion University, 2021
Director: Dr. Jean R. Delayen

Magnetized electron cooling of the ion beam is one of the major approaches towards obtaining the required high luminosity in the proposed Electron-Ion Collider (EIC). To increase the cooling efficiency, a bunched electron beam with a high bunch charge and high repetition rate is required. However, these features can combine to enhance the collective interactions, such as the space charge effect. A magnetized electron beam was successfully generated at the Thomas Jefferson National Accelerator Facility (JLab) using a compact, 300 kV DC high voltage photo-gun with an inverted insulator geometry and bi-alkali antimonide photocathode. The beam magnetization was characterized using a modest diagnostic beamline to measure beam sizes, rotation angles, and normalized transverse emittance as a function of magnetic field at the photocathode, laser spot size, and gun high-voltage. Simultaneously, simulations were performed using the A Space Charge Tracking Algorithm (ASTRA) and General Particle Tracer (GPT) programs. Further, sustained high average current magnetized beam up to 28 mA was demonstrated, and the photocathode lifetime for different magnetized electron beam currents was investigated. In the second part of the project, the space charge effect in low-energy magnetized electron beams was studied and compared with GPT simulations. The high bunch charge studies showed evidence of space charge current limitations starting at 0.3 nC and limited the maximum delivered bunch charge to 0.7 nC. To reach the high bunch charge goal of a few nC, the existing DC photo-gun design was modified using CST Studio Suite's electromagnetic field solver, and a way to cancel the beam deflection exerted by the non-symmetric nature of the inverted insulator photo-gun geometry was discovered. This thesis presents a detailed description of the generation, characterization, and simulation of high current, high bunch charge magnetized electron beams at JLab, as well as the modified photo-gun design. Together with measurements and simulations, the purpose of this thesis is to provide a solid background on the theoretical aspects and the experimental challenges associated with magnetized electron beams for accelerator applications.

To amma and appachchi.

ACKNOWLEDGMENTS

I would first like to express my sincere gratitude to my supervisor, Prof. Jean Delayen, for accepting me as a student and his guidance and encouragement throughout my Ph.D. journey. I am very grateful to Prof. Geoffrey Krafft for introducing me to the Jefferson Lab's Center for Injectors and Sources (CIS) group and his constant guidance during this research.

A huge thanks goes to my Jefferson Lab mentor, Dr. Riad Suleiman, for always being there for me. Without his guidance and support, this project would not be a success. Also, I express my sincere gratitude to Dr. Md Abdullah Mamun for helping me with the measurements and sharing his knowledge and ideas throughout my thesis project.

A special thanks goes to Dr. Carlos Hernandez-Garcia for his willingness to share his expertise with me in high voltage conditioning, designing the photo-gun components, fabrication, and assembly, and Dr. Fay Hannon for introducing me to beam dynamic simulations and assistance in troubleshooting the problems. Also, I would like to extend my sincere gratitude to Dr. Shukui Zhang for helping me with the new laser system for high bunch charge operations. Also, I owe a special thanks to Dr. Matt Poelker for his advice and always encouraging words.

My sincere thanks also goes to Dr. Yan Wang for sharing his knowledge and experience with me, Dr. Jay Benesch for providing me solenoid field maps for my simulation work, Dr. Gabriel Palacios-Serrano for generating the 3D CST model for the GTS photo-gun, and his friendship, and Mr. Don Bullard for teaching me electrode polishing and sharing his knowledge and experience on gun assembly. I would also like to extend my sincere gratitude to Dr. Joe Grames, the head of the CIS group, and all the members of the CIS group and technicians for their support to make this project a success. It has been an honor to work with the Jefferson Lab gun group.

I would also like to thank my committee members, Prof. Sebastian Kuhn and Prof. Helmut Baumgart. They were always available when I needed their help and advice.

I am extremely thankful to the Physics Department at Old Dominion University, especially Prof. Lepsha Vuskovic and Ms. Lisa Okun, for their continuous support not only on academics but also on a personal level.

A special thanks goes to Dr. Subashini De Silva for always being there for me as a sister and my dear friend Jayendrika Tiskumara for her endless support since my very first day in the USA. Also, I would like to thank all my Sri Lankan friends for their immense support

and for making my stay in Virginia enjoyable.

I am sincerely thankful to Dr. Salvador Sosa, Victoria Lagerquist, Josh Yoskowitz, and all my friends at Old Dominion University and Center for Accelerator Science (CAS) for their help and support throughout my Ph.D. journey.

Finally, I want to express my sincere gratitude to my parents for letting me pursue my dreams. Without their tremendous understanding, unconditional love, and encouragement, it would be impossible for me to reach my goals.

This work is supported by the Department of Energy under contract DE-AC05-06OR23177. Additional support came from Laboratory Directed Research and Development program and JSA initiatives fund program.

TABLE OF CONTENTS

Page

LIST OF TABLES

LIST OF FIGURES

Figure Page

Figure Page

Figure Page

Figure Page

Figure Page

Figure Page

Figure Page

CHAPTER 1

INTRODUCTION

The proposed high-energy, high-luminosity, polarized Electron-Ion Collider (EIC) is one of the highest priorities for new accelerator facilities to support the United States nuclear physics research to gain a deeper understanding of matter and fundamental forces. Specifically, how do protons get their mass and spin from their constituent quarks and gluons? How are quarks and gluons distributed inside atomic nuclei? How are protons and neutrons bound in nuclei? How closely can gluons be packed before they reach saturation? What are the properties of dense gluonic matter?[1] The facility will contain two intersecting accelerator rings: one containing an intense beam of polarized electrons and the other a high-energy beam of polarized protons or heavier atomic nuclei, which are steered into head-on collisions. The facility is planned to be designed and constructed over the next ten years at Brookhaven National Laboratory (BNL). Thomas Jefferson National Accelerator Facility (JLab) plays a significant role in conducting various R&D projects on several novel accelerator technologies to support the design and construction. Generation and characterization of a magnetized bunched electron beam from a DC photo-gun for ion beam cooling is one such laboratory directed R&D (LDRD) project on which this dissertation is based.

One of the critical requirements of the proposed collider design is to obtain ultra-high luminosity, exceeding 10^{33} cm^{-2}s^{-1} at the colliding point, which is a few hundred times larger than the luminosity achieved so far by the Hadron-Electron Ring Accelerator (HERA) in Germany. According to the following equation

$$L = \frac{1}{2\pi} f N_b \frac{N_1 N_2}{\sqrt{\sigma_{1x}^2 + \sigma_{2x}^2}\ \sqrt{\sigma_{1y}^2 + \sigma_{2y}^2}}, \tag{1}$$

where N_1, N_2 are the number of particles per bunch, N_b is the number of bunches, f is the repetition frequency, σ_x, σ_y are the beam sizes of the two colliding beams respectively with $\sigma_{1x} \neq \sigma_{2x}$, $\sigma_{1y} \neq \sigma_{2y}$ and assuming approximately equal bunch lengths $\sigma_{1s} = \sigma_{2s}$ [2], high luminosity can be achieved with high bunch charge and small beam sizes (small transverse emittance) of both colliding electron and ion beams together with high bunch repetition rate. In order to obtain this small transverse emittance (less momentum spread in the ion beam), a process called "beam cooling" is used. Cooling can be explained as

a reduction of the 6D phase space volume occupied by the beam (for the same number of particles), or similarly, a reduction in the random motion of the beam. There are a few different cooling mechanisms: electron cooling (magnetized electron cooling), stochastic cooling, coherent electron cooling (CeC), micro-bunching cooling, optical stochastic cooling, ionization cooling, and laser cooling [3].

The proposed EIC cooler design requires strong hadron cooling of hadrons up to a TeV in energy in less than an hour of cooling time. It has being a challenging task to achieve these requirements because the traditional beam cooling methods are not effective for hadron beams in the TeV energy range, and ordinary electron cooling, which has successfully cooled hadron beams below 10 GeV, is ineffective at the TeV scale [3]. However, several accelerator groups have been considering several concepts to reach this goal. Thus far, CeC, which is being explored at BNL, and magnetized electron cooling, which is being considered at JLab, have become promising concepts.

G.I. Budker invented electron cooling in 1965 to increase the luminosity of hadron colliders. The idea behind this is when an electron beam with temperature T_e is co-propagated with an ion beam with temperature T_i with $T_e < T_i$ and similar velocities, Coulomb collisions between ions and electrons lead to a transfer of thermal energy from ions to the electrons. Thermal equilibrium is reached when both particles have the same transverse momentum. Hence, in equilibrium the lighter electrons have higher transverse velocities and slow down the heavy ions, which reduces the transverse emittance. The electron cooling method was successfully tested in 1974 at NAP-M (Russian acronym for Antiproton Accumulator Model) with low-energy non-relativistic protons [4, 5]. In 2005, Fermilab demonstrated relativistic electron cooling of 8.9 GeV/c antiprotons at its Recycler facility with 4.3 MeV electron beam [6]. BNL has recently demonstrated the world's first bunched-beam electron cooling of Au ions of energy 4.6 GeV/nucleon at its Low Energy Relativistic Heavy Ion Collider (RHIC) electron Cooler (LEReC) facility with electron beams of energy 1.6 - 2.6 MeV occupying RF acceleration[7].

In 1977, Y. Derbenev discovered that the electron cooling efficiency could increase up to two orders of magnitude if the process occurs inside a uniform magnetic field, a process known as "magnetized electron cooling" [8, 9]. The basic principle is as follows: when an electron beam travels through a long solenoid magnet through which the ion beam passes, it forces the electrons to follow small helical trajectories. This motion favors increasing the electron-ion interaction time while suppressing the electron-ion recombination, which is a severe problem, especially for heavy ions. Cooling rates of a magnetized electron beam

are ultimately determined by electron longitudinal energy spread rather than transverse emittance as the transverse motion of the electrons is quenched by the strong magnetic field.

However, delivering the electron beam into the cooling solenoid represents a significant challenge. The radial fringe field at the entrance of the cooling solenoid exerts a large transverse momentum onto the electron beam making it impossible to obtain the desired electron beam trajectory inside the solenoid. The ill effects of the fringe field can be canceled if the electron beam is born in a similar solenoid field and passing through a fringe field at the exit of the photo-gun that produces a beam motion with equal transverse momentum but of opposite sign, such that the two fringe-field effects cancel [10].

Figure 1 shows the transportation of the magnetized electron beam from its generation to the cooling solenoid.

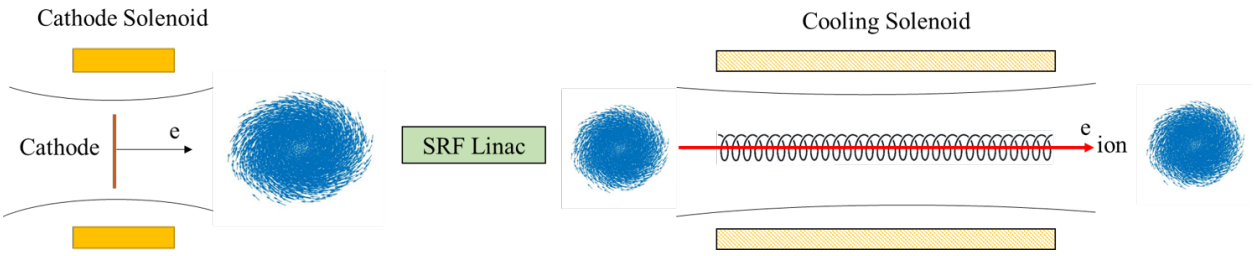

FIG. 1: Illustration of the beamline from generation of the magnetized beam to the cooling solenoid.

So far, the Fermilab Accelerator Science and Technology (FAST) facility has successfully demonstrated the production of a magnetized electron beam (canonical-angular-momentum (CAM) dominated beam) using a 50 MeV RF photo-gun at a low average current with a solenoid providing a strong axial magnetic field at the photocathode. The system includes a superconducting 300 MeV electron linac [11, 12]. Their work mainly focuses on removing the CAM from the electron distribution via round-to-flat beam (RTFB) transformation using sets of skew-quadrupole magnets. RTFB transforms the beam eigen-emittances to the conventional emittances along each transverse degree of freedom, yielding a beam with

an asymmetric transverse emittance of a large aspect ratio. Further, the transverse emittance and the magnetization were measured by implementing multi-slit and quadrupole scan techniques [13].

Conversely, hadron cooling requires a very high average current, high bunch charge (100 mA average current with nanoCoulomb (nC) bunch charge) unpolarized electron beam with low emittance and long lifetime. Delivering a high average current, high bunch charge electron beam has been one of the main goals and challenging tasks for many accelerator facilities around the world, mainly due to space charge effects, its current limitations and subsequently the degradation of the beam quality, and increase in beam instability.

There are four different electron guns to be considered for high average current, high bunch charge delivery: a normal conducting RF gun (with a photocathode or gridded thermionic cathode), a superconducting radio frequency (SRF) gun, a DC high-voltage gun (with downstream bunching, or rf-pulsed gridded thermionic emitter), and a DC high-voltage photo-gun.

In general, RF guns are used for pulsed-rf applications. They are more complicated and expensive compared to DC guns. One issue with operating normal conducting RF guns in CW mode is the thermal heat load management. SRF guns promise CW operation with high average current and beam energy, but have had no success in achieving the desired high average current. Further, SRF guns cannot be utilized for magnetized electron beam generation, as the magnetic field at the photocathode can affect the superconducting condition of the SRF cavity due to the Meissner effect. A DC high-voltage rf-pulsed gridded thermionic gun is a viable option. On the other hand, photo-guns have great flexibility over bunch charge, repetition rates, bunch length, and energy compared to thermionic guns, making them the best choice for high-performance accelerators. However, DC high-voltage photo-guns have two drawbacks: field emission at high bias voltage, which leads to ion back bombardment, and the reliance on a relatively delicate photocathode [14]. Several accelerator groups have been working on different photocathode materials and fabrication techniques for overcome this issues (JLab: GaAs, Cs_xK_ySb, Cornell: GaAs, GaN, GaAsP, CsK_2Sb, and Cs_3Sb) [15].

Until recently, RF photo-guns were known to be providing the best beam quality and beam parameters with the highest average current of 32 mA. Recent work at JLab and Cornell University has shown that DC high-voltage photo-guns followed by superconducting accelerating cavities produce beams as good as or better than RF guns with similar parameters [15]. The DC gun used for the Jefferson Lab Free-Electron Laser (FEL) has reliably provided 135 pC bunches at an average current of 9 mA for many years. Cornell University

holds the world record for high average current, 65 mA with nC bunch charge, but not simultaneously [15]. BNL also has made significant progress in generating 30 mA electron beams for the LEReC program [16].

1.1 RESEARCH GOALS AND OBJECTIVES

The initial focus of this research was to generate, characterize, and simulate the magnetized bunch electron beam from a DC gun with high average current, high bunch charge, and high repetition rate as a part of the JLab proposed EIC (JLEIC) cooler project to achieve its promised ultra-high luminosity. Table 1 lists the magnetized electron beam specifications for the JLEIC cooler design.

TABLE 1: The magnetized electron beam requirements of JLEIC cooler.

Parameter	JLEIC requirement
Bunch charge [nC]	3.2
Average current [mA]	140 (at 400 kV)
Repetition rate [MHz]	43.3
Transverse normalized emittance [mm mrad]	<19
Normalized drift emittance [mm mrad]	36
Cathode spot radius - flat top [mm]	3.1
Bunch length - flat top [ps]	60
Magnetic field at the cathode [kG]	0.5

In order to reach the above goals, the initial research objectives were set as follows:

1. Generate magnetized electron beams using a compact 300 kV DC high-voltage photogun with an inverted insulator geometry and alkali-antimonide photocathodes.

2. Characterize the magnetized beam by measuring the beam size and rotation angle variation as a function of the cathode magnetic field and benchmark them against the simulations.

3. Study the transverse emittance associated with the magnetized beam (correlated/drift emittance) by measuring and simulating the emittance by varying the cathode magnetic field for various laser spot sizes.

4. Deliver high current magnetized electron beams and investigate the photocathode lifetime for different magnetized electron beam currents.

5. Deliver magnetized electron beams with high bunch charge.

The second part of the project focuses on investigating the space charge effect in low energy magnetized beams as a function of magnetic field strength, gun high-voltage, laser pulse width, and spot size and comparing the results with simulations.

However, experiments performed at high bunch charge showed evidence of space charge current limitations starting at 0.3 nC, which reduces the maximum delivered bunch charge to 0.7 nC. The low extracted charge is mainly due to the modest longitudinal electric field (E_z) at the photocathode as well as beam loss. Hence, re-designing of the existing DC photo-gun to reach the few nC high bunch charge goal was the final objective.

Although the the BNL's eRHIC design was selected over JLEIC design for the future EIC project, successful demonstration of these goals will still be significant for many accelerator applications with magnetized beam, high average current, and high bunch charge, including the eRHIC upgrades.

1.2 ORGANIZATION OF THE DISSERTATION

This dissertation is organized in the following way: Chapter 2 describes the magnetized electron source at JLab, which includes a gun high voltage chamber, photocathode preparation chamber, drive laser, cathode solenoid, and a diagnostic beamline. Chapter 3 discusses the theoretical background, namely, the basic concepts of accelerator physics, linear beam dynamics, and derivations of some of the formalism used in this dissertation. Chapter 4 discusses the theoretical background of the space charge effect and space charge current limitations related to this dissertation. Chapter 5 presents the characterization of the magnetized electron beam with detailed experimental methods, simulation techniques, results analysis, and error analysis. It includes beam size, rotation angle, drift emittance variations with the cathode magnetic field, angular momentum conservation, and high current run results. Further, it includes the findings related to the experiment, which helped benchmark the simulations against the experimental results. Chapter 6 discusses the characterization of the space charge dominated magnetized electron beam as a function of cathode magnetic field, gun voltage, and beam dimensions compared to simulations. Chapter 7 discusses the re-design of the photo-gun for high bunch charge operations. This chapter contains two subsections that explain the existing gun design and modified gun design. Chapter 8 present the summary of the results, conclusions, and future work.

CHAPTER 2

MAGNETIZED ELECTRON SOURCE

The prototype magnetized electron source is located at the Gun Test Stand (GTS) inside the Low Energy Recirculator Facility (LERF) building at JLab. Figure 2 illustrates the main components of the beamline and Fig. 3 shows the photographs of the beamline.

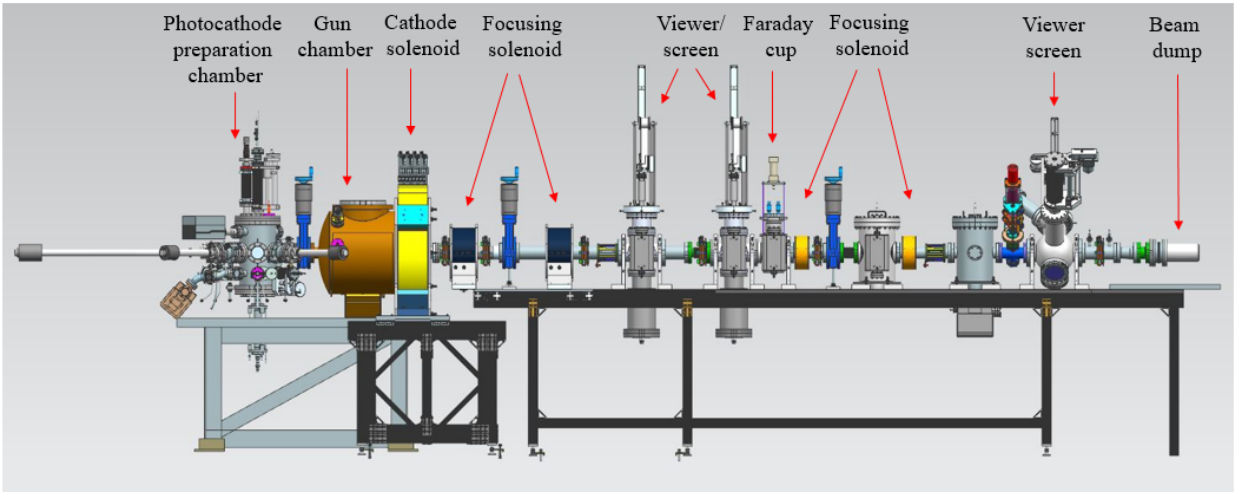

FIG. 2: Magnetized electron source.

The beamline mainly consists of a photo-gun high-voltage chamber, drive laser system, bi-alkali antimonide photocathode preparation chamber, cathode solenoid, and diagnostic beamline, all of which will be described in the following subsections.

2.1 GUN HIGH VOLTAGE CHAMBER

A load-lock type compact DC high-voltage photo-gun with inverted insulator geometry and spherical cathode electrode with a screening electrode operating at 300 kV was designed,

built, and installed for this study. The inverted-insulator design helps maintain a better vacuum with less field emission as it reduces the total metallic area inside the gun chamber. Figure 4 illustrates the main components of the photo-gun and Fig. 5 shows the photograph of the gun chamber. The photo-gun vacuum chamber is 36 cm in length and 46 cm in diameter and is made of 304L stainless steel with 0.5 cm thickness. Before assembly, the empty chamber was vacuum baked at 400 °C for 100 hours to reduce outgassing from the chamber walls [17], and was moved to a class 1000 cleanroom for the assembly.

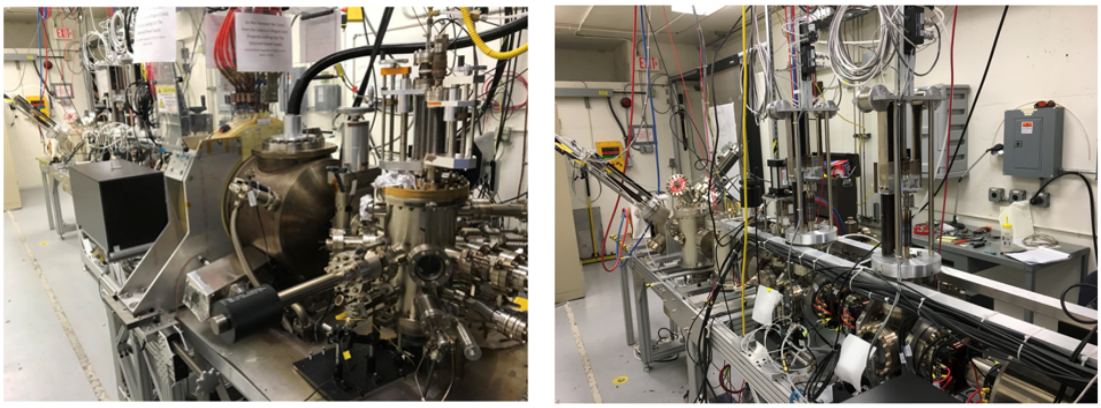

FIG. 3: Photographs of the beamline.

The cathode electrode is made by welding two 15.2 cm diameter hydroformed hemispherical shells (316L stainless steel). The front end has a 25° angle Pierce focusing geometry [18]. The angle terminates on a 1.3 cm diameter aperture exposing the flat photocathode. The photocathode is held against the back of the front face of the cathode electrode using spring-loaded sapphire rollers.

Figure 6 shows the anode electrode with a slightly curved front face to match the Pierce geometry located 9 cm downstream of the cathode front. The anode electrode is electrically isolated from ground potential to enable measurement of field emission from the cathode electrode and enable biasing as a means to repel downstream ions created by the beam [18]. There are five apertures in the anode plate where the middle aperture is for the beam to pass.

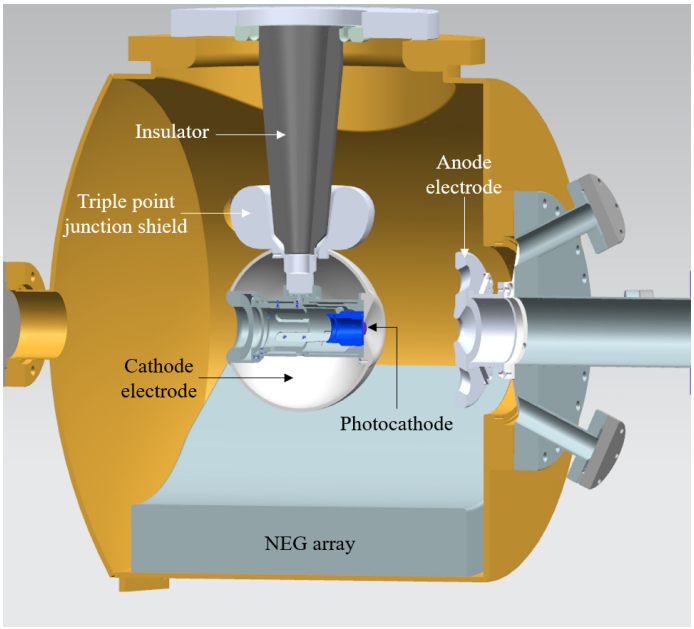

FIG. 4: Main components of the gun chamber.

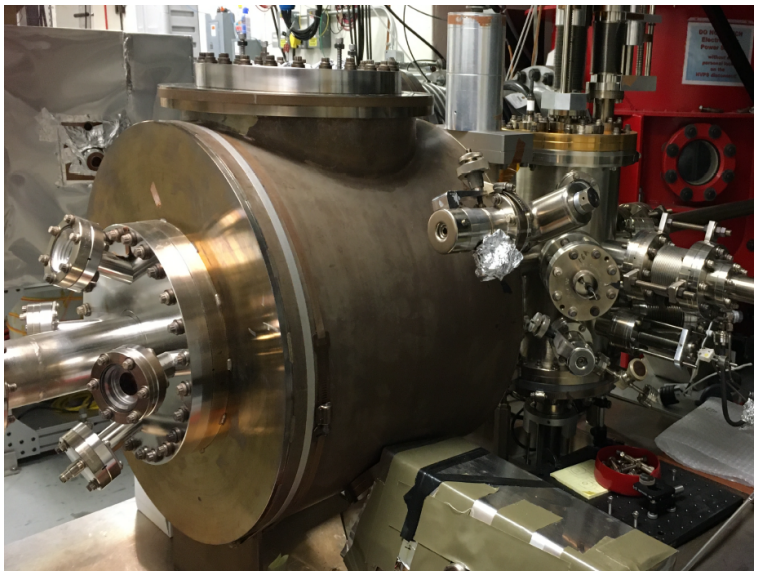

FIG. 5: Photograph of the gun chamber.

The left and right apertures deliver the laser to the photocathode and pass the unabsorbed laser out of the photo-gun, respectively. The top aperture is used as a viewport to check the laser spot location on the photocathode. The bottom aperture is for the feed-through to connect the anode electrically.

FIG. 6: Photograph of the anode electrode.

The high voltage is applied to the cathode electrode using a commercial high-voltage cable with a termination designed to mate with the inverted insulator geometry. The ceramic insulator and the high-voltage cable are industry-standard components with dimensions specified by the commercial designation R30. Figure 7 is a photograph of the industry-standard cable R30 plug. The narrow end of the conical insulator passes through a hole in the cathode electrode and mates to the locking device as shown in Fig. 8 that holds the photocathode puck. Figure 9 shows the photograph of the cathode electrode assembly mounted to the inverted insulator. This technique helps keep the gun vacuum electrically grounded and isolated from the high-voltage cable and the electrode.

The point where the cathode electrode, inverted insulator, and vacuum meets is called

FIG. 7: The industry-standard cable R30 plug.

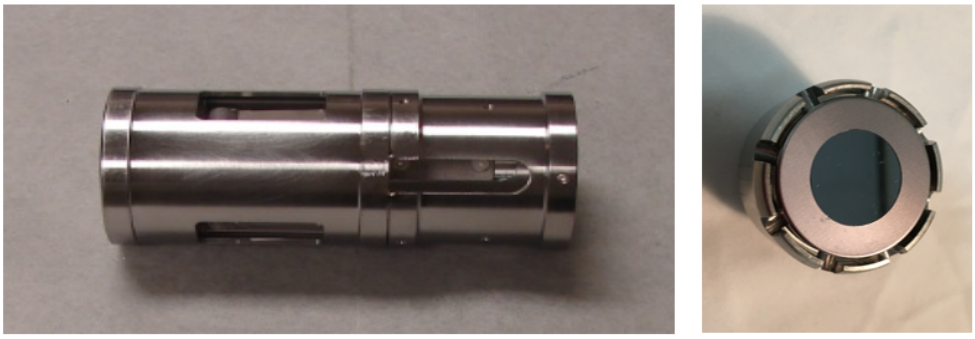

FIG. 8: Photograph of the locking device used to hold the photocathode puck (left) and the puck with tantalum cup holding Mo substrate (right).

FIG. 9: Photograph of the cathode electrode assembly mounted to the inverted insulator.

the triple point junction. Once the cathode is biased with high voltage, the electric field becomes very high and causes the insulator to break down, resulting in arcing. To prevent this, a specially designed screening electrode called the triple point junction shield is firmly attached to the cathode electrode, as shown in Fig. 9. After fabrication, all the electrode parts were barrel polished to achieve a mirror-like surface finish and cleaned in an ultrasonic bath of 2-propanol [19].

Two different high voltage power supplies were used at the GTS to energize the photo-gun. One is a 500 kV, 5 mA Cockcroft-Walton SF_6 gas-insulated DC high-voltage power supply as shown in Fig. 10 for high current delivery. It is a JLab modified Glassman model PS/PK500N004YU2 [20]. The photo-gun is connected to the high-voltage power supply, with a 300 MΩ conditioning resistor in series. The gun was high-voltage conditioned, and Kr processing was used to eliminate field emitters [10]. The photo-gun was conditioned to 360 kV and operated at or below 300 kV.

For high bunch charge measurements, a Spellman high-voltage power supply with 225 kV biased voltage and 30 mA average current with a power limit of 3 kW was used, as shown in Fig. 11 and Fig. 12. The R28 HV cable was used to connect the Spellman supply to the photo-gun.

The vacuum pressure inside the photo-gun while delivering electron beam is about 1×10^{11} Torr achieved using Non-Evaporable Getter (NEG) pumps and ion pumps. NEG pumps are vacuum pumps whose working principle is based on chemisorption and absorption. Figure 13 shows the NEG pumps at the bottom of the gun chamber (SAES WP1250 with ST707 material). NEGs are used to pump hydrogen, which is the dominant gas species inside the vacuum chamber. The NEGs are electrically isolated from the chamber as they cannot be activated during a bake-out and help maintain the vacuum afterward. Ion pumps remove noble gases and gas species like methane and carbon monoxide, which the NEGs poorly pump. Ion pumps are also used to check the vacuum level inside the chamber which is done by a highly sensitive current monitor (nA range) integral to the ion pump power supply. The ion pump current is proportional to pressure through the high 10^{-12} Torr range [18].

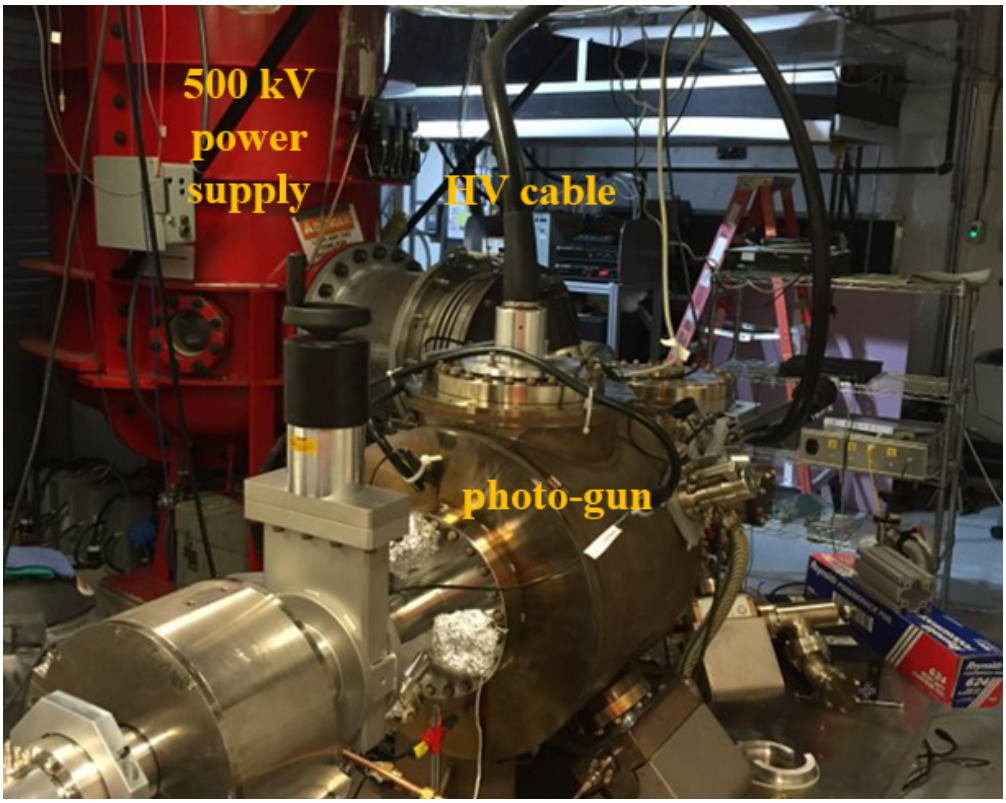

FIG. 10: Photograph of the gun electrode connected to a 500 kV, 5 mA DC power supply via a high-voltage cable.

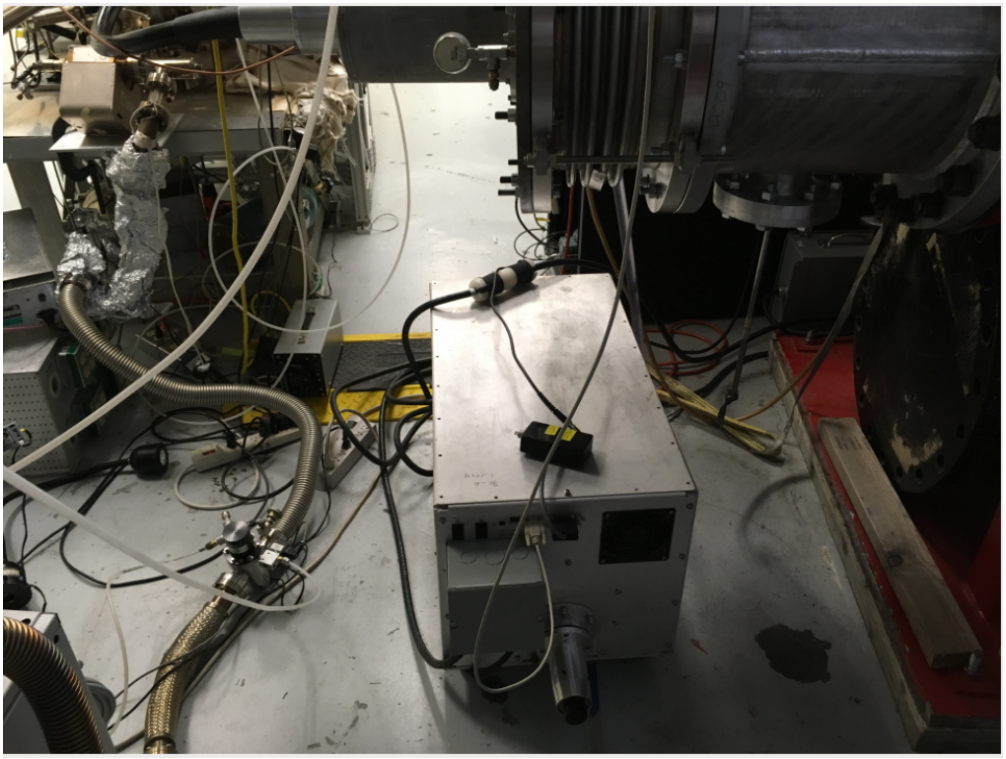

FIG. 11: Photograph of the Spellman power supply.

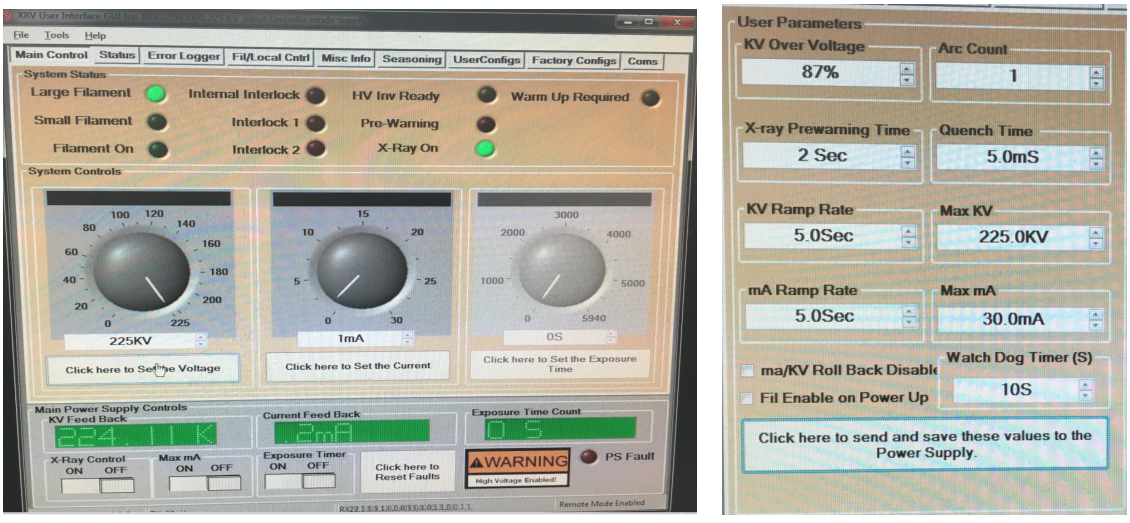

FIG. 12: User configuration of the Spellman power supply.

FIG. 13: The NEG modules inside the gun chamber.

2.2 PHOTOCATHODE PREPARATION CHAMBER

The JLEIC electron cooler was proposed to have a robust, high average current magnetized electron beam. Because of its higher quantum efficiency (QE), high current achievements, fast response-time, and robustness, alkali antimonide photocathodes were chosen to reach this goal. Figure 14 shows the load-lock type bialkali antimonide Cs_xK_ySb photocathode preparation chamber, which was built and installed behind the gun high-voltage chamber. The preparation chamber consists of a pure Sb source, a pure alkali (Cs and K) source, two heaters, four manipulators, a mask, two NEG pumps, an ion pump, a residual gas analyzer (RGA), and three thermocouples. The chamber can accommodate five photocathodes: three with GaAs substrates, one with Mo substrate, and one dummy puck for high-voltage conditioning. Figure 15 shows the schematic diagram of all the parts of the preparation chamber [21].

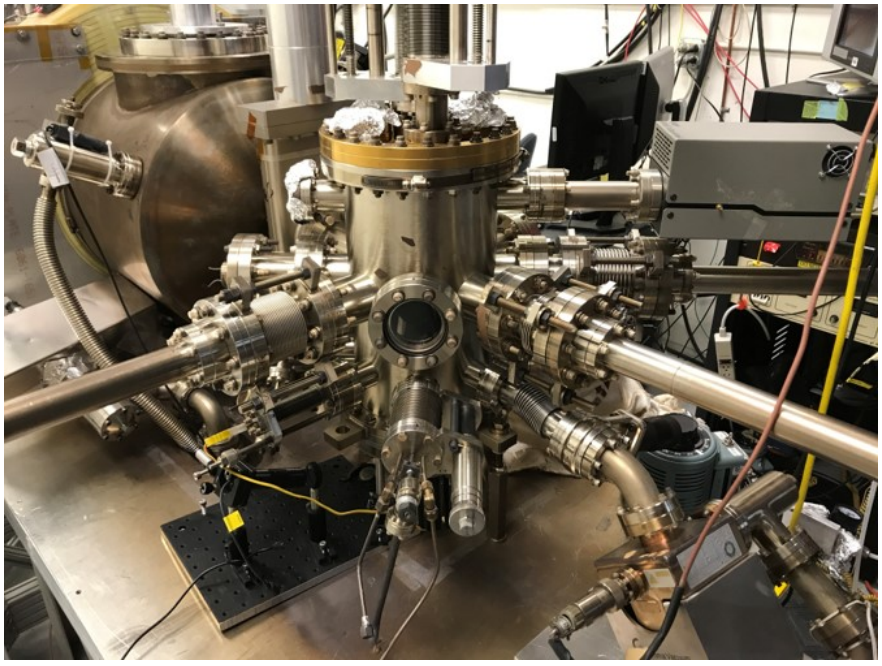

FIG. 14: Photograph of the photocathode preparation chamber.

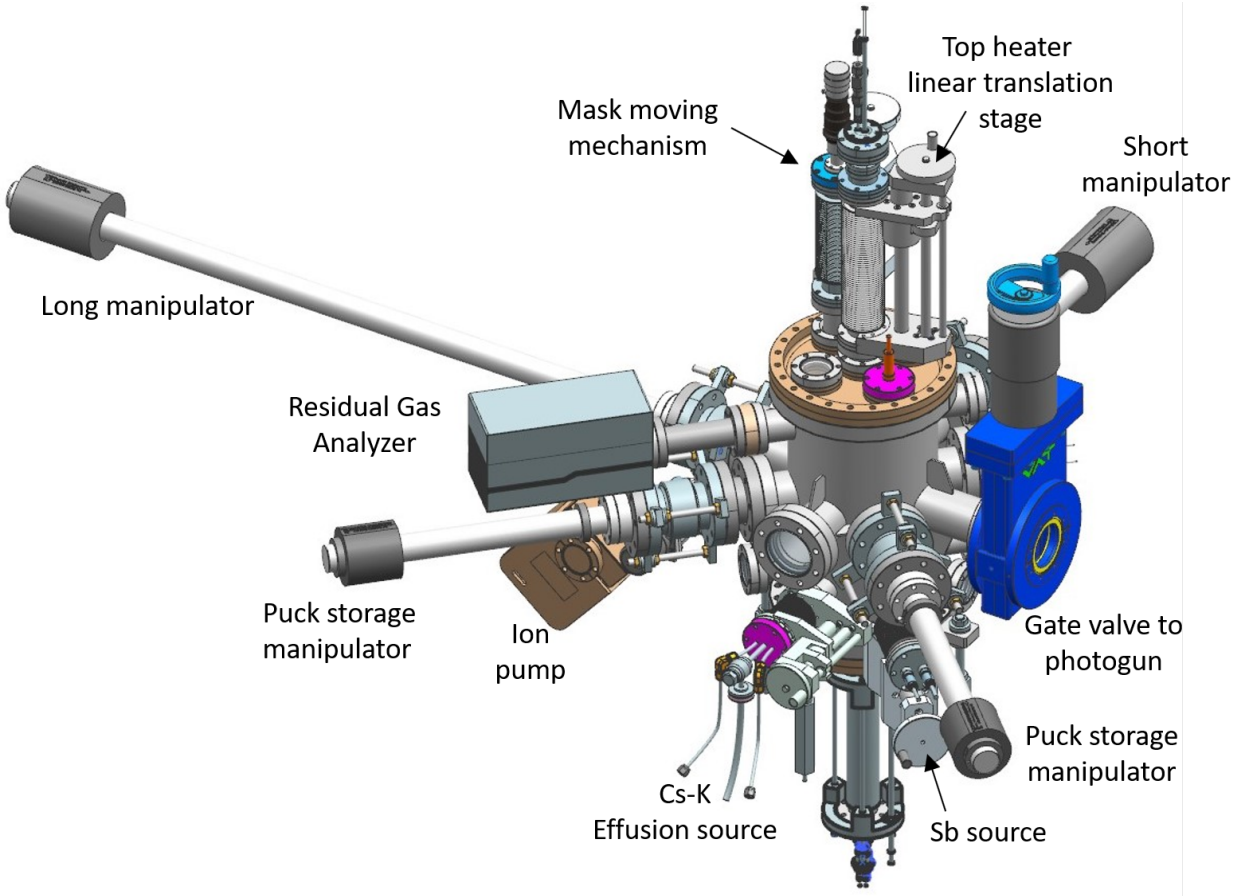

FIG. 15: Schematic diagram of the preparation chamber.

Two different substrates, GaAs and Mo were used to fabricate the photocathodes. GaAs is often used for high-brightness applications because it has the lowest thermal emittance of any photocathode known. The GaAs samples used were 3 - 6 mm thick, were p-dopped with Zn (1×10^{19} cm^{-3}), and have smooth surface finishes. One of the essential properties of a GaAs photocathode is that it can achieve negative electron affinity (NEA) due to Cs deposition on the surface. These photocathodes tend to have long operating lifetimes at low currents, but short lifetimes at high currents [15]. Hence, a Mo substrate was used for high current beam delivery, as it has superior thermal conductivity, which helps avoid QE degradation due to associated alkali loss by laser-induced heating [22]. The Mo substrate is 1 mm thick and hand-polished with sand papers and diamond paste to obtain a mirror-like surface finish. These substrates were firmly attached to the puck using a tantalum retaining

ring crimped tightly to the edge of the puck with indium foil between the puck face and the sample for electrical and thermal contact.

Photocathodes were fabricated using a two-step sequential deposition technique [17]. The first thin Sb film was deposited from a heated crucible. It was heated by supplying 25 A current through a tungsten wire wrapped around an alumina crucible containing Sb pellets. The Sb film thickness was varied using 10, 30, 60, and 90 minute deposition times. Then Cs and K were deposited using an effusion source containing both species. The photocurrent was continuously monitored using a low power (4 mW) 532 nm green laser during alkali deposition. The alkali deposition was discontinued when the photoemission current reached a maximum [10]. Figure 16 shows the inside view of the preparation chamber, and Fig. 17 illustrates the main components inside the chamber [18].

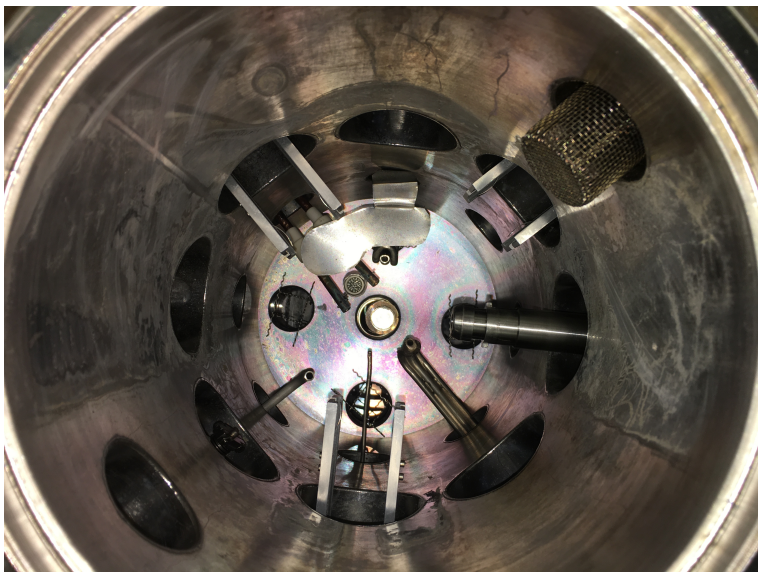

FIG. 16: Inside look of the photocathode preparation chamber.

The deposition chamber has two resistive heaters: one at the bottom and one at the top of the chamber. The bottom heater is used for heat cleaning the substrate at 450 °C for at least 18 hours. The top heater is used to maintain the surface deposition temperature

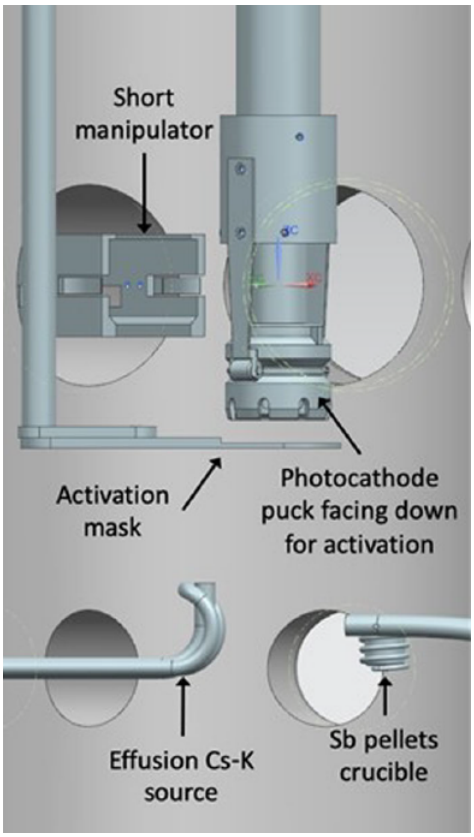

FIG. 17: Diagram of the photocathode activation vacuum chamber internal components showing the photocathode puck facing down behind the mask for photocathode fabrication.

at 120 °C. Pucks face up during substrate cleaning and face down during photocathode preparation [21].

The preparation chamber also has a stainless steel mask to limit the activation area. It has three holes with diameters of 1, 3, and 5 mm. The mask with the desired hole is positioned between the puck and the two sources. The chamber also consists of four magnetically coupled sample manipulators of different sizes. The main long manipulator is used to move pucks in and out of the gun chamber. Two short manipulators are used to move pucks to and from the heater and transfer the pucks to the long manipulator. The other short manipulator is used to store the pucks and move when needed. Further, the NEGs and ion pumps helped maintain the vacuum at 10^{-11} Torr, and a RGA mass spectrometer (SRS model RGA200) was used to monitor the vacuum gas composition continuously [21]. Figure 18 shows how all the pucks are placed inside the chamber.

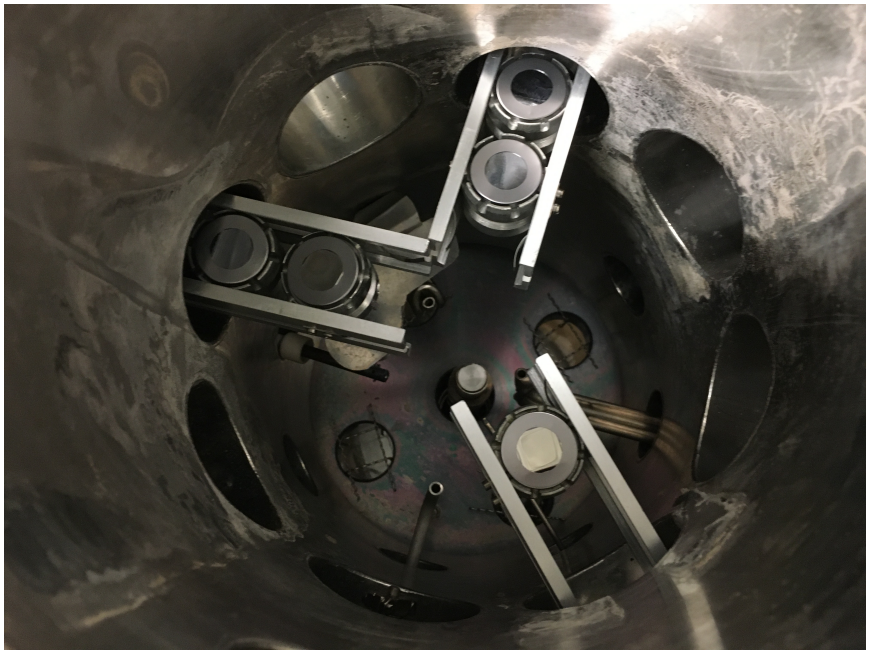

FIG. 18: Pucks inside the preparation chamber.

The quality of the photocathode is based on the QE and charge lifetime. Higher QE and a higher charge lifetime are desired. QE is the ratio between the number of electrons emitted and the number of incoming photons and can be calculated using the equation

$$QE = \frac{hc}{\lambda e}\frac{I}{P} \times 100\% = \frac{124}{\lambda}\frac{I}{P}\%, \tag{2}$$

where P (mW) is the incident laser power, I (μA) is the measured average current, λ is the laser wavelength (515 nm), h is Planck's constant (6.626×10^{-34} Js), e is the electron charge (1.602×10^{19} C), and c is the speed of light (2.998×10^{8} m/s).

One method to obtain a fair idea of the QE distribution of the photocathode is by performing a QE scan as shown in Fig. 19. A commercially available pen laser is used to scan across the whole photocathode surface and a pico-ameter connected to the anode measures the photocurrent. Before scanning, the scanning laser must be aligned and positioned correctly by selecting the scanning range. Then the photocathode is grounded using the long manipulator, and the anode plate is positively biased to 284 V. The measured QE values are usually lower than the actual QE values because the anode plate may not collect every electron emitted from the photocathode, since the 284 V bias voltage is relatively low. Sometimes it can be up to 40% lower than the actual QE.

More accurate QE values can be obtained by turning on the gun high voltage and sending a clean beam to the Faraday cup. Then one can calculate the QE using the beam current at the Faraday cup and the input laser power. The drawback of this method is that only one point can be checked each time, so it is not easy to map the whole photocathode.

2.3 DRIVE LASER

Two distinct drive lasers were used throughout this project: One for the high current generation and one for high bunch charge delivery. The laser used for the high current run was specifically constructed to provide light with RF structure at 532 nm with Watts of power and ps pulse width. It employs a master-oscillator-power-amplifier system composed of a 1.066 μm gain-switched diode laser (GSDL) and multistage Yb-fiber amplifier chain followed by a harmonic converter [23]. Further, it features adjustable pulse repetition rates from tens of MHz to a few GHz, a variable pulse width from tens to hundreds of ps, and a direct synchronization to an external RF signal without requiring RF-laser phase-locking systems. Sub-mW ps seed pulses from the GSDL were amplified to up to 8 W using two single mode Yb polarization-maintaining (PM) fiber amplifiers and a highly-doped double-clad Yb fiber power amplifier [23].

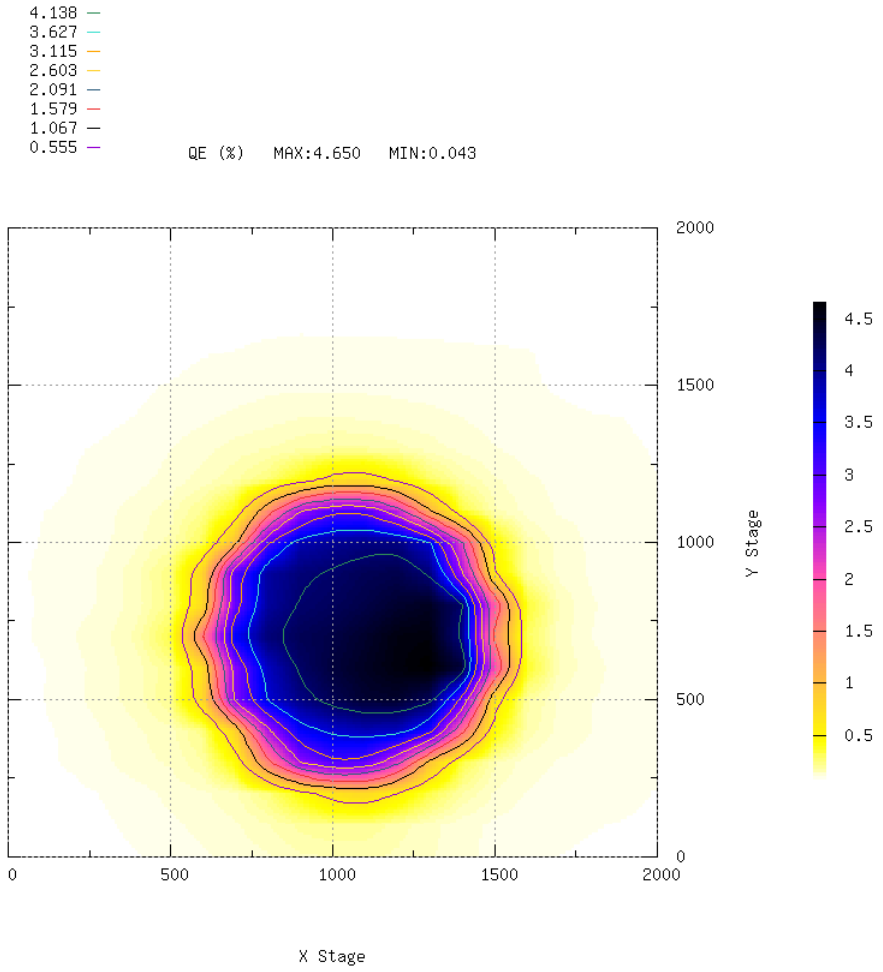

FIG. 19: A QE scan shows the QE distribution of a photocathode.

The second laser used for high bunch charge operations was a commercial ultra-fast laser with a pulse duration less than 0.5 ps, 20 μJ pulse energy, operating at 50 kHz pulse repetition and 1030 nm wavelength (NKT Origami). The IR beam was converted to 515 nm using a BBO crystal. A pulse stretcher consisting of a pair of diffraction gratings and reflectors in a double pass configuration were built to meet the pulse length requirement. The sub-picosecond pulses were lengthened to 75 - 120 ps (FWHM) by changing the stretcher's dispersion length [23]. An image-relaying optical transport was used for both lasers to deliver the light beams from the drive laser enclosure to an optical diagnostic hutch before reaching the photo-gun chamber as shown in Fig. 20.

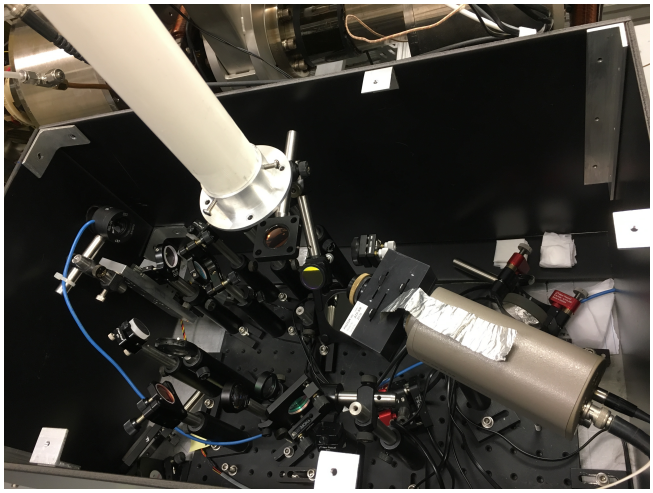

FIG. 20: Inside view of the optical diagnostic hutch.

The average power and laser pulse energy can be continuously varied using a rotating waveplate attenuator. A low duty-factor, machine-safe electron beam was produced using a rubidium titanyl phosphate Pockells cell and a mechanic shutter (*i.e.* a tune-mode generator) to protect the yttrium aluminum garnet (YAG) view screens [18, 23].

The size of the laser beam incident on the photocathode was adjusted using a simple telescopic lens system. A cylindrical lens was employed to ensure a circular laser profile at the photocathode illuminated at 25° angle of incidence. The transverse profile and size of

the laser spot on the photocathode were measured and monitored by placing a beam splitter between the last lens and the viewport in the photo-gun high-voltage vacuum chamber. The diverted laser beam was guided to a CCD camera positioned equidistant from the beam splitter and the photocathode. The image from the CCD camera was processed by Spiricon laser beam profiler software as shown in Fig. 21 [23, 24].

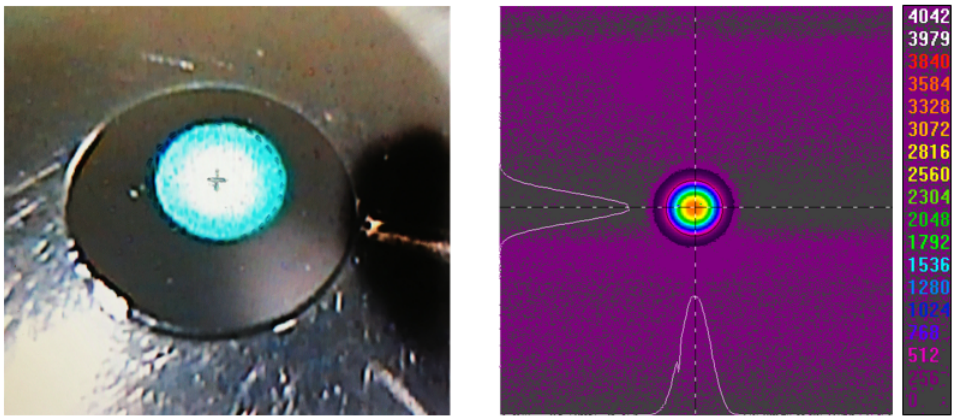

FIG. 21: Laser spot on the photocathode (left). Laser profile on the Spiricon software (right).

2.4 CATHODE SOLENOID

The cathode solenoid was designed to fit in front of the gun chamber 0.2 m away from the photocathode, as shown in Fig. 22. The properties of the solenoid are listed in Table 2. The solenoid does not have a steel shield. It is comprised of 16 layers each with 20 turns of water-cooled copper conductor, with a cross-section area of 0.53 cm^2 and a total length of 500 m. The solenoid was energized with a spare CEBAF magnet power supply [14].

A 2D magnetic field map of the cathode solenoid was generated using Opera software. The steel covers of the nearby focusing solenoids have distorted the magnetic field map as shown in Fig. 23.

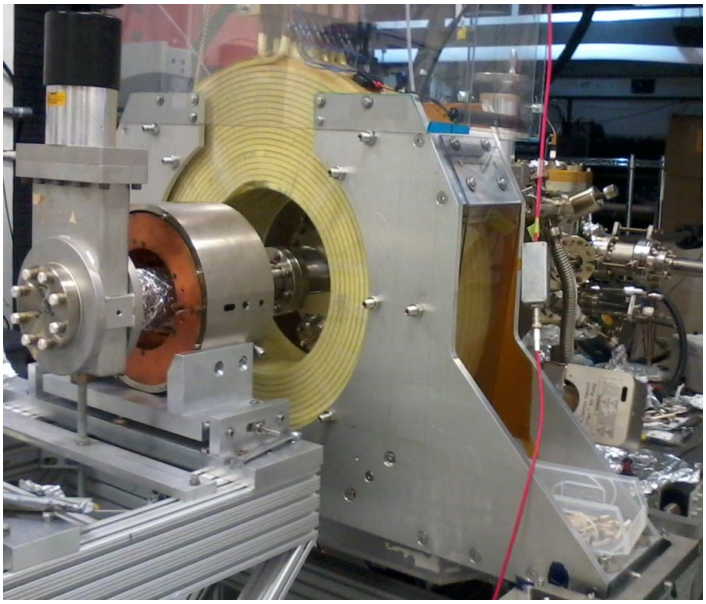

FIG. 22: Photograph of the cathode solenoid.

TABLE 2: Physical properties of the cathode solenoid.

Size	11.811” ID, 27.559” OD, 6.242” Z
Conductor	L=500 m, A=0.53 cm^2 (16 layers by 20 turns)
Coil Weight	240 kg
Resistance	0.18 Ω (65 °C average T)
Field at the photocathode	1.5 kG
Max field	3.3 kG
Voltage	72 V
Current	400 A

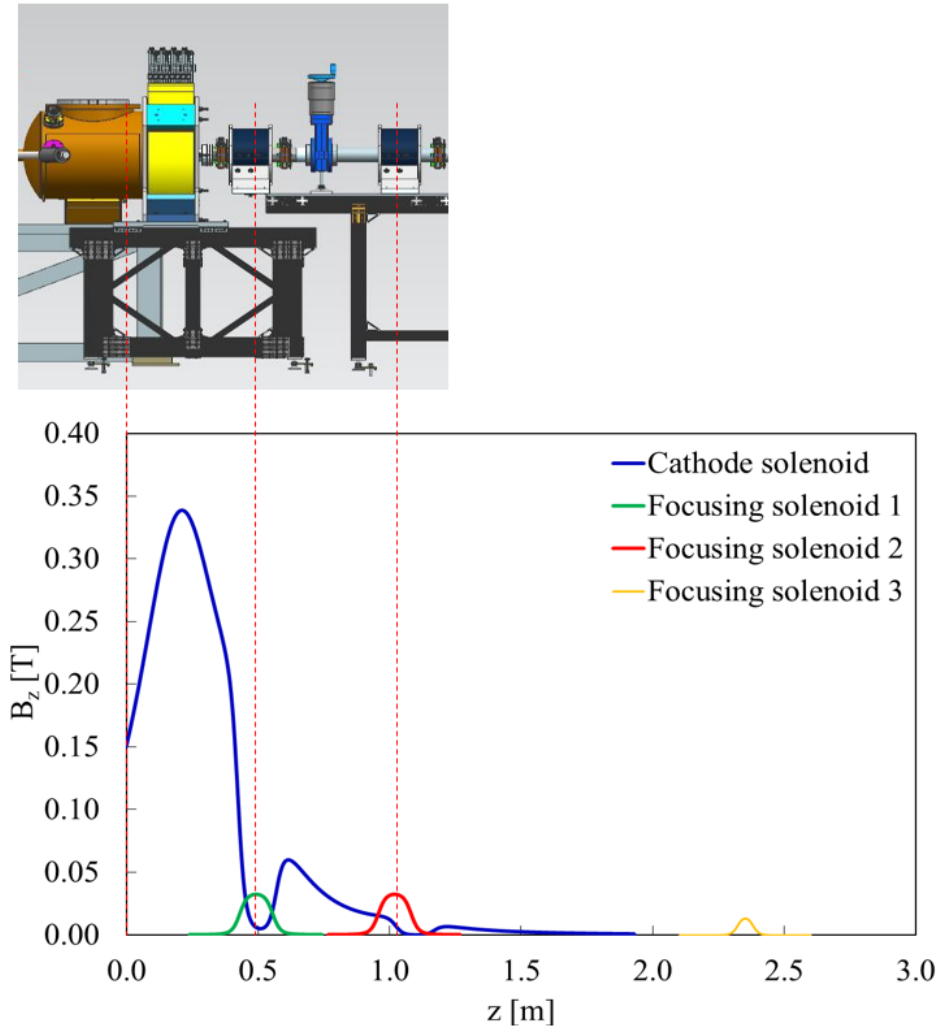

FIG. 23: Cathode solenoid field map and first three focusing solenoid field maps.

2.5 DIAGNOSTIC BEAM LINE

The diagnostic beamline extends 4.5 m from the photocathode with different beam pipe aperture sizes range from 1 - 5 cm radii. The beamline includes four focusing solenoids, two fluorescent YAG screen-slit combinations, a YAG screen, nine steering magnets, two ion collectors, two differential pumps, five ion pumps, two NEG pumps, a wire scanner, a Faraday cup, and a beam dump.

2.5.1 FOCUSING SOLENOIDS

There are four focusing solenoids located at 0.49, 1.01, 2.35, and 2.94 m. Figure 24 shows the focusing solenoid next to the cathode solenoid. The first two magnets are MFG magnets that provide up to 330 G magnetic field at the center using a maximum current of 4 A. The following two magnets are MFH magnets that provide provide up to 200 G magnetic field at the center using a maximum current of 1.5 A. The windings are in the metal housing as shown in the picture.

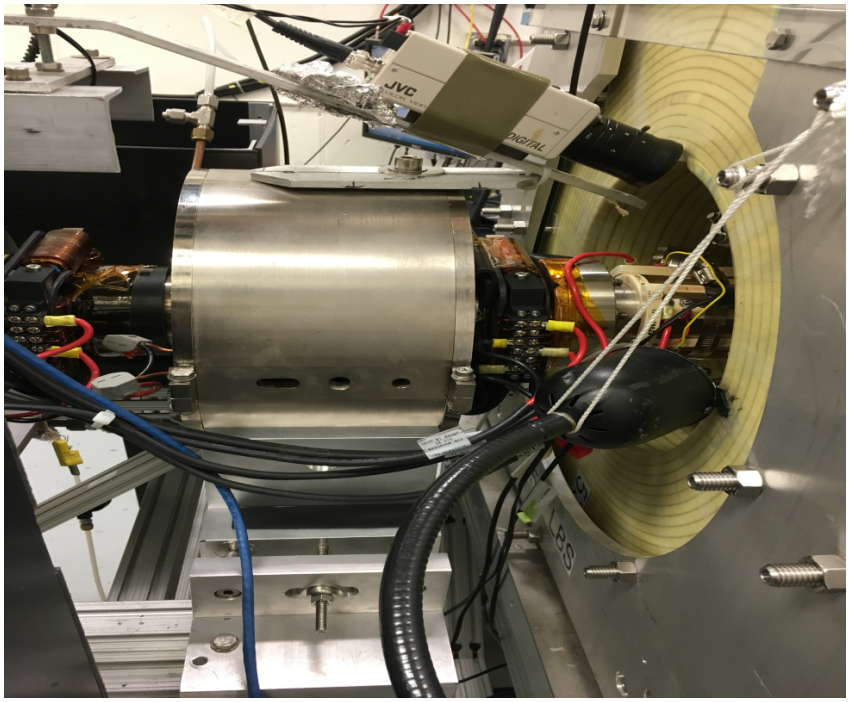

FIG. 24: One of the focusing solenoids.

2.5.2 VIEWER/SLIT

The beamline consists of two viewer-slit combinations at 1.5 m, 2.0 m, and one viewer at 3.75 m to measure the transverse density profile, location, rotation angle, and transverse emittance of the beam. Figure 25 shows the hardware design of the viewer slit combination, and Fig. 26 shows the schematic diagram.

FIG. 25: Photograph of two viewer-slit combinations.

A viewer is made of YAG single crystals of 0.1 mm thickness that fluoresce when struck by an electron beam. It is mounted on a round metal frame of 50.8 mm diameter. A system with a mirror forming a 45° angle to the viewer and an optical camera focused on the mirror is used to receive the image on the viewer to a computer screen. When using a viewer, one has to make sure the power is low, as an intense beam could saturate the viewer and the measurement would not be accurate. Also, beams can crack the viewers if the power exceeds the viewer power limit.

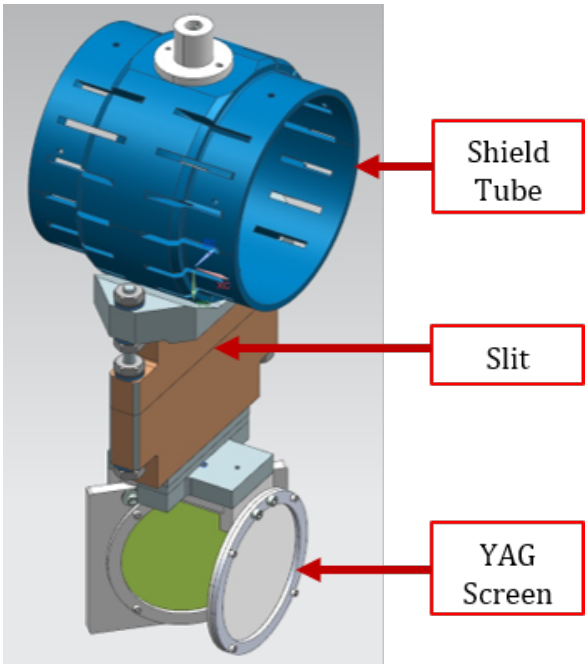

FIG. 26: Schematic diagram of the viewer slit combination.

Before measuring the beam size on a viewer, it should be calibrated to convert the pixel value to mm. The calibration method is as follow: First, the camera should be facing perpendicular to the viewer. Next, a circle is drawn on the inner circumference of the viewer, as shown in Fig. 27. The EPICS screen shows the dimensions of the circle in pixels. By comparing that number to the viewer circumference from the drawing, one can obtain a pixel to mm conversion.

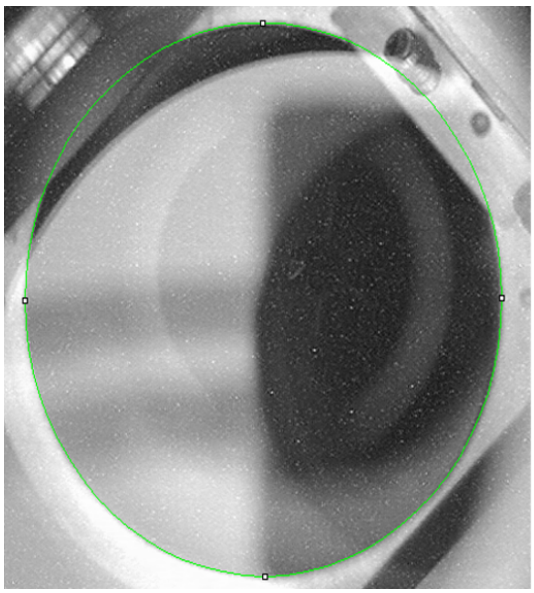

FIG. 27: Circle drawn on the inner circumference of the viewer.

2.5.3 STEERING MAGNETS

Steering magnets, commonly called correctors are used to correct the beam trajectory in horizontal and vertical directions. There are nine pairs of steering magnets located along the beamline. Two are air-core magnets and seven iron-core ones. These two types are shown in Fig. 28.

The air-core steering magnets are made of 100 turns of #24 american wire gauge (AWG) copper magnet wire with two opposed inner coils. These are mounted on the surface of the 6.35 cm diameter beamline to provide a transverse magnetic field say, in the x-direction; and two diametrically opposed outer coils mounted on the 8.23 cm outer diameter of the inner coils, to provide an orthogonally oriented transverse magnetic field, say, in the y-direction. With 200 mA of current flowing in series through each pair of dipole coils, the transverse momentum imparted to a traversing 100 keV electron will result in angular deflections of 33 mrad in the x-direction and 29 mrad in the y-direction. The maximum operating current is 1000 mA.

The iron-core steering magnets coils are directly wrapped on nickel-plated steel yokes and attached with epoxy. The design lends itself to traditional base mounting, while optional

clamps can be mounted directly to the beamline. For iron-core magnets, with a 100 keV electron beam and 200 mA current, the deflection angle is about 37 mrad in both x and y planes. Usually, an iron-core corrector is stronger than an air-core corrector.

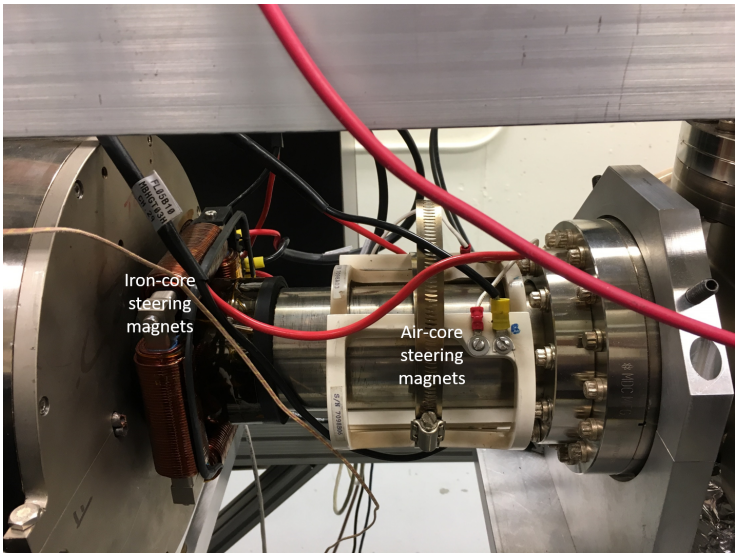

FIG. 28: Iron-core and air-core steering magnets.

2.5.4 ION PUMPS

Figure 29 shows one of the ion pumps attached to the beamline. Altogether there are seven ion pumps: one at the preparation chamber, one at the gun chamber, and five along the beamline. All have a pumping speed of 40 liters per second with an operating range from 10^{-6} to 10^{-12} Torr.

2.5.5 FARADAY CUP AND BEAM DUMP

A Faraday cup is located at 2.17 m, and the beam dump is located at 4.5 m from the photocathode. Each of them are electrically isolated so that beam current can be measured when the beam is delivered. Both are cooled using low conductivity water (LCW). The rated

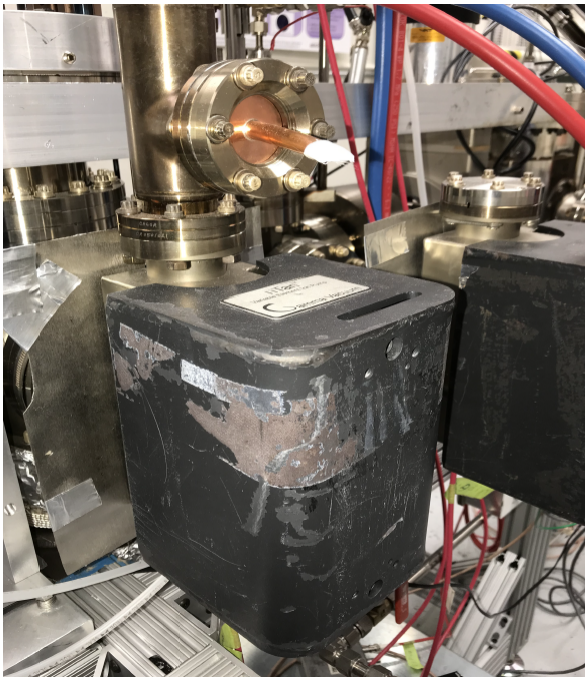

FIG. 29: Photograph of the ion pump.

power of the Faraday cup is 200 W, and that of the dump is 2.5 kW. The dump can accept up to 8 mA CW beam if the beam energy is 300 keV.

CHAPTER 3

THEORETICAL BACKGROUND

This chapter discusses the basic concepts of accelerator physics, linear beam dynamics, and derivations of some of the mathematical formalism used extensively in this dissertation.

3.1 BEAM DYNAMICS AND COORDINATE SYSTEM

Particle accelerators mainly consist of components that accelerate the particles to the desired energy, guide them to follow the desired transportation line while focusing to minimize the losses. In doing so, particles constantly interact with static and time-varying electromagnetic fields and subject to Lorentz forces

$$\boldsymbol{F}_{ext} = q(\boldsymbol{E} + [\boldsymbol{v} \times \boldsymbol{B}]), \tag{3}$$

where q is the charge of the particle, $\boldsymbol{E}$ and $\boldsymbol{B}$ are the electric and magnetic field vectors, $\boldsymbol{v}$ is the particle velocity. In general, particles are accelerated from a static or time-varying electric field using DC or RF guns. Particles bend, focus or defocus from the magnetic field using dipole magnets, quadrupole magnets, etc.

Particle motion in a linear accelerator system is commonly described by Cartesian coordinate system (x, y, z). Time derivative of (x, y, z) is denoted by $(\dot{x},\ \dot{y},\ \dot{z})$ or the velocities as $(v_x,\ v_y,\ v_z)$. Particle momentum is given by

$$p_i = \gamma m v_i, \tag{4}$$

where, $(i = x, y, z)$, m is the rest mass of the particle, γ is the Lorentz factor given by $\gamma = 1/\sqrt{1-\beta^2}$, $\beta = v/c$ and c is the speed of light in vacuum.

In order to simplify the beam dynamics, the motion of a particle is divided into transverse and longitudinal directions where the longitudinal coordinate denote by s follows the particle trajectory and the horizontal and vertical components $(x(s),\ y(s))$ describe the particle's motion in transverse directions relative to the trajectory. Since all accelerator systems are fixed to a specific location, the particle motion can be better described by its position rather than the time. Thus, the mathematical formalism has been derived using s as the

independent coordinated instead of time. The derivative of $(x(s), y(s))$ with respect to s, are denoted as $(x'(s), y'(s))$.

3.2 LINEAR EQUATIONS OF MOTION

The transverse equation of motion of a particle in an accelerator, assuming no momentum deviation from designed momentum is simply given by the Hill's equation

$$u''(s) + K(s)u = 0, \tag{5}$$

where u represents either horizontal or vertical displacement x or y and $K(s)$ is a constant for a linear machine and has periodicity for a circular machine that describes the magnetic field strength present at a location s along the beamline. Usually, dipole and quadrupole fields with uncoupled motion in the two transverse planes are considered, solving this equation [25].

For $K > 0$ the solutions to the above equation can be written as

$$\begin{aligned} u(s) &= A\,\cos(\sqrt{K}s) + B\,\sin(\sqrt{K}s), \\ u'(s) &= -\sqrt{K}A\,\sin(\sqrt{K}s) + \sqrt{K}B\,\cos(\sqrt{K}s). \end{aligned} \tag{6}$$

Applying the initial conditions $s = 0,\ u(s) = u_0$ and $u'(s) = u'_0$ Eq. 6 can be rewritten as

$$\begin{aligned} u(s) &= u_0\,\cos(\sqrt{K}s) + \frac{u'_0}{\sqrt{K}}\,\sin(\sqrt{K}s), \\ u'(s) &= -u_0\sqrt{K}\,\sin(\sqrt{K}s) + u'_0\,\cos(\sqrt{K}s). \end{aligned} \tag{7}$$

This solution can be expressed in matrix formulation as

$$\begin{pmatrix} u(s) \\ u'(s) \end{pmatrix} = \begin{pmatrix} \cos(\sqrt{K}s) & \frac{1}{\sqrt{K}}\sin(\sqrt{K}s) \\ -\sqrt{K}\,\sin(\sqrt{K}s) & \cos(\sqrt{K}s) \end{pmatrix} \begin{pmatrix} u_0 \\ u'_0 \end{pmatrix}. \tag{8}$$

Also,

$$U(s) = M(s|s_0)U_0 \quad \text{with} \quad U(s) = \begin{pmatrix} u(s) \\ u'(s) \end{pmatrix}, \tag{9}$$

and

$$M(s|s_0) = \begin{pmatrix} \cos(\sqrt{K}s) & \frac{1}{\sqrt{K}}\sin(\sqrt{K}s) \\ -\sqrt{K}\,\sin(\sqrt{K}s) & \cos(\sqrt{K}s) \end{pmatrix}, \tag{10}$$

which called the transfer matrix from s_0 to s and the determinant of $M(s|s_0)$ is unity.

For $K < 0$, the above solution changes to

$$M(s|s_0) = \begin{pmatrix} \cosh(\sqrt{K}s) & \frac{1}{\sqrt{K}}\sinh(\sqrt{K}s) \\ -\sqrt{K}\,\sinh(\sqrt{K}s) & \cosh(\sqrt{K}s) \end{pmatrix}. \tag{11}$$

$M(s|s_0)$ can be obtained for each element. Thus, particle trajectory along a complicated beamline represent by each element in intervals from s_0, s_1, ... s_{n-1}, s_n can be deduced by repeated matrix multiplication as

$$M(s_n|s_0) = M(s_n|s_{n-1})...M(s_2|s_1)M(s_1|s_0), \tag{12}$$

without solving the Hill's equation at every s. For instance, in drift space $K = 0$ and transfer matrix becomes

$$M(s|s_0) = \begin{pmatrix} 1 & l \\ 0 & 1 \end{pmatrix}, \tag{13}$$

where $l = s - s_0$. For a quadrupole with length l and strength K transfer matrix is given by either Eq. 10 or Eq. 11 depending on whether focusing $K > 0$ or defocuing $K < 0$. The thin lens approximation can be applied when focal length of the quadrupole f is large compared to l. When $l = s - s_0 \to 0$ while keeping the focal strength constant, $1/f = Kl =$ constant. Thus, Eq. 10 becomes

$$M(s|s_0) = \begin{pmatrix} 1 & 0 \\ -1/f & 1 \end{pmatrix}. \tag{14}$$

3.3 PHASE SPACE

In theory, beam is defined as a collection of particles that contained in a finite region of phase space. Phase space is a 6-dimensional space where each particle along the beamline is represented by a point with coordinates (x, p_x, y, p_y, z, p_z) where (x, y, z) are the position vectors and (p_x, p_y, p_z) are the momentum vectors. This occupies a 6-dimensional hyper volume generally referred as Γ_6. In 6-dimensional phase space a beam that consists of N particles at a given instant is best described by density function $f(x, y, z, p_x, p_y, p_z)$. Hence, the number of particles in an element of space volume $d\tau_6 = dxdp_xdydp_ydzdp_z$ is given by

$$d^6N = f(x, y, z, p_x, p_y, p_z)d\tau_6. \tag{15}$$

Providing there is no coupling between the axial and transverse motion or acceleration, the 6-dimensional hyper volume V can be projected onto three 2-dimensional orthogonal planes. Thus, the total phase space density of particles becomes a product of the three subspace densities

$$f(x, y, z, p_x, p_y, p_z) = f(x, p_x).f(y, p_y).f(z, p_z). \tag{16}$$

Furthermore, each subspace can be studied separately. There are a few main properties that particle trajectories obey in phase space. They are, the trajectories depend on the initial values of the coordinate and time. Hence, two trajectories with different initial conditions cannot intersect. Also, a boundary in the phase space that encloses a given number of particles at a given time t will map into a boundary a time t' which enclose the same number of particles [25].

Particle density in phase space satisfies the Liouville's theorem, which states that under the influence of conservative forces, the particle density in phase space stays a constant. This can also be stated as the invariant of the phase space hyper-volume enclosing a chosen group of points as they move in the phase space.

$$\frac{dV}{dt} = 0. \tag{17}$$

According to the theorem, the location and the distribution of the beam at any place along the beamline can be easily deduced from the information of the area occupied by the particles in phase space at the beginning of the beamline. However, there are a few situations in Liouville's theorem cannot be applied such as electron cooling, electromagnetic radiation is present, e.g., synchrotron.

According to the phase space coordinates transverse momenta can be written as $p_x = p_0 \tan(x')$ and $p_y = p_0 \tan(y')$. For a considerable small transverse momentum distribution $p_x = p_0 x'$ and $p_y = p_0 y'$. Thus, one can use the slope of the trajectory x' and y' as the transverse momentum coordinates as long as the p_0 is constant which is true in many beam dynamic calculations. Coordinate space expressed in $x - x'$ and $y - y'$ are called the trace space [25].

Particle distribution in phase space commonly takes the shape of an ellipse, and such ellipse is generally referred to as phase space ellipse, by mapping the ellipse properties into particle distribution as in Fig. 30 essential properties such as the area, shape, and orientation of the particle distribution can be found [26].

Equation of the phase space ellipse is as follows

$$\gamma x^2 + 2\alpha x x' + \beta x'^2 = \epsilon, \tag{18}$$

where α, β, γ and ϵ are the ellipse parameters. α is related to the beam orientation and β gives the shape and size of the beam. ϵ is called the beam emittance which is the area enclosed by the ellipse

$$\int_{ellipse} dx dx' = \pi\epsilon. \tag{19}$$

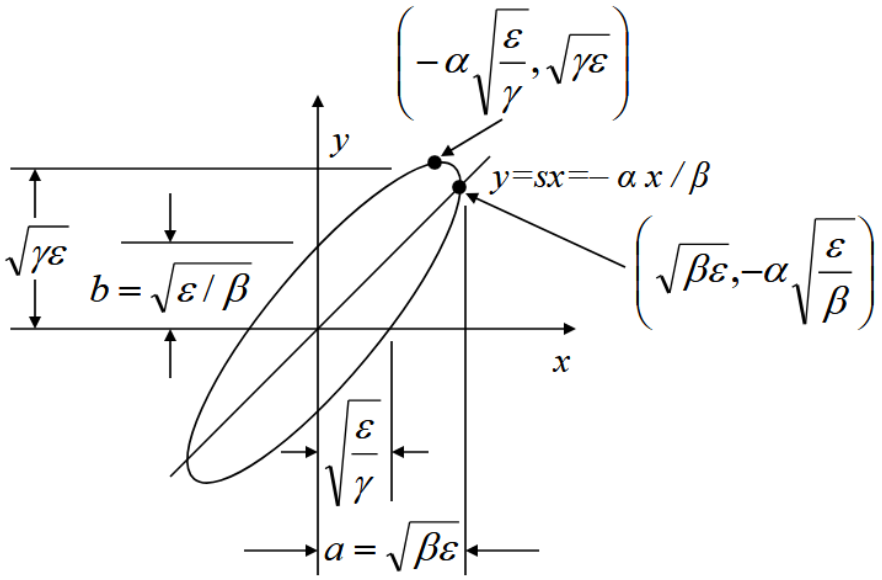

FIG. 30: Phase space ellipse.

Let us consider the particle which is on the largest phase space ellipse within a particular beam where all the other particles stay within that ellipse and use the dynamics of that particle to explain the behavior of the distribution. Let phase space ellipse at $s = 0$ be

$$\gamma_0 x_0^2 + 2\alpha_0 x_0 x_0' + \beta_0 x_0'^2 = \epsilon. \tag{20}$$

By using the transfer matrix Eq. 8 which is used to obtain the particle trajectory at any other location along the beamline that $s \neq 0$, and solving for x_0 and x_0' and substituting to Eq. 20 yields

$$\begin{aligned}\epsilon = &(C'^2\beta_0 - 2S'C'\alpha_0 + S'^2\gamma_0)x^2 \\ &+ 2(-CC'\beta_0 + S'C\alpha_0 + SC'\alpha_0 - SS'\gamma_0)xx' \\ &+ (C^2\beta_0 - 2SC\alpha_0 + S^2\gamma_0)x'^2,\end{aligned} \tag{21}$$

where $C = \cos(\sqrt{K}s)$, $S = \sin(\sqrt{K}s)$ and C' and S' are derivatives with respect to s. This equation can be reformulated as Eq. 18 by replacing the coefficients as follows

$$\begin{aligned}\gamma &= C'^2\beta_0 - 2S'C'\alpha_0 + S'^2\gamma_0, \\ \alpha &= -CC'\beta_0 + S'C\alpha_0 + SC'\alpha_0 - SS'\gamma_0, \\ \beta &= C^2\beta_0 - 2SC\alpha_0 + S^2\gamma_0.\end{aligned} \tag{22}$$

The resulting new ellipse has the same area $\pi\epsilon$ but due to the different α, β, and γ values the new ellipse will have a different shape and orientation. Hence during the propagation along the beamline the phase space continuously change its form and orientation but not its area. The ellipse parameters can also be represented in matrix formalism as [25]

$$\begin{pmatrix}\beta(s) \\ \alpha(s) \\ \gamma(s)\end{pmatrix} = \begin{pmatrix} C^2 & -2CS & S^2 \\ -CC' & CS' + C'S & -SS' \\ C'^2 & -2C'S' & S'^2 \end{pmatrix} \begin{pmatrix}\beta_0 \\ \alpha_0 \\ \gamma_0\end{pmatrix}. \tag{23}$$

In beam dynamics, α, β, and γ are referred to as the Twiss parameters or Courant-Snyder parameters. Using the above matrix formalism with initial values of α_0, β_0, and γ_0, beam parameters anywhere along the beamline can be easily deduced. Further from the geometric properties of an ellipse, the correlation between Twiss parameters and beam distribution can be set as

$$\beta\gamma - \alpha^2 = 1. \tag{24}$$

Beam waist where the minimum beam size occurs when $\alpha = 0$. The location of the beam waist is given by

$$s_w - s_0 = \frac{\alpha_0}{\gamma_0}. \tag{25}$$

When the beam is diverging, α_0 is negative, and when the beam is converging, α_0 is positive.

3.4 BEAM MATRIX

Phase space transformation to n-dimensional ellipse can be written in

$$u^T \sigma^{-1} u = 1, \tag{26}$$

where u is the coordinate vector, and σ is a symmetric matrix called the beam matrix. By applying Eq. 26 to the two-dimensional phase space ellipse equation [25],

$$\begin{pmatrix} x & x' \end{pmatrix} \begin{pmatrix} \sigma_{11} & \sigma_{12} \\ \sigma_{21} & \sigma_{22} \end{pmatrix}^{-1} \begin{pmatrix} x \\ x' \end{pmatrix} = 1. \tag{27}$$

Since $\sigma_{12} = \sigma_{21}$ this can be expressed as

$$\sigma_{22} x^2 - 2\sigma_{12} x x' + \sigma_{11} x'^2 = \det\, \sigma. \tag{28}$$

Comparing Eq. 28 with Eq. 18 yields the following relation

$$\sigma = \begin{pmatrix} \sigma_{11} & \sigma_{12} \\ \sigma_{21} & \sigma_{22} \end{pmatrix} = \epsilon_x \begin{pmatrix} \beta_x & -\alpha_x \\ -\alpha_x & \gamma_x \end{pmatrix}. \tag{29}$$

Thus, two dimensional phase space area can be written as

$$\pi \sqrt{\sigma_{11}\sigma_{22} - \sigma_{12}^2} = \pi\epsilon. \tag{30}$$

The definition of the beam matrix elements are measures of the particle distribution in phase space such as uniform, Gaussian etc. In order to obtain a uniform definition of beam matrix elements for Gaussian distribution the solution to the Hill's equation for a particular particle in amplitude-phase form is considered

$$x_i = a_i \sqrt{\beta}\, \cos(\psi + \psi_i), \tag{31}$$

where, a_i and ψ_i are constants, β is the beta function and $\psi = \sqrt{K} s$. Taking average of all the particles within a well defined fraction of beam and simplifying yields

$$\begin{aligned} \langle x_i^2 \rangle &= \frac{1}{2} \langle a_i^2 \rangle \beta = \epsilon\beta, \\ \langle x_i'^2 \rangle &= \frac{1}{2} \langle a_i^2 \rangle \frac{1+\alpha^2}{\beta} = \epsilon\gamma, \\ \langle x_i x_i' \rangle &= -\frac{1}{2} \langle a_i^2 \rangle \alpha = -\epsilon\alpha, \end{aligned} \tag{32}$$

where

$$\begin{aligned} \epsilon &= \frac{1}{2}\langle a_i^2 \rangle, \\ \alpha &= -\frac{1}{2}\beta', \\ \gamma &= \frac{(1+\alpha^2)}{\beta}. \end{aligned} \tag{33}$$

The beam matrix elements become

$$\begin{aligned} \sigma_{11} &= \langle x_i^2 \rangle = \epsilon\beta, \\ \sigma_{22} &= \langle x_i'^2 \rangle = \epsilon\gamma, \\ \sigma_{12} &= \langle x_i x_i' \rangle = -\epsilon\alpha. \end{aligned} \tag{34}$$

Beam emittance can be expressed as

$$\epsilon^2 = \langle x_i^2 \rangle \langle x_i'^2 \rangle - \langle x_i x_i' \rangle. \tag{35}$$

The transfer matrix M for transverse plane x that describe the particle motion through a beamline consisting of non dispersive elements (elements that induce a transverse motion dependent on the particle energy) is given by

$$\begin{pmatrix} x_f \\ x_f' \end{pmatrix} = \begin{pmatrix} M_{11} & M_{12} \\ M_{21} & M_{22} \end{pmatrix} \begin{pmatrix} x_i \\ x_i' \end{pmatrix}. \tag{36}$$

Using the identities $I = M^{-1}M = M^T(M^T)^{-1}$ and substituting into Eq. 27 at the initial starting point i, yields

$$x_i^T (M^T(M^T)^{-1}) \sigma_i^{-1} (M^{-1}M) x_i = 1. \tag{37}$$

By simplifying this the beam matrix at the final position f can be obtained by

$$\sigma_f = M \sigma_i M^T. \tag{38}$$

3.5 EMITTANCE

Emittance is a commonly used figure of merit in comparing electron sources. It expresses the average spread of the particles in a beam in phase space and has a dimension of length

times angle (m rad). Unlike other beam qualities, *i.e.*, beam dimensions that vary with the location, emittance is a conserved quantity when there are no dissipative or cooling forces present. Typically emittance can be separated for each plane (x, y, and z) when they are no or very weakly coupled. The total emittance is usually a combination of that induced by thermal, space charge, RF systems, etc.

The statistical definition of the phase space normalized (n) rms emittance in x plane is given by

$$\epsilon_{n,x,rms} = \frac{1}{m_0 c}\sqrt{\langle x^2\rangle\langle p_x^2\rangle - \langle x p_x\rangle}, \tag{39}$$

where m_0 is the electron rest mass, c is the speed of light [25]. When a beam accelerates, the transverse beam size shrinks. In order to have a constant emittance, it is scaled according to the beam energy $\epsilon_n = \beta\gamma\epsilon$ where γ and β are the relativistic parameters defined by the beam energy. This is referred to as the normalized emittance.

3.5.1 GEOMETRIC EMITTANCE

From the rms normalized emittance, the geometric emittance can be written as

$$\epsilon_{rms} = \frac{m_0 c}{\langle p_z\rangle}\epsilon_{n,rms}, \tag{40}$$

where $\langle p_z\rangle$ denotes the mean longitudinal momentum.

During the acceleration of the electron bunch, the longitudinal momentum increases while the transverse momentum remains constant. Thus, the geometric emittance decreases as $\langle p_z\rangle$ increases, while the normalized phase space emittance does not show this feature. This is adiabatic damping.

3.5.2 TRACE SPACE EMITTANCE

Normalized trace space emittace is given by

$$\epsilon_{n,x,tr,rms} = \frac{\langle p_z\rangle}{m_0 c}\sqrt{\langle x^2\rangle\langle x'^2\rangle - \langle x x'\rangle}. \tag{41}$$

Experimentally, trace space emittance is calculated by measuring x' and y' instead of transverse momenta [27].

3.5.3 THERMAL EMITTANCE

Thermal emittance is the lowest possible emittance that an injector can be achieved. It mainly depends on the illuminating wavelength, the degree of negative affinity, and the band structure of the photocathode material [28].

The thermal emittance can be calculated by assuming the electrons from the cathode are emitted uniformly and isotropically, within a radius r in the presence of an accelerating field. The transverse thermal energy of the cathode can be written as $k_B T_\perp$. By using $\frac{1}{2} m_0 \langle v_x^2 \rangle = \frac{1}{2} k_B T_\perp$ for nonrelativistic photoelectrons where $v_x = p_x/m_0$ being the transverse component of the velocity and $\langle x^2 \rangle = \sigma^2 = r^2/4$ in Eq. 39 with $\langle x p_x \rangle = 0$ yields the expression for thermal emittance

$$\epsilon_{the,n,rms} = \sigma_0 \sqrt{\frac{k_B T_\perp}{m_0 c^2}} = \sigma_0 \sqrt{\frac{E_{kin}}{m_0 c^2}}, \tag{42}$$

where σ_0 is the rms of the emitting area and E_{kin} is the average thermal energy (eV) [28].

3.5.4 EMITTANCE MEASUREMENT

Though emittance plays a major role in characterizing the beam, there is no single direct measurement to acquire it. Emittance includes both beam size and its divergence, and though there are many ways to measure the beam size, there is no direct way to measure the beam divergence. Thus, over the years, people have come up with various techniques to measure the transverse and longitudinal emittances. Single solenoid scan, quadrupole scan, pepper pot, single slit, multiple slits, harp scan are some techniques used to measure the transverse emittance. In our experiment, we used the simple solenoid scan method. There are two types of solenoid scan calculation methods; thick lens method and thin lens approximation. One should decide which method is suitable for their setup according to the thickness of the solenoid (l) compared to the distance between solenoid to viewer (L) or focal length (f). In our case, we used the thick lens method since l is no longer ignored; it is not negligible when compared to the focal length.

The solenoid scan method involves beam size measurements on a specific viewer as a function of the magnet field strength of the scanning solenoid. Then the calculation process goes as follows.

If Q represents the transfer matrix of the solenoid where l is the length of the solenoid, k is the strength of the solenoid, $\varphi = \frac{1}{2} kl$ and focal length $f = \frac{4}{k^2 l}$, and S represents the transfer matrix between the solenoid and the viewer as shown in Fig. 31, the transfer matrix M can be written as [29]

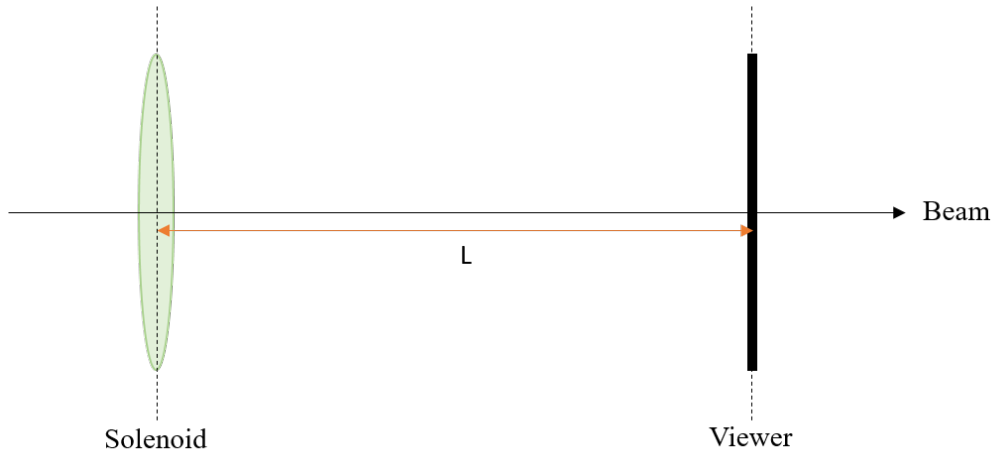

FIG. 31: Schematic diagram of the solenoid scan setup.

$$Q = \begin{pmatrix} \cos\varphi & \frac{2}{k}\sin\varphi \\ -\frac{k}{2}\sin\varphi & \cos\varphi \end{pmatrix} \quad , \quad S = \begin{pmatrix} 1 & L \\ 0 & 1 \end{pmatrix}, \tag{43}$$

$$M = \begin{pmatrix} \cos\varphi - \frac{Lk}{2}\sin\varphi & \frac{2}{k}\sin\varphi + L\cos\varphi \\ -\frac{k}{2}\sin\varphi & \cos\varphi \end{pmatrix}. \tag{44}$$

The first term of the beam matrix can be written as

$$\sigma_{11} = \langle x^2 \rangle = M_{11}^2\sigma_{11}^{(0)} + 2M_{11}M_{12}\sigma_{12}^{(0)} + M_{12}^2\sigma_{22}^{(0)}, \tag{45}$$

$$\begin{aligned} \sigma_{11} = &\left(\cos\varphi - \frac{Lk}{2}\sin\varphi\right)^2 \sigma_{11}^{(0)} + \\ &2\left(\cos\varphi - \frac{Lk}{2}\sin\varphi\right)\left(\frac{2}{k}\sin\varphi + L\cos\varphi\right)\sigma_{12}^{(0)} + \\ &\left(\frac{2}{k}\sin\varphi + L\cos\varphi\right)^2 \sigma_{22}^{(0)}. \end{aligned} \tag{46}$$

However, unlike in thin lens approximation where Eq. 45 becomes a parabolic function, in thick lens method one has to use the equation as it is. For many measurements of the

beam sizes (σ_{11}) over the scan, the full transfer matrix from Eq. 45 can be written as [30]

$$\begin{pmatrix} \sigma_{11v}^{(a)} \\ \sigma_{11v}^{(b)} \\ . \\ . \\ . \\ \sigma_{11v}^{(N)} \end{pmatrix} = \begin{pmatrix} M_{11}^{2(a)} & 2M_{11}^{(a)}M_{12}^{(a)} & M_{12}^{2(a)} \\ M_{11}^{2(b)} & 2M_{11}^{(b)}M_{12}^{(b)} & M_{12}^{2(b)} \\ . & & \\ . & & \\ . & & \\ M_{11}^{2(N)} & 2M_{11}^{(N)}M_{12}^{(N)} & M_{12}^{2(N)} \end{pmatrix} \begin{pmatrix} \sigma_{11s} \\ \sigma_{12s} \\ \sigma_{22s} \end{pmatrix} = M \begin{pmatrix} \sigma_{11s} \\ \sigma_{12s} \\ \sigma_{22s} \end{pmatrix}, \tag{47}$$

where, v denote the beam size at the viewer and s denotes the beam parameters at the solenoid for each measurements from (a) to (N). The solution to this equation can be written as

$$\begin{pmatrix} \sigma_{11s} \\ \sigma_{12s} \\ \sigma_{22s} \end{pmatrix} = (M^T M)^{-1} M^T \begin{pmatrix} \sigma_{11v}^{(a)} \\ \sigma_{11v}^{(b)} \\ . \\ . \\ . \\ \sigma_{11v}^{(N)} \end{pmatrix}. \tag{48}$$

The error of the measurement can be minimized by employing a least-squares fit to the data. This can be done by χ^2 minimization where the χ^2 function is given as [30]

$$\chi^2 = \sum_{n=1}^{N} \left(\frac{y_i - f(x_i, \alpha)}{\delta_i} \right)^2, \tag{49}$$

where $f(x_i, \alpha)$ is any function (fit model) with independent variable x_i and fit parameter α. y_i is the ultimate measured function value (the dependent variable), δ_i is the estimated error of y_i, and N is the number of data points. The fit parameters can be found by minimizing χ^2 with respect to fit parameters. The calculation method goes as follows.

For each i^{th} measurement there is an equivalent transfer matrix $M(i)$, rms beam size $\sigma_{ii}(i)$, and estimated error on the beam size $\delta_(i)$. Applying χ^2 function into our situation for N measurements, Eq. 49 can be re-written as

$$\chi^2 = \sum_{n=1}^{N} \left(\frac{\sigma_{11}(i) - (M_{11}^2(i)\sigma_{11}^{(0)} + 2M_{11}(i)M_{12}(i)\sigma_{12}^{(0)} + M_{12}^2(i)\sigma_{22}^{(0)})}{\delta_i} \right)^2. \tag{50}$$

The minimization of the χ^2 can be done by obtaining the derivative of χ^2 with respect

to σ_{11}, σ_{12} and σ_{22} and equating it to zero as follows

$$\begin{aligned}\frac{\partial \chi^2}{\sigma_{11}^{(0)}} &= 2\sum_{i=1}^{N} \frac{\left(M_{11}^2(i)\sigma_{11}^{(0)} + 2M_{11}(i)M_{12}(i)\sigma_{12}^{(0)} + M_{12}^2(i)\sigma_{22}^{(0)}\right)}{\delta_i} M_{11}^2(i) \\ &\quad - 2\sum_{i=1}^{N} \frac{\sigma_{11}(i)}{\delta_i} M_{11}^2(i) = 0,\end{aligned} \tag{51}$$

$$\begin{aligned}\frac{\partial \chi^2}{\sigma_{12}^{(0)}} &= 4\sum_{i=1}^{N} \frac{\left(M_{11}^2(i)\sigma_{11}^{(0)} + 2M_{11}(i)M_{12}(i)\sigma_{12}^{(0)} + M_{12}^2(i)\sigma_{22}^{(0)}\right)}{\delta_i} M_{11}(i)M_{12}(i) \\ &\quad - 2\sum_{i=1}^{N} \frac{\sigma_{11}(i)}{\delta_i} M_{11}(i)M_{12}(i) = 0,\end{aligned} \tag{52}$$

$$\begin{aligned}\frac{\partial \chi^2}{\sigma_{22}^{(0)}} &= 2\sum_{i=1}^{N} \frac{\left(M_{11}^2(i)\sigma_{11}^{(0)} + 2M_{11}(i)M_{12}(i)\sigma_{12}^{(0)} + M_{12}^2(i)\sigma_{22}^{(0)}\right)}{\delta_i} M_{12}^2(i) \\ &\quad - 2\sum_{i=1}^{N} \frac{\sigma_{11}(i)}{\delta_i} M_{12}^2(i) = 0.\end{aligned} \tag{53}$$

By rewriting the above equations in matrix format

$$\begin{pmatrix} \sum \frac{M_{11}^4(i)}{\delta_i^2} & \sum \frac{2M_{11}^3(i)M_{12}(i)}{\delta_i^2} & \sum \frac{M_{11}^2(i)M_{12}^2(i)}{\delta_i^2} \\ \sum \frac{2M_{11}^3(i)M_{12}(i)}{\delta_i^2} & \sum \frac{4M_{11}^2(i)M_{12}^2(i)}{\delta_i^2} & \sum \frac{2M_{11}(i)M_{12}^3(i)}{\delta_i^2} \\ \sum \frac{M_{11}^2(i)M_{12}^2(i)}{\delta_i^2} & \sum \frac{2M_{11}(i)M_{12}^3(i)}{\delta_i^2} & \sum \frac{M_{12}^4(i)}{\delta_i^2} \end{pmatrix} \begin{pmatrix} \sigma_{11}^0 \\ \sigma_{12}^0 \\ \sigma_{22}^0 \end{pmatrix} = \begin{pmatrix} \sum \frac{M_{11}^2(i)\sigma_{11}(i)}{\delta^2(i)} \\ \sum \frac{2M_{11}(i)M_{12}(i)\sigma_{11}(i)}{\delta^2(i)} \\ \sum \frac{M_{12}^2\sigma_{11}(i)}{\delta^2(i)} \end{pmatrix}. \tag{54}$$

This equation can be simplified as $Ma = b$, where M is called the curvature matrix, a is the coefficient matrix which contains the beam matrix elements at the solenoid, and b is the matrix containing the sum of the product of the measured beam sizes and the transfer matrix elements. Hence, x can be found by

$$a = M^{-1}b. \tag{55}$$

And from those solutions the emittance and the Twiss parameters can be written as

$$\epsilon_{x,rms} = \sqrt{\sigma_{11}\sigma_{22} - \sigma_{12}^2}, \tag{56}$$

$$\beta_x = \frac{\sigma_{11}}{\sqrt{\sigma_{11}\sigma_{22} - \sigma_{12}^2}}, \tag{57}$$

$$\alpha_x = -\frac{\sigma_{12}}{\sqrt{\sigma_{11}\sigma_{22} - \sigma_{12}^2}}, \tag{58}$$

$$\gamma_x = \frac{\sigma_{22}}{\sqrt{\sigma_{11}\sigma_{22} - \sigma_{12}^2}}. \tag{59}$$

Next, we will use this solutions to find the error in the measurement. The squared error of a function $g(x_1, x_2, ..., x_n)$ via error propagation is given as below

$$\sigma_g^2 = \sum_{i=1}^{n} \left(\frac{\partial g}{\partial x_i}\right)^2 \sigma_{x_i}^2 + \sum_{i=1}^{n} \sum_{j=1, j\neq i}^{n} \left(\frac{\partial g}{\partial x_i}\right)^2 \left(\frac{\partial g}{\partial x_j}\right)^2 \mathrm{cov}(i,j), \tag{60}$$

where the first sum represents the variances of the function g, the second sum is the contribution of the co-variances. Hence, in order to find the error, the variance and covariances of σ_{11}, σ_{12} and σ_{22} are needed. If a_1, a_2, and a_3 represent σ_{11}, σ_{12}, and σ_{22} respectively, the variance of a_k where $k = 1, 2, 3$ can be written as

$$\sigma_{a_k}^2 = \sum_{i=1}^{n} \left(\frac{\partial a_k}{\partial \sigma_{11}(i)}\right)^2 \delta_i^2. \tag{61}$$

However, simplifying the above equations, there is an easy and often more practical method which mostly use in computer codes as follows. The diagonal elements of the M^{-1} matrix give the variances of a_k and the off-diagonal elements give the covariance terms [30]. If a function f is defined as

$$f = \begin{pmatrix} \beta_x \\ \alpha_x \\ \epsilon_{x,rms} \end{pmatrix} = \begin{pmatrix} \frac{a_1}{\sqrt{a_1 a_3 - a_2^2}} \\ -\frac{a_2}{\sqrt{a_1 a_3 - a_2^2}} \\ \sqrt{a_1 a_3 - a_2^2} \end{pmatrix}. \tag{62}$$

The errors on the emittance and Twiss parameters can be calculated by using M^{-1} and Eq. 62 where the diagonal elements of the error matrix $\sigma(f)^2$ contain the squared errors of

the emittance and Twiss parameters

$$\sigma(f)^2 = (\nabla_a f)^T M^{-1} (\nabla_a f) = \begin{pmatrix} \sigma_{\beta_x}^2 & \dots & \dots \\ \dots & \sigma_\alpha^2 & \dots \\ \dots & \dots & \sigma_{\epsilon_{x,g}^2} \end{pmatrix}. \tag{63}$$

3.6 BEAM ENVELOPE

Beam envelope describes the beam size as a whole with maximum transverse position it can achieved. Equation for the beam envelope can be obtained by using the solution for the Hill's equation, for a particular particle, i with arbitrary phase ψ_i [25]

$$x_i = \sqrt{\epsilon\beta}\,\cos(\psi + \psi_i). \tag{64}$$

The maximum transverse position occurs when $\cos(\psi + \psi_i) = \pm 1$. Thus, the beam envelope ($E(s)$) containing all the particles can be found by selecting the particle i that satisfies the above condition along the beamline.

$$E(s) = \pm\sqrt{\epsilon\beta}. \tag{65}$$

Here the $\pm$ indicates that there is an envelope on either side of the beam center. All the other particles which have $|\cos(\psi + \psi_i)| \leq 1$ contained in

$$-\sqrt{\epsilon\beta} \leq x_i \leq \sqrt{\epsilon\beta}. \tag{66}$$

Hence, the beam envelope is determined by the beam emittance and the beta function where the beam emittance is a constant of motion and resembles the transverse "temperature" of the beam, and the beta function reflects exterior forces from focusing magnets.

3.7 BEAM DYNAMICS OF A SOLENOID

The solenoids are used in beam focusing in the low-energy section of the accelerators. It is also used in generating angular momentum-dominated beams, as mainly discussed in this project.

In a simple solenoid, the longitudinal magnetic field B_z on the axis is peaked at the center of the solenoid, decreases toward the ends, and approaches zero far from the solenoid. In contrast, the radial magnetic field B_r is peaked near the ends of the solenoid as shown in Fig. 32 [31].

Basically, the longitudinal magnetic field is assumed to be uniform inside the solenoid. A rotationally symmetric magnetic fields can be expanded in a polynomial series as [32]

$$\begin{aligned} B_z(r,z) &= B(z) - \frac{r^2}{4}B''(z) + ..., \\ B_r(r,z) &= -\frac{r}{2}B'(z) + \frac{r^3}{16}B'''(z) + ..., \\ B_\theta(r,z) &= 0. \end{aligned} \tag{67}$$

where z is the distance along the solenoid axis, r is the radial distance from the solenoid axis, and the prime denotes a derivative with respect to z. Let us keep only terms up to the first-order term in r. The magnetic field of an infinity long solenoid is given by $B_z = \mu_0 IN/L$ where μ_0 is the permeability of free space, N/L is the number of turns per unit length, and I is the current passing through the solenoid.

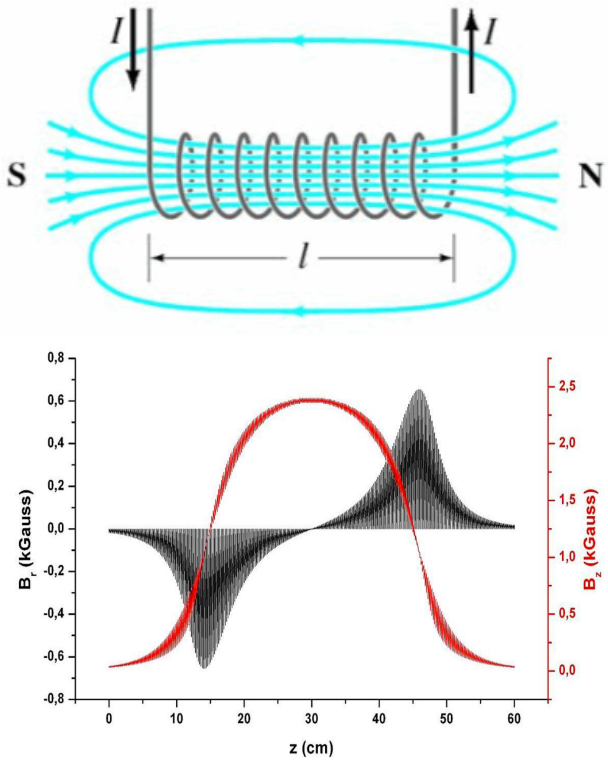

FIG. 32: B_z and B_r of a solenoid.

In order to understand some of the exciting aspects of beam dynamics in a solenoid magnetic field, let us consider the Lagrangian function for a relativistic particle in an electromagnetic field [33].

$$L = -mc^2(1-\beta^2)^{1/2} - q\phi + q\vec{v}.\vec{A}, \tag{68}$$

where $\beta = \frac{v}{c}$, ϕ scaler potential and A vector potential. It can be rewritten in cylindrical coordinates as

$$L = -mc^2\Big[1 - \frac{\dot{r}^2 + r^2\dot{\theta}^2 + \dot{z}^2}{c^2}\Big]^{1/2} - q\phi + q(\dot{r}A_r + r\dot{\theta}A_\theta + \dot{z}A_z). \tag{69}$$

The canonical momenta is defined as

$$p_i = \frac{\partial L(q_i, \dot{q_i}, t)}{\partial \dot{q}_i}. \tag{70}$$

Therefor, the three canonical momentum components are

$$p_r = \frac{\partial L}{\partial \dot{r}} = \gamma m\dot{r} + qA_r, \tag{71}$$

$$p_\theta = \frac{\partial L}{\partial \dot{\theta}} = \gamma m r^2\dot{\theta} + qrA_\theta, \tag{72}$$

$$p_z = \frac{\partial L}{\partial \dot{z}} = \gamma m\dot{z} + qA_z. \tag{73}$$

The Hamiltonian for charged particles in cylindrical coordinates for relativistic case can then be obtained from above equations as below

$$H = \Sigma_i \dot{q}_i \frac{\partial L}{\partial \dot{q}_i} - L, \tag{74}$$

$$H = c\Big[m^2c^2 + (p_r - qA_r)^2 + \Big(\frac{p_\theta - qrA_\theta}{r}\Big)^2 + (p_z - qA_z)^2\Big]^{1/2} + q\phi. \tag{75}$$

The Hamiltonian represents the total energy which in this case is a constant of motion. Identifying the cyclic variables

$$\frac{dp_j}{dt} = -\frac{\partial H}{\partial q_j} = 0, \tag{76}$$

where the canonical momentum variable p_j is a constant of the motion. As a result of this in systems with cylindrical symmetry the Hamiltonian is independent of the azimuth coordinate θ

$$\frac{dp_\theta}{dt} = -\frac{\partial H}{\partial \theta} = 0. \tag{77}$$

Therefore,

$$p_\theta = \gamma m r^2 \dot{\theta} + qrA_\theta = \text{constant}. \tag{78}$$

This represents the conservation of canonical angular momentum, which is also known as Busch's theorem. The theorem states that the canonical angular momentum of a charged particle moving in an axially symmetric magnetic field is conserved. This is very useful in the analysis of particle dynamics in axially symmetric fields.

The magnetic flux enclosed by the particle trajectory *i.e.*, the flux inside a circle with radius r given by the radial distance r' of the particle from the axis at a given position along the trajectory can be written as

$$\psi = \int \vec{B}.d\vec{S} = \int (\nabla \times \vec{A}).d\vec{S} = \oint \vec{A}.d\vec{l} = 2\pi r A_\theta. \tag{79}$$

Therefore Eq. 78 can be rewritten as ,

$$\gamma m r^2 \dot{\theta} + \frac{q}{2\pi}\psi = \text{constant}. \tag{80}$$

Applying the conservation of canonical momentum, for a particle that launched in a region where, $\boldsymbol{B} = 0$, no initial velocity in azimuthal direction

$$\gamma m r^2 \dot{\theta} = -\frac{r^2}{2c} e B_z, \tag{81}$$

$$\omega_L = -\frac{qB_z}{2\gamma m}, \tag{82}$$

which is called the Larmor frequency, where $\psi = \pi r^2 B_z$. When a charged particle enters from the field-free region to a uniform magnetic field region in a solenoid, it starts rotating with the Larmor frequency. The relation between cyclotron frequency and Larmar frequency is given by $\omega_L = \omega_c/2$. Cyclotron frequency is the frequency that particles rotate around the center of their individual trajectories, and Larmar frequency is the frequency that particles rotate around the solenoid axis [32].

In order to describe the transverse motion of charged particles in an axisymmetric system for particles of constant velocity, let us consider the linear terms in Eq. 67.

$$\boldsymbol{F} = m\gamma\ddot{\mathbf{x}} = q\dot{\mathbf{x}} \times \mathbf{B}. \tag{83}$$

In cylindrical coordinates,

$$m\gamma(\ddot{r} - r\dot{\theta}^2) = qr\dot{\theta}B. \tag{84}$$

Substituting $\dot{\theta}$ from Eq. 72 and simplifying

$$\gamma\ddot{r} = \frac{p_\theta^2}{\gamma m^2 r^3} - \frac{r}{4\gamma}\left(\frac{qB}{m}\right)^2. \tag{85}$$

In order to follow the usual notation, the derivation with respect to the longitudinal coordinate, form Lorentz factor

$$\begin{aligned} \dot{r} &= r'\beta_z c, \\ \ddot{r} &= r''(\beta_z c)^2. \end{aligned} \tag{86}$$

By substituting these yield

$$r'' + \left(\frac{qB}{2mc\beta\gamma}\right)^2 r - \left(\frac{p_\theta}{mc\beta\gamma}\right)^2 \frac{1}{r^3} = 0, \tag{87}$$

where r'' represents the change of slope of the particle trajectory, the second term represents the transverse confining force from the magnetic, and the third term represents the centrifugal de-confining force due to the canonical angular momentum, p_θ. This equation including the effect of the electric field and self fields is called the paraxial ray equation.

Applying this equation of motion for a particle coming parallel to the axis from outside of the solenoid, $A_\theta = 0$, $\dot{\theta} = 0$ thus, $p_\theta = 0$. Then the above equation deduced to harmonic oscillator with $r'' + kr = 0$ where, k becomes the focusing strength. Hence, solenoid starts acting as a focusing device. Assuming the thin lens approximation, where r is constant in the vicinity of the solenoid the focal length can be obtained by

$$\frac{1}{f} = -\frac{r'}{r} = \int \left(\frac{qB}{2p_z}\right)^2 dz. \tag{88}$$

Further, the focusing occurs with rotational symmetry as this equation is independent of θ. Also, more importantly, the focal length is proportional to the square of the momentum. Thus, focusing on solenoids is more effective for low-energy sections.

3.7.1 EMITTANCE ASSOCIATED WITH THE ANGULAR MOMENTUM DOMINATED BEAM

The total transverse emittance associated with the angular momentum dominated beam is given by

$$\epsilon_{x,rms} = \sqrt{\epsilon^2_{correlated} + \epsilon^2_{uncorrelated}} \, . \tag{89}$$

where the uncorrelated emittance combining the effect of thermal, space charge components and the correlated emittance, which represents the magnetization [34, 35].

In order to obtain a relationship for correlated emittance, consider the full paraxial envelope equation with self fields [33]

$$r'' + \frac{\gamma'}{\gamma\beta^2}r' + \frac{\gamma''}{2\gamma\beta^2}r + \left(\frac{qB}{2mc\beta\gamma}\right)^2 r - \left(\frac{p_\theta}{mc\gamma\beta}\right)^2 \frac{1}{r^3} - \left(\frac{\epsilon_n}{\beta\gamma}\right)^2 \frac{1}{r^3} - \frac{K}{r} = 0, \tag{90}$$

where $K = \dfrac{I}{I_0}\dfrac{2}{\beta^3\gamma^3}$ is the generalized perveance, which indicates how significant the space charge effect is on the beam's motion and I is the beam current and $I_0 = \dfrac{4\pi\epsilon_0 mc^3}{q} \approx \dfrac{1}{30}\dfrac{mc^2}{q} \approx 17$ kA for electron is the characteristic current. The additional second term contains the effect of the axial electric field (acceleration or deceleration), the third term that of the radial electric field (focusing, defocusing). Further, the sixth term represents the emittance variations, and the last term represents the space charge effect. When $B \neq 0$ at the cathode, then from Busch's theorem, $p_\theta = \dfrac{1}{2}eB_z r^2$ where B_z and r are the longitudinal magnetic field and the beam radius at the cathode, respectively.

According to the above equation, the emittance term has the same $\dfrac{1}{r^3}$ dependence as the angular momentum term, which are repulsive forces tending to diverge the beam. If we equate the two terms

$$\left(\frac{p_\theta}{mc\gamma\beta}\right)^2 \frac{1}{r_m^3} = \left(\frac{\epsilon_n}{\beta\gamma}\right)^2 \frac{1}{r_m^3}, \tag{91}$$

$$\frac{p_\theta}{mc} = \epsilon_n = \gamma\beta\epsilon. \tag{92}$$

The emittance due to magnetization can be written as

$$\epsilon_{correlated} = \frac{eB_z a_0^2}{8m_e c}, \tag{93}$$

which is also called the drift emittance or magnetized emittance.

CHAPTER 4

SPACE CHARGE EFFECTS

The previous chapter discusses how charged particles moving in an accelerator interact with the external electromagnetic fields (Eq. 3). However, in real accelerators the beam itself produces additional electromagnetic fields called "self-fields", which cannot be ignored. Space charge fields are one such field that depends on the intensity of the beam current and the charge distribution. Space charge forces are the Coulomb repulsive forces inside the charge distribution. These space charge forces can disrupt the external fields which guide the beam through the accelerator and cause emittance growth, energy loss, instabilities, etc.

Let us derive the equation for the direct space charge forces in free space. In a uniform cylindrical charge distribution with radius a and longitudinal charge distribution $\lambda(r) = \lambda_0(r/a)^2$ traveling with a relativistic constant velocity $v = \beta c$, the electric and magnetic fields can be computed as below [36]. Applying Gauss's law

$$E_r(2\pi r)\Delta z = \frac{\lambda(r)\Delta z}{\epsilon_0} \rightarrow E_r = \frac{\lambda_0}{2\pi\epsilon_0}\frac{r}{a^2}. \tag{94}$$

Applying Ampere's law

$$B_\phi(2\pi r) = \mu_0 I = \mu_0\beta c\lambda(r) \rightarrow B_\phi = \frac{\lambda_0\beta}{2\pi\epsilon_0 c}\frac{r}{a^2} = \frac{\beta}{c}E_r. \tag{95}$$

Thus, the electromagnetic transverse force acting on a charge inside the beam is given by the Lorentz force.

$$F_r(r) = q(E_r - \beta c B_\phi) = qE_r(1-\beta^2) = \frac{q}{\gamma^2}\frac{\lambda_0}{2\pi\epsilon_0}\frac{r}{a^2}. \tag{96}$$

As per the above equation, the electric force is defocusing the beam, and the magnetic force is focusing the beam. For relativistic particles, the magnetic force almost balances the electric force. However, for non-relativistic particles (low-energy beams near the cathode), the magnetic force is negligible, and the beam spreads rapidly due to the defocusing. Also, this transverse space-charge force is inversely proportional to the bunch dimensions [36].

By applying this to Gaussian charge distribution. The charge density can be written as

$$\rho(r,z) = \frac{q_0}{(\sqrt{2\pi})^3\sigma_z\sigma_r^2}e^{(-z^2/2\sigma_z^2)}e^{(-r^2/2\sigma_r^2)}, \tag{97}$$

where q_0 is the bunch charge σ_z and σ_r are longitudinal and transverse rms beam sizes. Hence, applying Gauss's law

$$E(r,z) = \frac{1}{2\pi\epsilon_0}\frac{q_0}{\sqrt{2\pi}\sigma_z\sigma_r^2 r}e^{(-z^2/2\sigma_z^2)}\int_0^r e^{(-r'^2/2\sigma_r^2)}r'dr', \tag{98}$$

$$E(r,z) = \frac{1}{2\pi\epsilon_0}\frac{q_0}{\sqrt{2\pi}\sigma_z}e^{(-z^2/2\sigma_z^2)}\left[\frac{1-e^{(-r^2/2\sigma_r^2)}}{r}\right]. \tag{99}$$

The total force inside the bunch can be written as,

$$F_r(r,z) = qE_r(1-\beta^2) = \frac{q}{2\pi\epsilon_0\gamma^2}\frac{q_0}{\sqrt{2\pi}\sigma_z}e^{(-z^2/2\sigma_z^2)}\left[\frac{1-e^{(-r^2/2\sigma_r^2)}}{r}\right]. \tag{100}$$

For a non-magnetized electron beam, the bunch transverse dimension is small and the charge density is intense, hence the nonlinear space charge force can have a huge effect during acceleration from low to higher energy and during the long drift, which would cause emittance growth. However, for magnetized electron beam, the transverse size is set by the beam's correlated emittance which is controllable and much larger in a drift space and thus the space charge effect is minimal.

4.0.1 SPACE CHARGE CURRENT LIMITATION

When space charge accumulates and forms a cloud of charges next to the cathode, it limits further emission of charges from the surface due to the space charge forces as shown in Fig 33. This is known as the space charge current limitation.

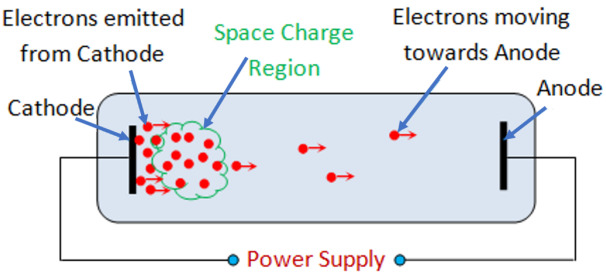

FIG. 33: Illustration of the space charge current limitation.

Child and Langmuir first studied the maximum current density J that can be transported from an infinite planar cathode at zero potential to an infinite planar anode parallel to the cathode at a distance d and fixed potential difference V when the initial velocity of electrons at the cathode is zero, due to the space charge limitations. The equation for J can be obtained by using the 1D Poisson's equation $\nabla^2\phi = \frac{d^2\phi}{dx^2} = -\rho/\epsilon_0$ with the continuity equation $J = \rho\dot{x}$ = constant and equation of motion $m/2\dot{x}^2 = q\phi(x)$ [37]. Hence,

$$\dot{x} = \left[\frac{2e\phi(x)}{m}\right]^{1/2}. \tag{101}$$

By substituting Eq. 101 and $\rho = J/\dot{x}$ in to Poisson's equation yields

$$\frac{d^2\phi}{dx^2} = \frac{J}{\epsilon_0(2e/m)^{1/2}}\frac{1}{\phi^{1/2}}. \tag{102}$$

In order to solve for ϕ first, let us multiply both sides with $d\phi/dx$ and integrate.

$$\left(\frac{d\phi}{dx}\right)^2 = \frac{4J}{\epsilon_0(2e/m)^{1/2}}\phi^{1/2} + C. \tag{103}$$

Applying boundary conditions, $\phi = 0$ at $x = 0$ and $d\phi/dx = 0$ at $x = 0$ and simplifying

$$\frac{4}{3}\phi^{3/4} = 2\left(\frac{J}{\epsilon_0}\right)^{1/2}\left(\frac{2e}{m}\right)^{-1/4}x. \tag{104}$$

Further, at $x = d$ $\phi = V$. Thus,

$$J = \frac{4\epsilon_0}{9d^2}\sqrt{\frac{2e}{m}}V^{3/2}. \tag{105}$$

Thus, the current can be increased by either increasing the voltage or decreasing the cathode anode spacing. Furthermore, Eq. 105 assumes an infinite charge plane (1D). Modification to Child's law due electron emission from a finite circular spot on the cathode (2D) is discussed in [38] and the effect of short bunches is presented in [39].

The charge saturation (current limitation) at the photocathode can be explained by combining the space charge effect and Fowler-Nordheim limit, which gives the maximum current density extracted from a surface under a given electric field, by treating the emission of electrons from a metal-vacuum interface, in the presence of an electric field normal to the surface, as a quantum mechanical tunneling process

$$J(s) = \frac{AE(s)^2}{\phi_w t^2(y)}\exp\left[\frac{-Bv(y)\phi_w^{3/2}}{E(s)}\right], \tag{106}$$

where, $y = (eE(s)/4\pi\epsilon)^{(1/2)}/\phi_w$ where $E(s)$ is the standard component of an electric field at cathode surface, ϕ_w is the work function of the metal, A and B are constants, and $v(y)$ and $t(y)$ represent the effect due to image charge effects. Image charges can be defined as the fields of the bunch including the (cathode) boundary condition minus the fields of the bunch in free space [40].

Space charge accumulates at the cathode suppresses the surface field, and thus, following the reduced surface field, fewer particles will be injected according to the Fowler-Nordheim equation. When the electric field from the emitted charge balances the surface charge, saturation occurs [40].

CHAPTER 5

CHARACTERIZATION OF THE MAGNETIZED ELECTRON BEAM

Characterization of the magnetized electron beam was first done by measuring the transverse *rms* beam sizes ($\sigma_1, \sigma_2, \sigma_3$), and calculating the rotation angles (shearing angles) while varying the magnetic field at the photocathode. Measurements were compared with the simulations done using A Space Charge Tracking Algorithm (ASTRA) and General Particle Tracer (GPT) programs. Post-processing was carried out with MATLAB software. Further, conservation of canonical angular momentum was verified using GPT simulation results. The drift emittance was measured using a single solenoid scan method by varying the magnetic field at the photocathode for different laser spot sizes, voltages, and simulated using GPT software. Finally, a high average current magnetized beam up to 28 mA was demonstrated, and the photocathode lifetime for different magnetized electron beam currents was investigated. The following subsections will discuss each measurement and simulation technique used and high current run results in detail.

5.1 BEAM SIZE VARIATION WITH THE CATHODE MAGNETIC FIELD

5.1.1 EXPERIMENTAL METHOD AND SIMULATIONS

In order to measure the transverse beam sizes along the beamline, 3 YAG screens were used. Cathode magnetic field was varied from 0 to 0.15 T by changing the solenoid current from 0 to 400 A. Beam sizes were measured at 300 kV biased voltage, 1 fC bunch charge, 22 ps rms pulse width, 0.301 mm rms laser spot size, which was displaced from the center by 0.5 mm in the vertical direction, and without engaging any beamline solenoids. Figure 34 shows the beam on the viewer 1 and σ_x and σ_y values according to the Gaussian fit. The final beam size was calculated by $\sigma = \sqrt{\sigma_x \sigma_y}$. Figure 35 shows the beam on three viewers viewer 1 (a), viewer 2 (b), and viewer 3 (c) at 0 A.

Occasionally the magnetized beam got distorted and ended up in a non-circular shape (mostly elliptical shape), as shown in Fig. 36. This occurs mainly when the beam is not

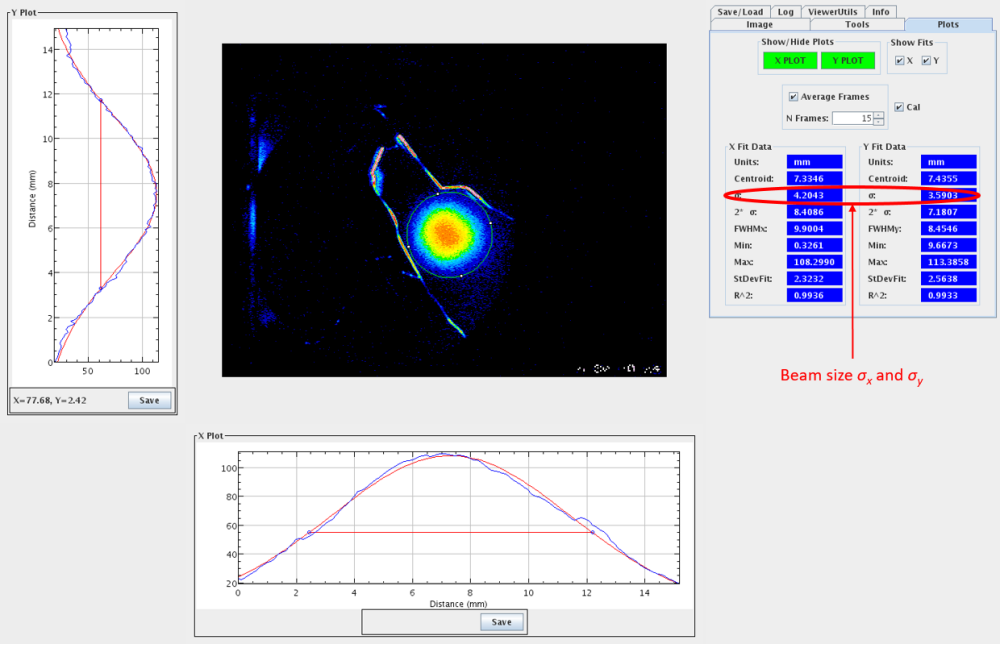

FIG. 34: Beam on the viewer 1 and σ_x and σ_y values.

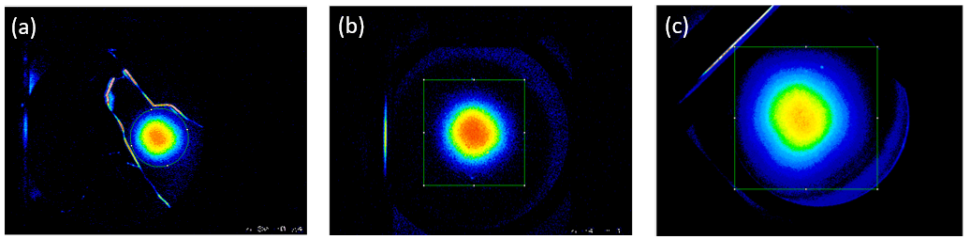

FIG. 35: Beam on 3 viewers (a) viewer 1, (b) viewer 2, and (c) viewer 3 at 0 A.

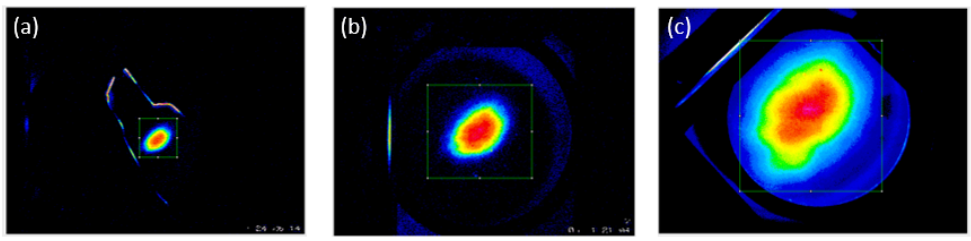

FIG. 36: Beam on 3 viewers (a) viewer 1, (b) viewer 2, and (c) viewer 3 at 200 A.

centered throughout the beamline. Hence, to obtain the correct σ_x and σ_y values, the data files of the beam on the viewers were saved. Then MATLAB was used to rotate them to align the major and minor axes of the ellipse with the x and y axes accordingly [41]. Next, Gaussian fit was applied to obtain the more accurate σ_x and σ_y values.

The beamline was modeled separately using ASTRA and GPT programs, and post-processing was carried out using MATLAB [42]. Simulations required the electric field map of the photo-gun and the magnetic field map of the cathode solenoid. 1D and 3D electrostatic field maps extend from the cathode surface to 0.14 m along the beamline, generated using CST Studio Suite's electromagnetic field solver, and 1D and 2D magnetic field maps extend from the cathode surface till the end of the beamline to cover the entire beampipe radius, generated using Opera software were employed. For ASTRA simulations the 1D electric field and the 1D magnetic field map were used. The radial electric and magnetic field components were deduced from the 1^{st} to 3^{rd} derivatives of the on-axis field, assuming rotational symmetry [43]. The initial particle distribution was created using the program "generator", which comes as a part of the ASTRA suite where the electron bunch emitted from the photocathode is defined in terms of the number of macroparticles, transverse distributions, etc. The transverse beam the size was set to 0.301 mm (Gaussian) with 0.5 mm off-centered in the y-direction. In addition, 300 kV gun high-voltage, 1 fC bunch charge, 0.56 mm mrad/mm initial emittance, and 22 ps rms pulse width were set up as beam parameters. Three YAG screens were included as beamline elements. Further, no beampipe aperture radii were added as it is hard to make the beam centered along the beamline and thus the particle loss cannot be tracked accurately. Hence, ASTRA simulations show the beam size at the three viewers when no beam loss occurs.

In order to visualize the beam profile at each YAG screen location, beam propagation along the beamline, and calculate the beam rms sizes at each YAG screen locations, output files were post-processed using MATLAB. The transverse beam sizes σ_x and σ_y were calculated using the standard deviation of each particle's x-coordinates and y-coordinates respectively.

Simulations were also carried out with GPT software employing a 3D electric field map, and 2D magnetic field map [44]. The 3D electric and 2D magnetic field maps generated were converted to General Datafile Format (GDF) before use in the GPT kernel. Laser profile has a significant impact on simulations when it comes to matching the measurements. Since all the lasers are not proper Gaussian or flat top, a gray-scale bitmap image of the laser profile was implemented as the initial particle distribution using the "SetXYdistbmp" syntax in

GPT (see Appendix A). Figure 37 shows the weighted laser profile with the QE scan and its x and y Gaussian distribution.

In order to make the beam centered, steering magnets were used, and they were optimized for each cathode magnetic field using the "GDFMGO" program, a multi-objective genetic global optimizer. Its primary use is to estimate the optimal trade-off between conflicting objectives [44]. In this simulation, two steering magnets were used to make the beam centered in two different locations in both x and y-directions. All the other beam parameters were set as same as the ASTRA except the initial emittance. Instead of initial emittance, the Mean Transfer Energy (MTE) was included. The MTE is a figure of merit used to characterize the photocathode thermal emittance [18]. The normalized rms transverse emittance at the cathode is given by

$$\epsilon = \sigma\sqrt{\frac{MTE}{m_0c^2}}, \tag{107}$$

where σ is the rms laser spot size, m_0 is the electron rest mass, and c is the speed of light. For a simple photoemission model, the theoretical MTE is defined as

$$MTE = \frac{hv - (E_g + E_a)}{3}, \tag{108}$$

where E_g is the energy gap, E_a is the electron affinity and hv is the photon energy. When $E_g = 1$ eV and $E_a = 1.1$ eV for CsK_2Sb and $hv = 2.326$ eV, $MTE = 75$ meV [18].

In addition, three YAG screens were included, and beampipe radii were added as the beam is centered along the beamline. GPT provides both time and position output. GPT post-processing tools GPTwin, GDFA and GDF2A were used to visualize the beam profiles at various simulation times, extract the beam parameters (stdx, stdy, avgz, etc.) and to get ASCII output files respectively. Figure 38 shows the electron motion of the non-magnetized (left) and magnetized (right) beam.

Figures 39, 40, and 41 show the comparison between measurements, ASTRA and GPT simulations, on beam size variations as a function of cathode solenoid current on viewer 1, viewer 2, and viewer 3 respectively. Simulations are in good agreement with the measurements in all three viewers, specifically till 200 A. The difference between the ASTRA simulations and measurement/GPT simulations in Fig. 41 indicates the beam loss occurs at higher solenoid currents.

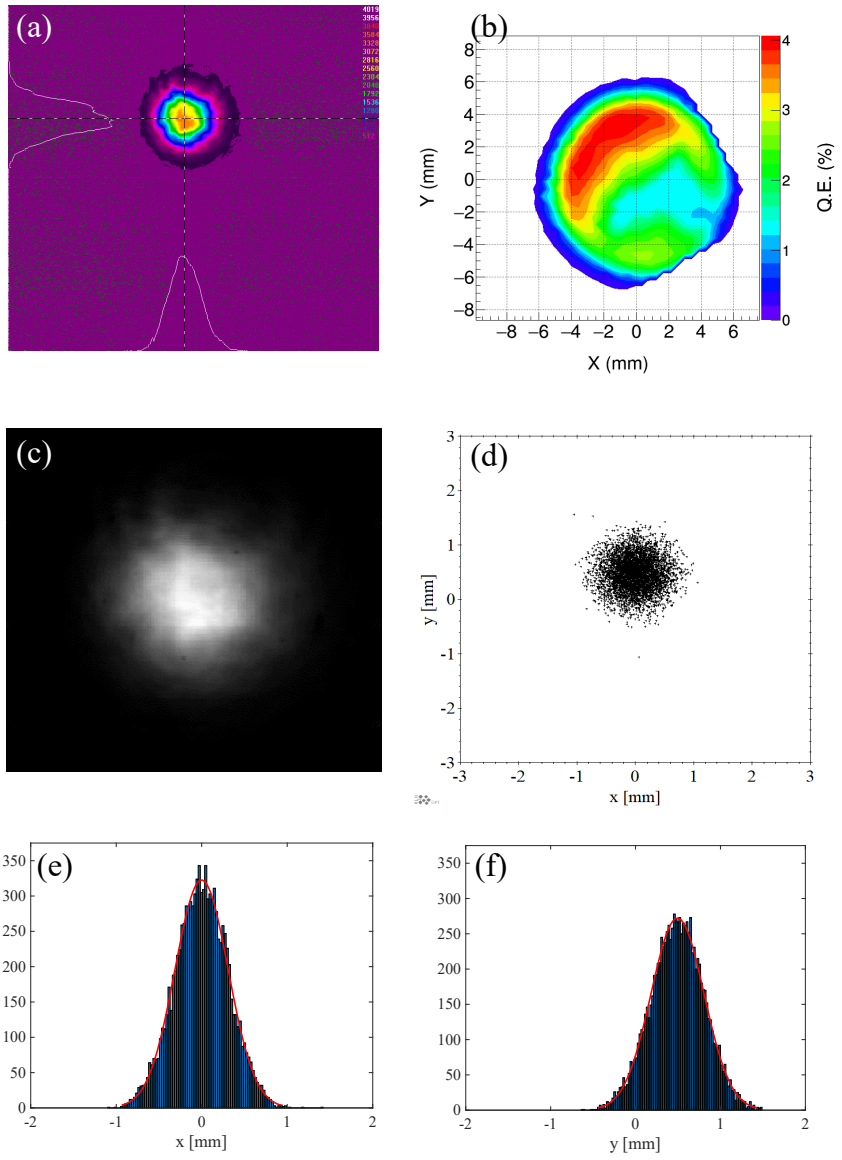

FIG. 37: (a) Laser profile. (b) QE profile. (c) GPT input gray-scale image. (d) Initial particle distribution from the image. (e) x-distribution at the cathode with the Gaussian fit. (f) y-distribution at the cathode with the Gaussian fit.

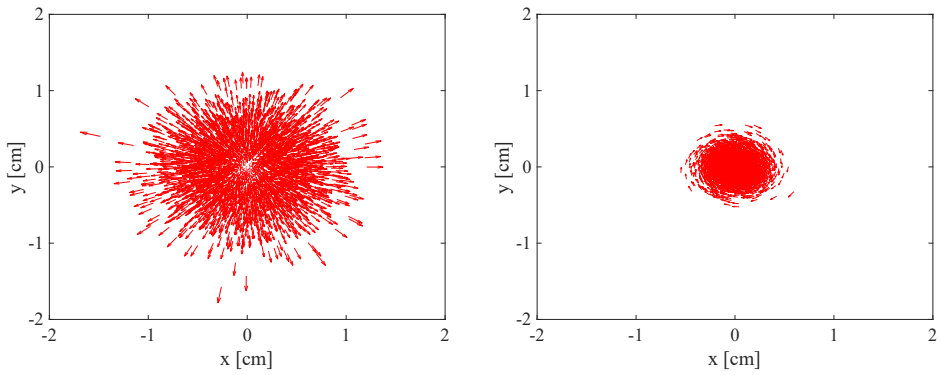

FIG. 38: Non-magnetized beam (left). Magnetized beam (right) for cathode solenoid current 150 A.

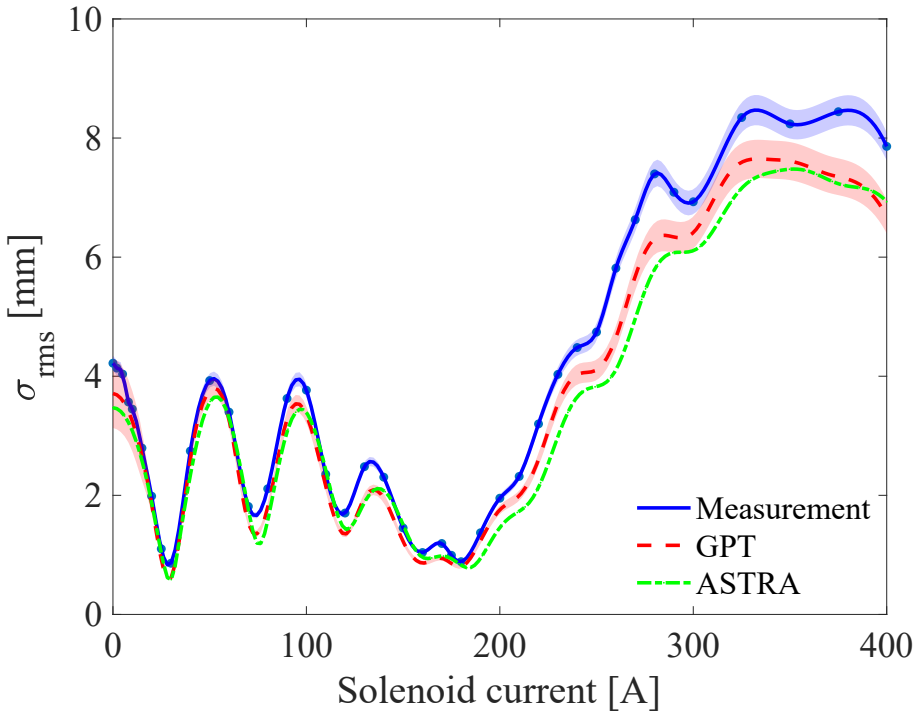

FIG. 39: Beam size variation as a function of solenoid current at viewer 1.

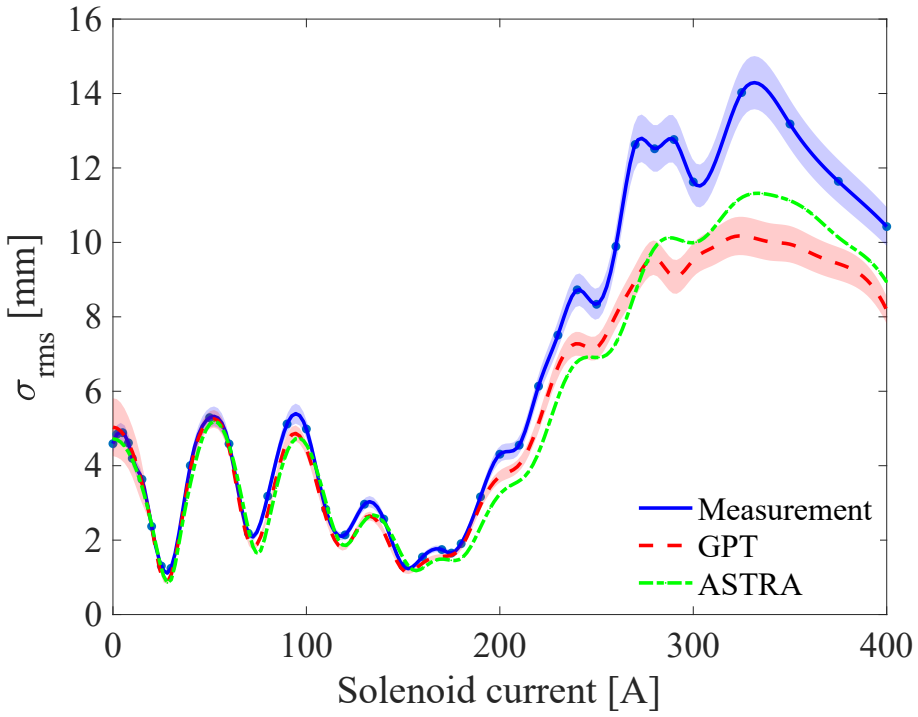

FIG. 40: Beam size variation as a function of solenoid current at viewer 2.

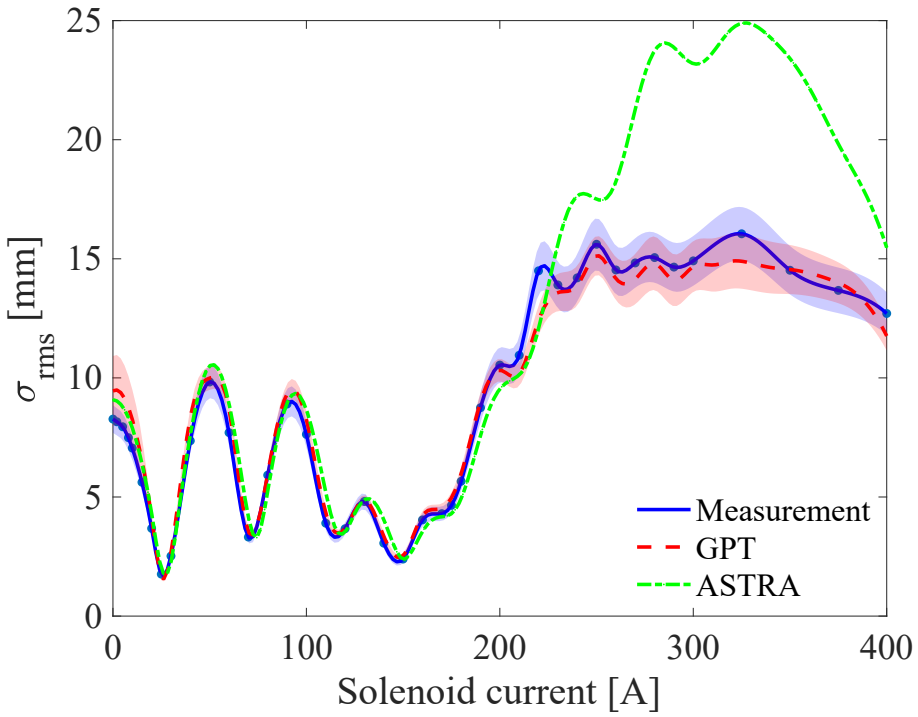

FIG. 41: Beam size variation as a function of solenoid current at viewer 3.

5.1.2 MISMATCH OSCILLATIONS

According to the above plots, the beam size converges and diverges with the solenoid current, a behavior known as mismatch oscillations [33]. This occurs due to the non-uniform magnetic field, as shown in Fig. 23. The magnetic force from the cathode solenoid does not match the initial emittance force, and these imbalanced forces result in repeated focusing of the beam within the solenoid.

Assume a perfect case where the cathode solenoid field is uniform in the longitudinal direction and cylindrically symmetric with a hard edge. Electrons born with a small transverse thermal momentum in this magnetic field make small Larmor motion around the field lines inside the solenoid. Once the beam is outside the solenoid it starts to rotate according to the conservation of canonical angular momentum. However, the cathode solenoid field shown in Fig. 23 is not uniform in the longitudinal direction and does not have a hard edge.

The radial equation of motion for a non-accelerating particle with cylindrical symmetry is given by Eq. 87. The canonical angular momentum can be expressed as

$$p_\theta = \frac{eB_z(z=0)r^2}{2} = w_L(z=0)\gamma m r^2. \tag{109}$$

When $w_L' = 0$, where the magnetic field is longitudinally uniform, $w_L(z) = w_L(0)$. Thus, by substituting w_L and p_θ into Eq. 87 the confining and de-confining terms cancel, $r'' = 0$ and particles move along the field lines.

When $w_L' \neq 0$, $w_L(z) \neq w_L(0)$ and confining and de-confining terms do not cancel out.

$$r'' + \left(\frac{w_L(z)}{\beta c}\right)^2 r - \left(\frac{w_L(z=0)}{\beta c}\right)^2 r = 0. \tag{110}$$

Thus mismatch oscillations occur. Figure 42 shows how beam size varies inside the non-uniform magnetic field for few different solenoid currents. Larger the solenoid current larger the number of oscillations. Figure 43 shows the mismatch oscillations and beam propagation after exciting the magnetic field for a few different solenoid currents.

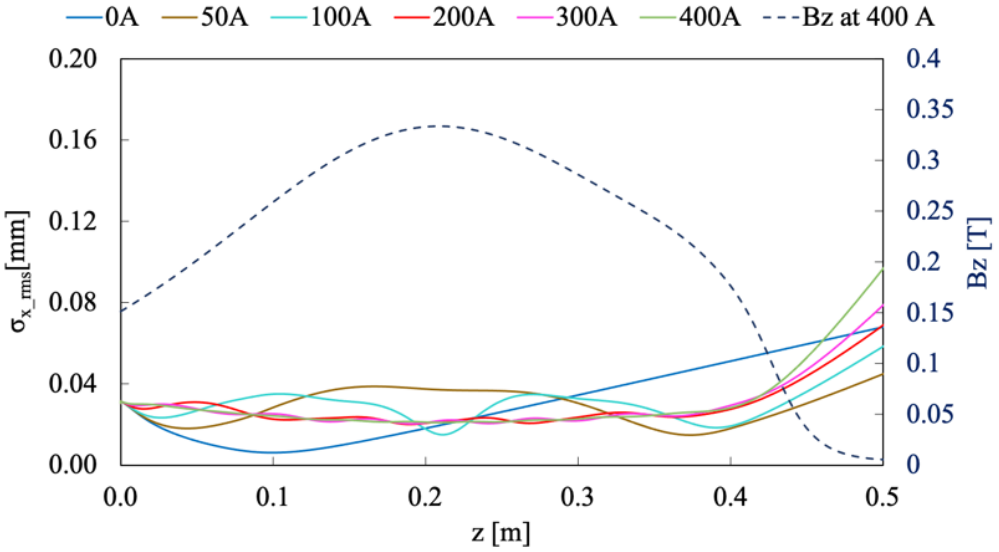

FIG. 42: Mismatch oscillations inside the cathode solenoid.

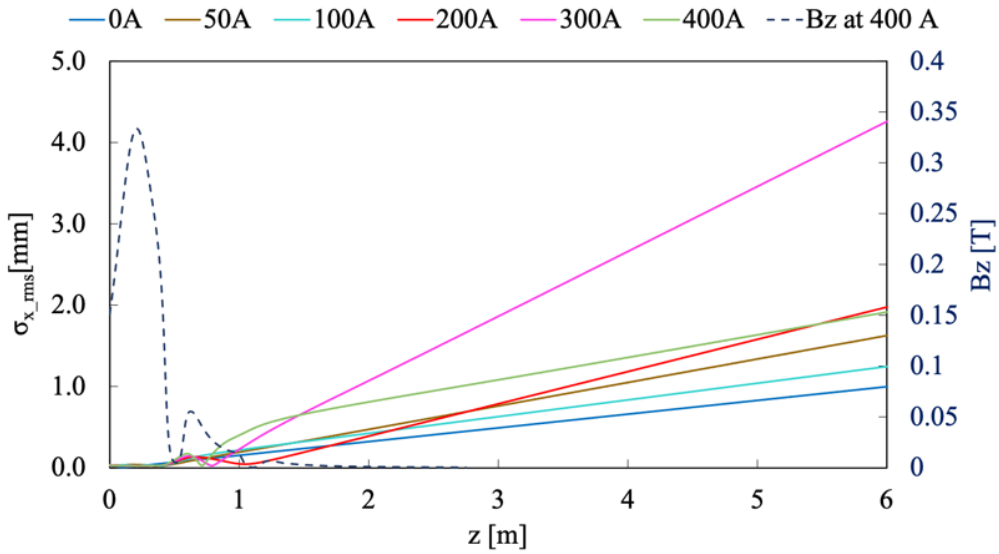

FIG. 43: Beam propagation along the z for different cathode solenoid currents.

5.1.3 ERROR ANALYSIS

Generally, there are two types of errors: systematic errors and statistical errors. Systematic errors are the errors that affect the accuracy of a measurement. These errors can occur due to the incorrect calibration of equipment, improper use of equipment, or failure to account for some effects properly. Systematic errors can be challenging to detect, but they can be reduced only by refining the measurement method or technique once detected. However, these errors cannot be improved by repeating the measurements. The statistical errors are the errors that affect the precision of measurements which can be improved by repeating the measurements but cannot be eliminated. These errors can occur due to lack of sensitivity, noise, etc. Statistical errors displace measurements in an arbitrary direction, whereas systematic errors displace measurements in a single direction.

For the beam size measurements, 3%, 5%, 7% errors were assigned for viewer 1, viewer 2, and viewer 3, respectively, by considering fluctuations in the beam size reading on the EPICS screen and beam loss. For GPT simulations, systematic error analysis was conducted by identifying the possible sources which could cause the errors.

The error caused by the laser profile was calculated by enlarging/reducing the laser profile image by the error percentage assigned. 10% error for MTE and 1% for B_z were applied. In addition, error was calculated by changing the laser position on the photocathode by 1 mm and changing the photocathode recess length to 0.6 mm and to 1 mm (will discuss in the next section).

For each source, the resultant errors were calculated using

$$\frac{\Delta\sigma}{\sigma} = \frac{|\sigma_1 - \sigma_2|}{\left(\frac{\sigma_1 + \sigma_2}{2}\right)}, \tag{111}$$

where σ_1 and σ_2 represent the beam size values with and without the error, respectively. Thus, the total error can be calculated by

$$\left(\frac{\Delta\sigma}{\sigma}\right)_{\text{total}} = \sqrt{\left(\frac{\Delta\sigma_1}{\sigma_1}\right)^2 + \left(\frac{\Delta\sigma_2}{\sigma_2}\right)^2 + \left(\frac{\Delta\sigma_3}{\sigma_3}\right)^2 + \dots}\,. \tag{112}$$

5.1.4 FINDINGS RELATED TO BEAM SIZE MEASUREMENTS

In simulating the beam size measurement, an interesting element that has not been previously paid attention to while doing the experiment was discovered: the photocathode position inside the cathode electrode. How much the photocathode is recessed from the cathode electrode surface can affect the E_z at the photocathode and the beam focusing, and thus it can increase the beam size at the viewers.

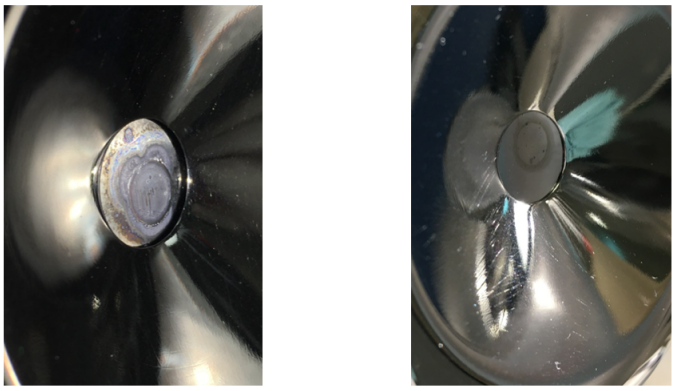

FIG. 44: Photocathode position inside the cathode electrode for GaAs wafer (left). Mo wafer (right).

Ideally, the GaAs surface should be on the same plane as the cathode electrode. Figure 44 (left) shows a recessed photocathode, and (right) shows an almost perfectly fitted photocathode. This can occur mainly due to the thickness of the tantalum cup and when the height of the crown shape in the puck is larger than the height of the combined wafer and tantalum cup.

Figure 45 (a) shows the beam envelope in x-direction for different recess lengths 0 mm (no recess) to 1 mm, and (b) shows the closer look of the beam envelope in x-direction inside the cathode-anode gap. Figure 45 (c) and (d) shows the same for the y-direction. 1 mm recess changed the E_z at the cathode from 2.19 MV/m to 1.67 MV/m at 300 kV, affecting

the space charge current limitations in the high bunch charge delivery.

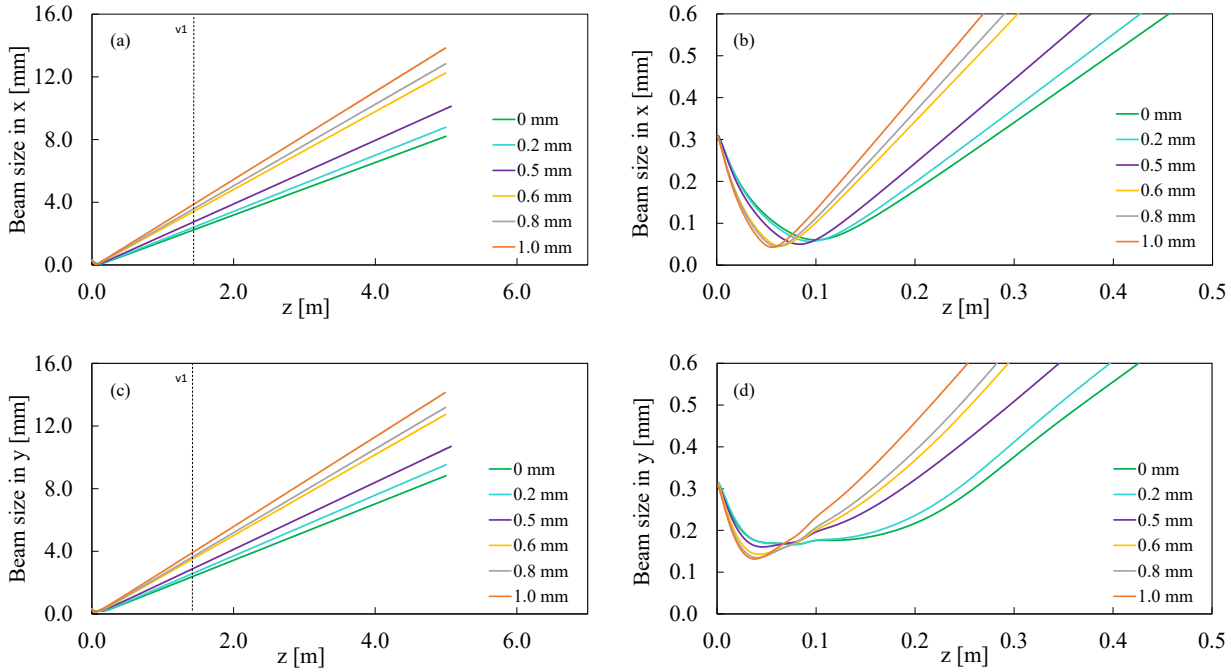

FIG. 45: Beam size variation along the z for different recess lengths (a) in x and (c) in y. Closer look of the beam size variation inside the gun for different recess lengths (b) in x and (d) in y.

5.2 ROTATION ANGLE VARIATION WITH THE CATHODE MAGNETIC FIELD

5.2.1 EXPERIMENTAL METHOD AND SIMULATIONS

Characterization of the magnetized electron beam was continued by measuring the rotation angle (shearing angle). The rotation angle was obtained by inserting a slit at the location of the first YAG screen and measuring the corresponding beamlet angle at the second (slit 1 - viewer 2) and third (slit 1 - viewer 3) screens, and by inserting a slit at the

second YAG screen location and measuring the rotation angle at the third screen (slit 2 - viewer 3). For more accurate results, data tables (.SDDS file) for each case were saved, and angles were calculated using a MATLAB curve fitting tool and ROOT software.

The simulations were done in both ASTRA and GPT programs employing the same Simulation parameters as before [42]. A virtual slit was created at the slit location, and the particles are numerically tracked to the corresponding viewers by assuming p_x and p_y are constant for each particle after they exit electromagnetic fields as no additional forces are acting on them afterward. Linear fits were done for the slit image at the slit location and the viewer location. The rotation angle was calculated from the gradients of the two fits.

Figures 46, 47, and 48 show the measurement, ASTRA and GPT simulations of the rotation variation with the cathode solenoid current for slit 1 - viewer 2, slit 1 - viewer 3, and slit 2 - viewer 3 respectively, along with the beam size variations at the corresponding viewers.

Measurement, ASTRA, and GPT show a good agreement except at 150 - 175 A region. Plots show the conservation of angular momentum, as the beam expands, its angular velocity decreases. Further, results show negative rotation angles (*i.e.* beamlet in 4^{th} quadrant) and large negative rotation angles (*i.e.* beamlet in 3^{rd} quadrant).

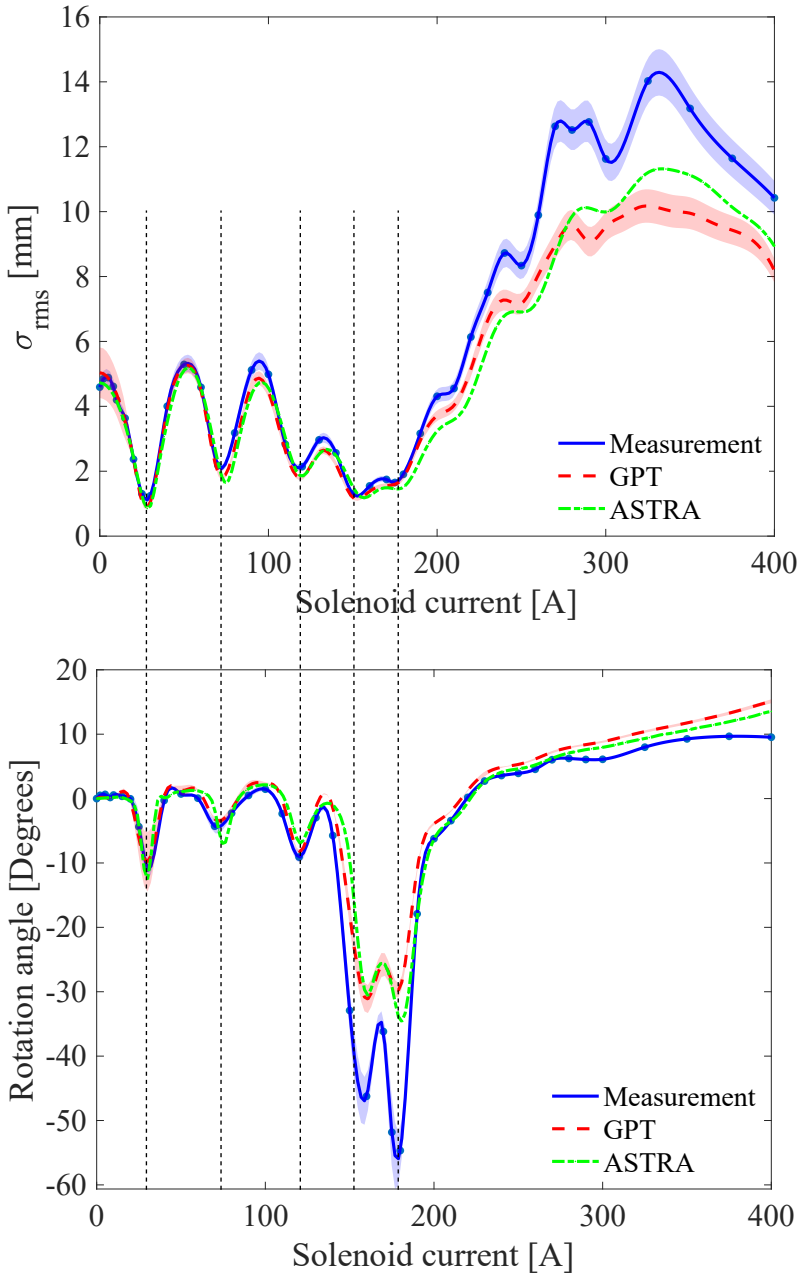

FIG. 46: Beam rms size variation with the cathode solenoid current at viewer 2 (top), rotation angle variation versus cathode solenoid current (bottom) for slit 1 - viewer 2 combination.

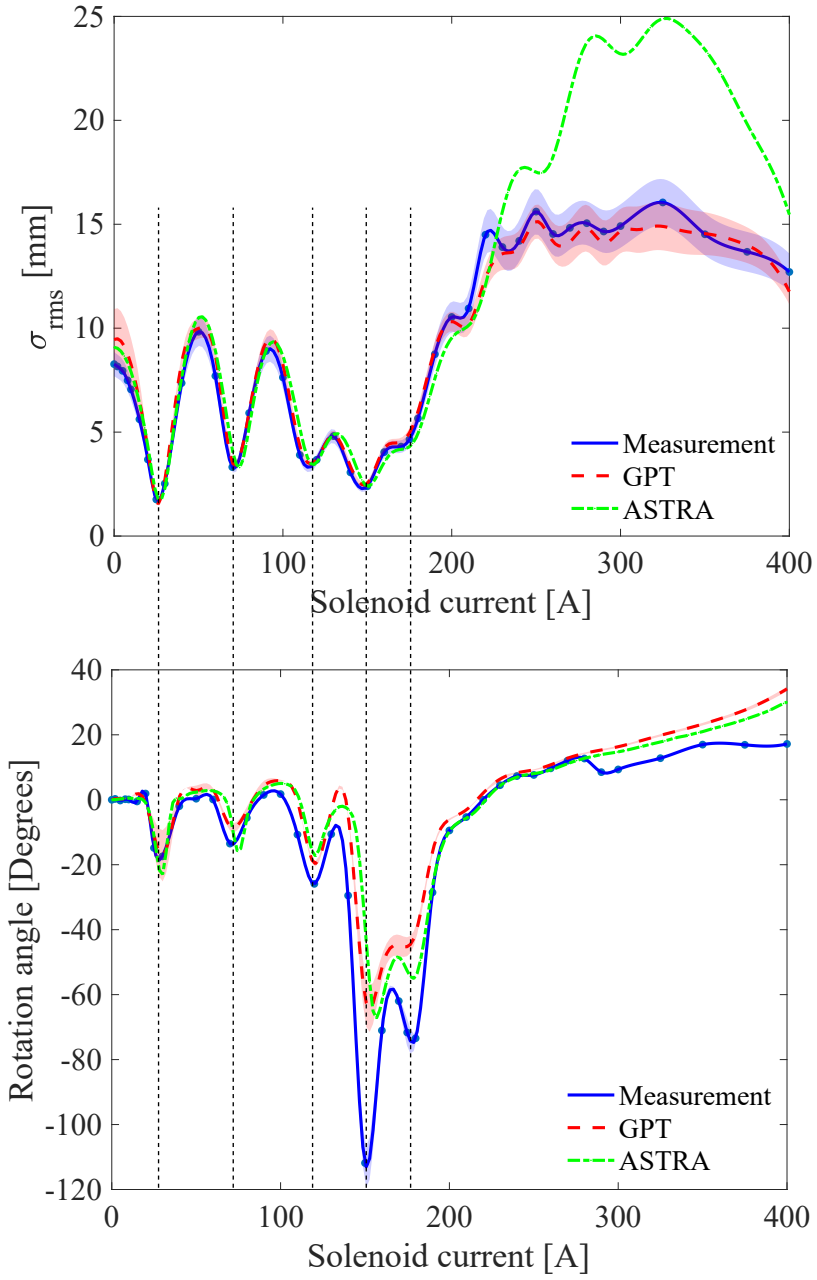

FIG. 47: Beam rms size variation with the cathode solenoid current at viewer 3 (top), rotation angle variation versus cathode solenoid current (bottom) for slit 1 - viewer 3 combination.

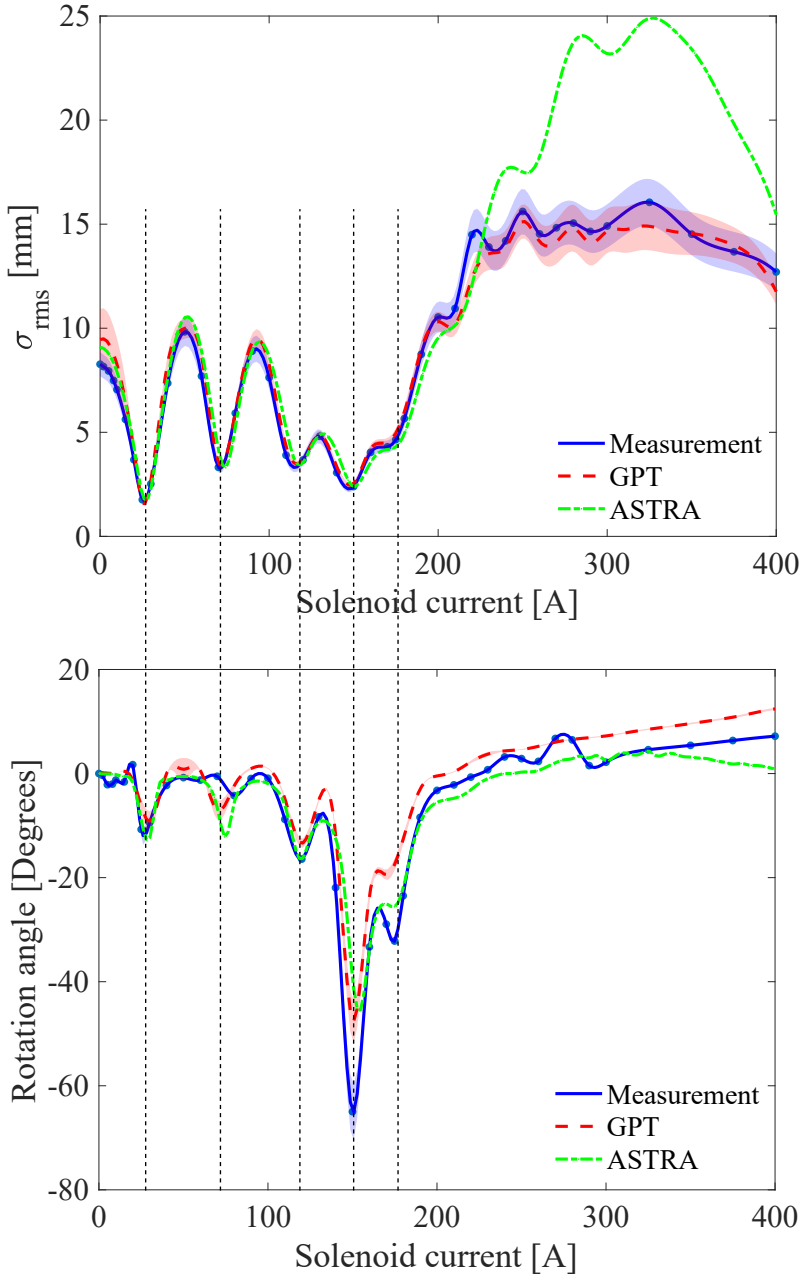

FIG. 48: Beam rms size variation with the cathode solenoid current at viewer 3 (top), rotation angle variation versus cathode solenoid current (bottom) for slit 2 - viewer 3 combination.

Figure 49 shows beam is in the 4^{th} in all three combinations. Figure 50 shows beam is in the 1^{st} quadrant in all three combinations. This can be explained as below.

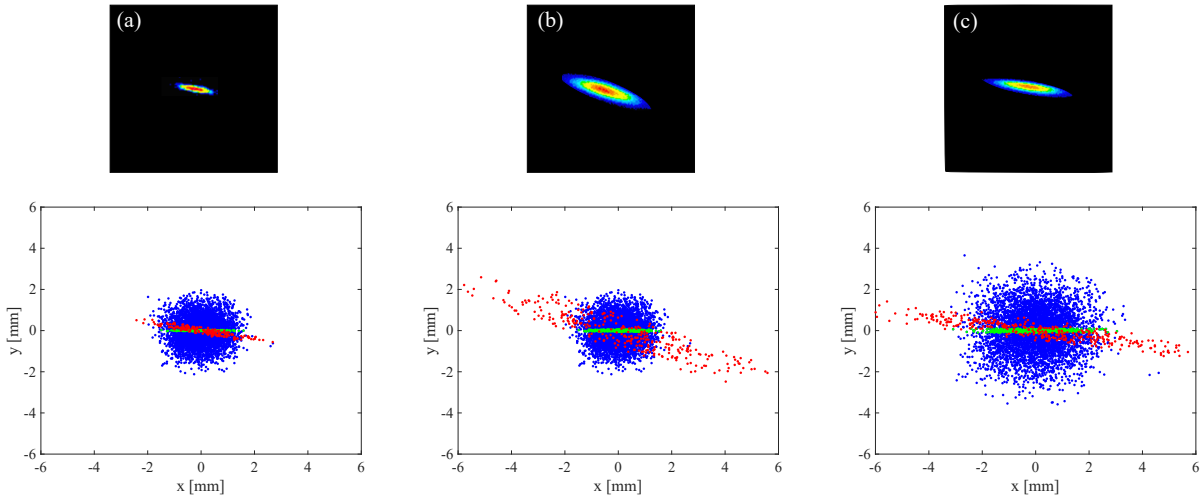

FIG. 49: Beam is in the 4^{th} quadrant (negative angle), measurements (top) and corresponding GPT simulations (bottom), (a): slit 1 - viewer 2, (b): slit 1 - viewer 3, (c): slit 2 - viewer 3 for 30 A.

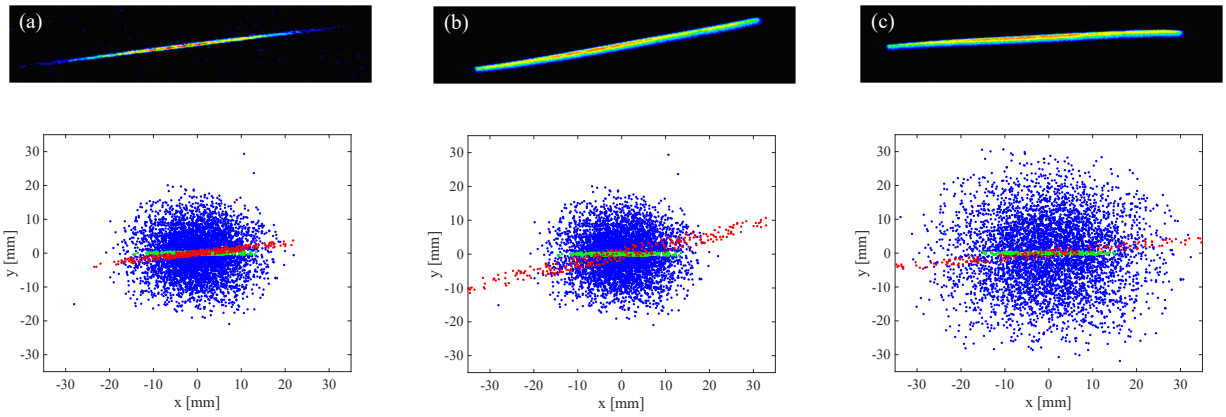

FIG. 50: Beam is in the 1st quadrant, measurements (top) and corresponding GPT simulations (bottom), (a): slit 1 - viewer 2, (b): slit 1 - viewer 3, (c): slit 2 - viewer 3 for 300 A.

5.2.2 EXPLANATION OF THE ROTATION ANGLE BEHAVIOR

Suppose that the beam distribution passing through the slit is uniform, rotating at angular velocity $\dot{\theta}$, and has divergence described by the usual α parameter as shown in Fig. 51. After the slit, the unit normalized beam distribution can be written as

$$\frac{1}{2x_b}\left[\Theta\left(\frac{x}{x_b}+1\right)-\Theta\left(\frac{x}{x_b}-1\right)\right]\delta(y)\delta\left(v_x+\frac{\alpha x v_z}{\beta}\right)\delta(v_y-\dot{\theta}x), \tag{113}$$

where Θ is the Heavyside function, δ is the Dirac delta function.

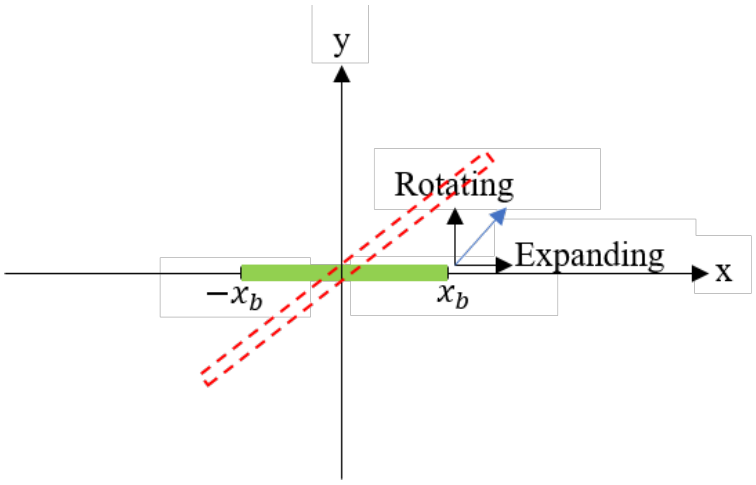

FIG. 51: Schematic diagram of the beam just passing through a slit.

Assuming the field between slit and viewer is negligible, the equations of motion is given by

$$\begin{aligned} x(z) &= zx' + x_0, \\ y(z) &= zy' + y_0, \end{aligned} \tag{114}$$

where z is the distance between the slit and the viewer, x_0 and y_0 are the beam size at the

slit in x and y respectively. Since $y' = \dot{\theta}x_0/v_z$ and $y_0 = 0$,

$$y(z) = \frac{\dot{\theta}x_0 z}{v_z}. \tag{115}$$

And,

$$x_0 = \frac{yv_z}{\dot{\theta}z} = x_b. \tag{116}$$

Therefore,

$$x(z) = x'z + \frac{yv_z}{\dot{\theta}z}. \tag{117}$$

Thus, the beam distribution in configuration space downstream of the slit is consequently

$$\frac{v_z y}{2\dot{\theta}x_b z}\left[\Theta\left(y + \frac{\dot{\theta}x_b z}{v_z}\right) - \Theta\left(y - \frac{\dot{\theta}x_b z}{v_z}\right)\right]\delta\left(x - x'z - \frac{yv_z}{\dot{\theta}z}\right), \tag{118}$$

which extend between the limits of $-\dot{\theta}x_b z/v_z \leq y \leq \dot{\theta}x_b z/v_z$. The x position correlated with the boundary of the line is $x'z + x_b$. Thus, the angle the distribution makes with the x axis is

$$\theta_{rot} = \arctan2\left(\frac{\dot{\theta}zx_0/v_z}{x_0 + x'z}\right). \tag{119}$$

For a diverging beam $x' = x_0/f$ where f is the focal length. Therefore,

$$\theta_{rot} = \arctan2\left(\frac{\dot{\theta}z/v_z}{1 + z/f}\right). \tag{120}$$

According to Eq. 32 $\alpha\epsilon = -\langle xx'\rangle$. And thus, $1/f = -\alpha\epsilon/x_{0,rms}^2$. By substituting into the above equation

$$\theta_{rot} = \arctan2\left(\frac{\dot{\theta}z/v_z}{1 - z\alpha\epsilon/x_{0,rms}^2}\right). \tag{121}$$

Hence, the quadrant in which the rotated beamlet result in depends on angular velocity and beam divergence or convergence. Figures 52, 53 show the α variation at slit 1 and slit 2 respectively. Figures 54, 55 show the angular velocity variation at slit 1 and slit 2 respectively.

At slit 1, α is always negative except from 145 - 156 A, which indicates that the beam is constantly diverging at slit 1 except for 145 - 156 A. Thus, the rotation angle should follow the angular velocity pattern. However, at 145 - 156 A beam is converging, and the angle

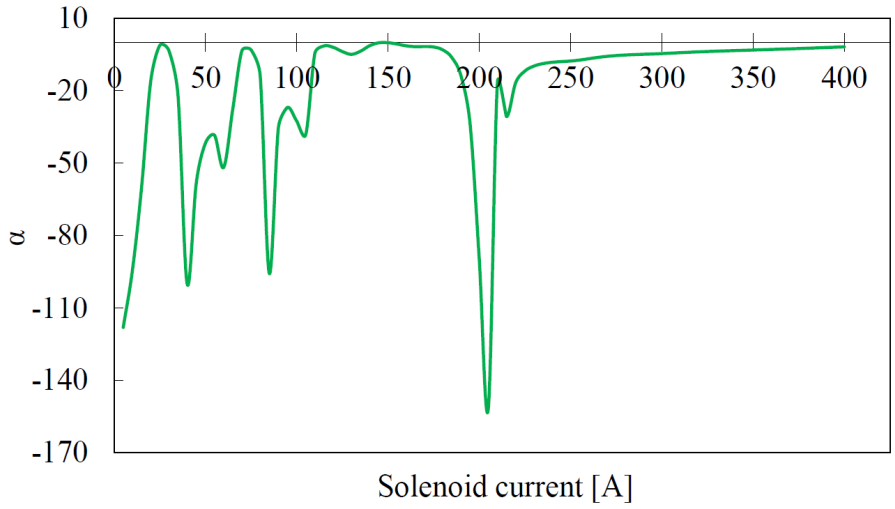

FIG. 52: The α variation at slit 1.

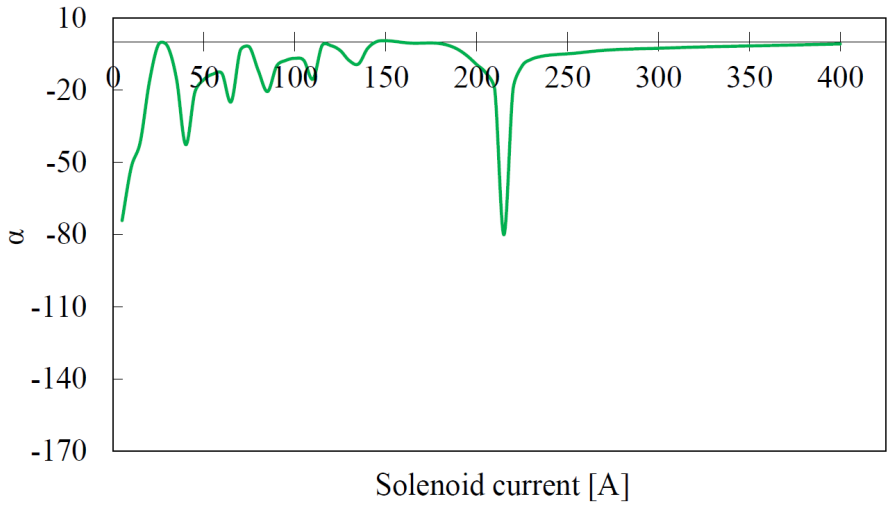

FIG. 53: The α variation at slit 2.

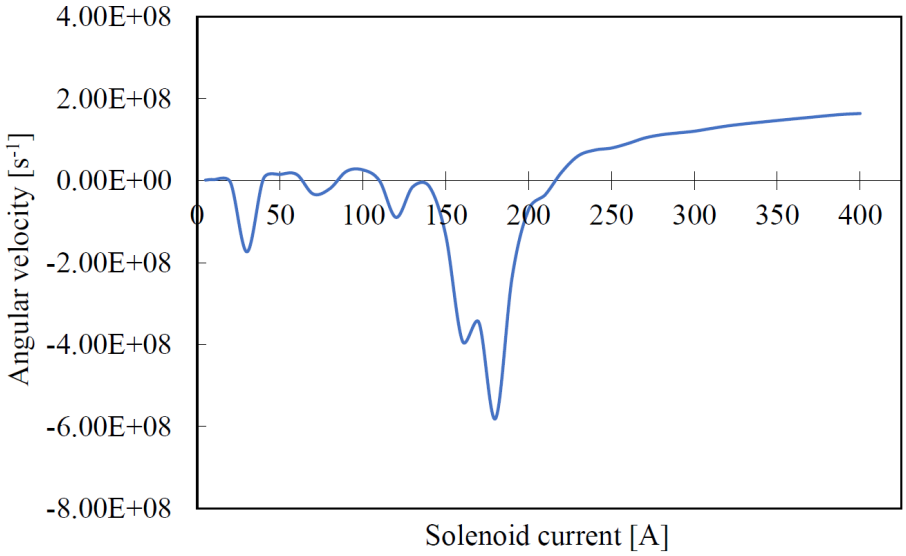

FIG. 54: The angular velocity variation at slit 1.

FIG. 55: The angular velocity variation at slit 2.

is determined by the z a x_0. Hence, at 150 A, the rotation angle can be seen in the 3$^{\text{rd}}$ quadrant, *i.e.*, in slit 1 - viewer 3.

At slit 2, α is always negative, which indicates that the beam is always diverging. Hence, the rotation angle should follow the angular velocity pattern. However, specifically for the solenoid currents larger than 200 A rotation direction has reversed as well as the beam size became very large. This can be explained with conservation of canonical angular momentum Eq. 80.

Consider a beam inside the cathode solenoid where $B_z = B_0$, $\dot{\theta}_0 = 0$ and outside the solenoid where $B_z = B_1$, $\dot{\theta}_1 \neq 0$, $B_1 << B_0$. Beam size inside the solenoid is r_0 and outside the solenoid r_1. From Eq. 80,

$$\frac{q}{2\pi}\psi_0 = \gamma m r^2 \dot{\theta}_1 + \frac{q}{2\pi}\psi_1. \tag{122}$$

For an electron beam this can be re-written as

$$\dot{\theta}_1 = \frac{q}{2\gamma m}\left[B_1 - B_0\left(\frac{r_0}{r_1}\right)^2\right]. \tag{123}$$

According to the above equation, when beam size is large outside the solenoid ($r_1 >> r_0$), $\dot{\theta}_1$ becomes positive and when the beam size is small outside the solenoid ($r_1 << r_0$), $\dot{\theta}_1$ become negative.

5.2.3 ERROR ANALYSIS

In order to obtain the error on the measurements, the error of the linear fit was calculated by using a ROOT macro [45]. In simulations, same as in the beam size measurements, sources that cause errors were identified as 3% for laser profile, 2% for the distance between slit and viewer, and 1% for B_z. Moreover, the laser position on the photocathode was changed by 1 mm, and the photocathode recess length was changed to 6 mm and 1 mm. Finally, the total error was calculated as before.

5.3 CONSERVATION OF CANONICAL ANGULAR MOMENTUM

Conservation of canonical angular momentum, also known as Busch's theorem, states that the canonical angular momentum of a charged particle moving in an axially symmetric magnetic field is conserved. The canonical angular momentum of an electron moving in an

axial magnetic field B_z can be written as

$$L = \gamma m r^2 \dot{\theta} + \frac{1}{2} q B_z r^2, \tag{124}$$

where γ is the Lorentz factor, $\dot{\theta}$ is the angular velocity, m and q are the electron rest mass and charge, respectively. Canonical angular momentum of the electron beam moving in an axial magnetic field can be obtained by averaging Eq. 124 over the beam distribution.

$$\langle L \rangle = \gamma m \langle r^2 \dot{\theta} \rangle + \frac{1}{2} q B_z \langle r^2 \rangle. \tag{125}$$

According to the 2D field map obtained for the cathode solenoid, B_r at the photocathode cannot be neglected. Thus, at the photocathode $\dot{\theta_0} \neq 0$, $B_z = B_0$ and $r = r_0$ yields

$$\langle L \rangle = \gamma m \langle r_0^2 \dot{\theta_0} \rangle + \frac{1}{2} q B_0 \langle r_0^2 \rangle. \tag{126}$$

At a location outside the solenoid, $\dot{\theta_1} \neq 0$ $B_z = B_1$ and $r = r_1$ yields

$$\langle L \rangle = \gamma m \langle r_1^2 \dot{\theta_1} \rangle + \frac{1}{2} q B_1 \langle r_1^2 \rangle. \tag{127}$$

According to the conservation of canonical angular momentum

$$\gamma m \langle r_0^2 \dot{\theta_0} \rangle + \frac{1}{2} q B_0 \langle r_0^2 \rangle = \gamma m \langle r_1^2 \dot{\theta_1} \rangle + \frac{1}{2} q B_1 \langle r_1^2 \rangle. \tag{128}$$

In order to verify the theory, GPT simulations were conducted with the similar beam parameters used in beam size simulations and rotation angle simulations using weighted laser profile. GPT simulation data provides x, y, γ, β_x, β_y, and B_z of each particle at the photocathode and at viewer locations. The calculations were done by making the beam centered and considering the angular momentum relative to the center of the beam ($X_i = x_i - \text{mean}(x_i)$, $Y_i = y_i - \text{mean}(y_i)$, $\beta_{Xi} = \beta_{xi} - \text{mean}(\beta_{xi})$, and $\beta_{Yi} = \beta_{yi} - \text{mean}(\beta_{yi})$) where i represent each particle, and using $\langle r_0^2 \dot{\theta_0} \rangle = c \langle X \beta_Y - Y \beta_X \rangle$. Figures 56, 57 show the above calculation for cathode solenoid currents 10 A to 200 A.

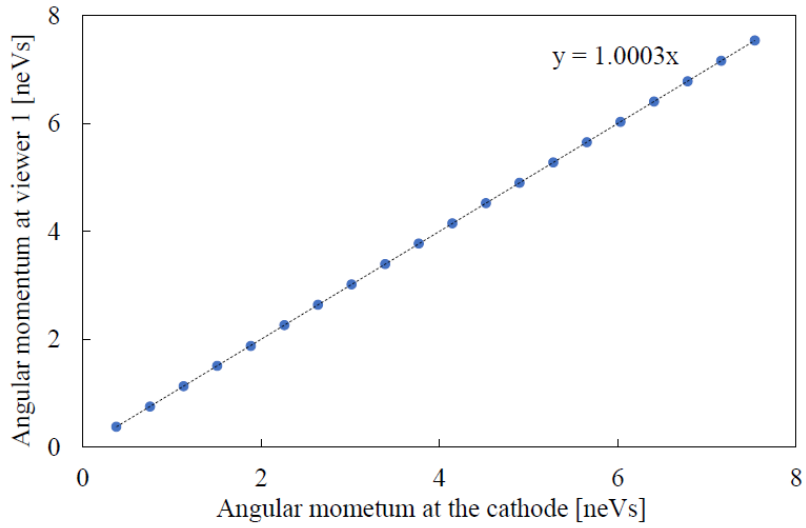

FIG. 56: Canonical angular momentum at viewer 1 verses canonical angular momentum at the photocathode and the linear fit.

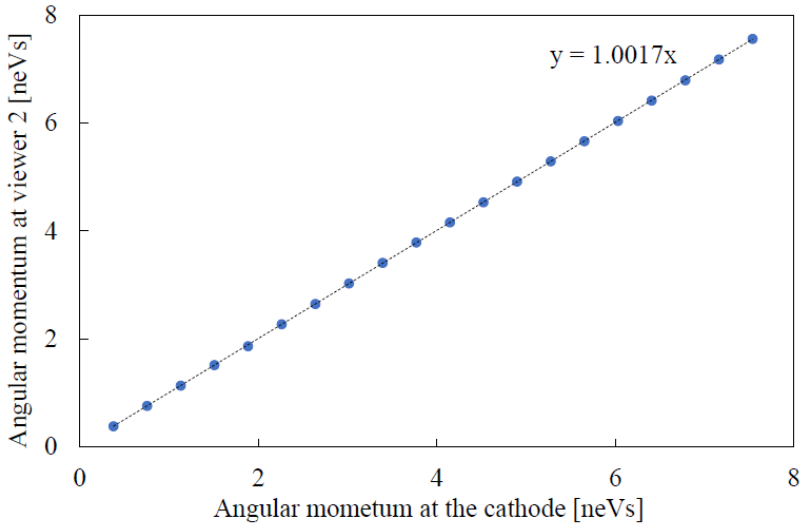

FIG. 57: Canonical angular momentum at viewer 2 verses canonical angular momentum at the photocathode and the linear fit.

According to the above plots, GPT results agree with the theory as long as there is no beam loss along the beamline; thus, all the particles are inside the magnetic field map region, generated up to the beam pipe radius. However, for higher cathode solenoid currents (200 A to 400 A) beam gets larger at viewer 2 and viewer 3 (Fig. 39, Fig. 40) and also goes off-axis at the end of the beamline. As a result, simulations could only verify the theory at lower cathode solenoid currents and only at viewers 1 and 2.

5.4 DRIFT EMITTANCE VARIATION WITH THE CATHODE MAGNETIC FIELD

Emittance was measured using a single solenoid scan technique. Before taking the measurements the beam was centered throughout the beamline using the three viewers, the Faraday cup, and the beam dump as explained below. The center of the three viewers were aligned with the center of the beam pipe. Therefore, the beam was centered at each viewer by using the upstream steering magnets. At the same time, the current readback from the Faraday cup and beam dump were checked to make sure that they read the same, thus no beam loss took place. The beam needs to be centered at all the upstream focusing solenoids before the viewer. If the beam is centered at a focusing solenoid, changing its strength would only change the size of the beam on a downstream viewer, not its position. Thus the "dithering" option was used and centered the beam on each focusing solenoid using the upstream steering magnets. These steps have to be repeated a few times to get the best beam transportation. Once the beam propagates well to the dump, the beamline vacuum should be stable.

Also, these settings could change easily after a run, after cycling a magnet as some magnets are mismatched, after a photocathode swap as it will not be at the same position as before or not placed precisely perpendicular to the beamline. Thus, one has to follow the above steps and make the beam centered every time.

As mentioned in the previous chapter, emittance associated with the magnetized beam mainly depends on the beam size at the cathode and the magnetic field at the cathode. Therefore, four different laser sizes were used, and the emittance measurements were repeated by varying the cathode solenoid current from 0 - 400 A (0 - 0.15 T). Figure 58 shows the Spiricon images of the four different laser sizes used.

Once the laser is set, and the beam is centered, the first two focusing solenoids were used to make the beam smaller and round on the third viewer. The third focusing solenoid was used as the scanning solenoid and measured the beam size on the 3rd viewer. In order to find

the scanning range, one can slowly increase the scanning solenoid strength until the beam reaches its waist, which is the middle point of the scanning range. Then five or six steps with step size 0.05 A to each side from the middle point would give you a good range. Once the range is found, one can proceed with the scanning.

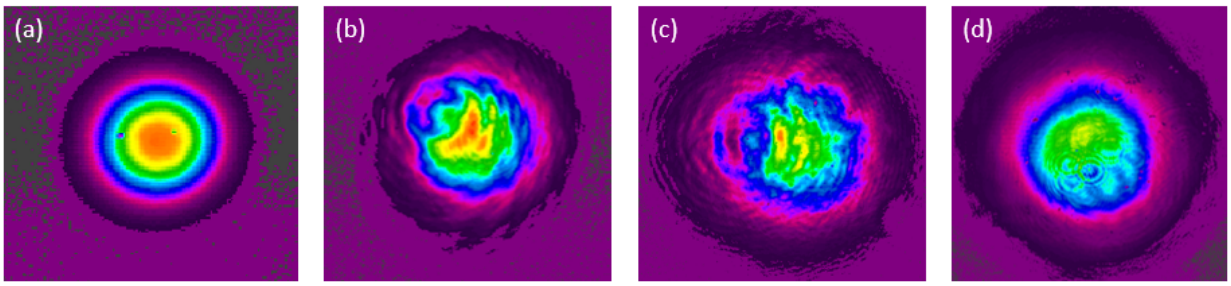

FIG. 58: Different laser spot sizes used.

Figure 59 shows the EPICS screen of the magnetized beam on viewer 3 at its smallest size with the scanning solenoid current and σ_x and σ_y.

For laser 1 in Fig. 58 (a), the gun was biased at 300 kV and delivered less than 2 nA to the dump. Thus, the space charge effect was negligible. The scan was done for 0, 50, 100, 150, ..., 400 A cathode solenoid currents. The photocathode used was 90 minute Sb GaAs with 0.37% QE. Fig. 60 shows beam size variation on viewer 3 along with the solenoid scan for laser 1.

For laser 2 in Fig. 58 (b), the gun was at 200 kV and delivered less than 2 nA to the dump. The scan was done for 0, 25, 60, 95, 120, 150, 200, 250, ..., 400 A cathode solenoid currents. The photocathode used was 10 minute Sb on Mo with 0.26% QE.

For laser 3 in Fig. 58 (c), the gun was at 200 kV and delivered less than 2 nA to the dump. The scan was done for 0, 25, 60, 95, 150, 200, 250 A cathode solenoid currents. Here, the low gun voltage and larger beam size prevented us from going up to 400 A. The photocathode used was 10 minute Sb on Mo with 0.26% QE. Hence, the emittance measurements were repeated for a larger laser size with higher voltage as laser 4 in Fig. 58 (d). The gun was at

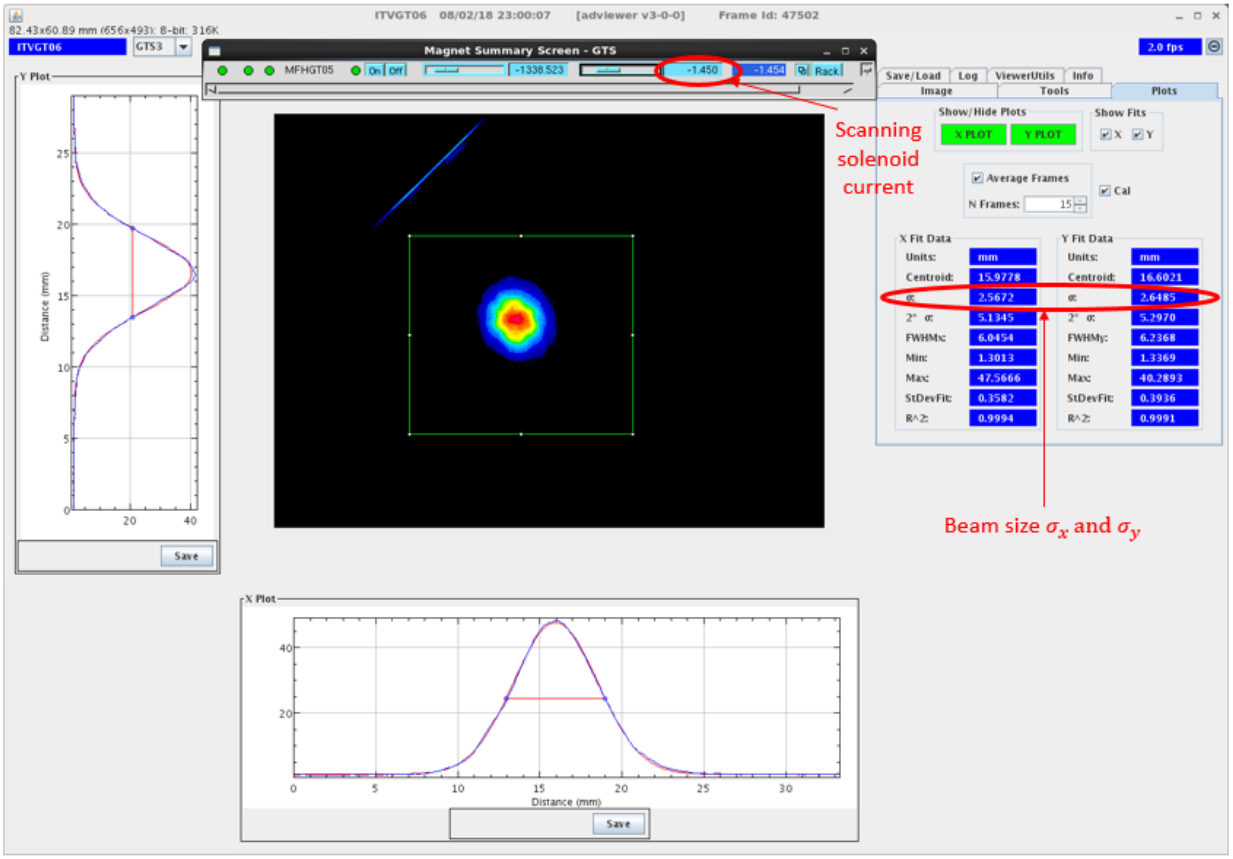

FIG. 59: Magnetized beam on viewer 3 at its smallest size in the scan. First two solenoids are on.

300 kV, delivering less than 2 nA to the dump. The scan was done for 0, 50, 100, 150, 200, 300, 400 A gun solenoid currents. The photocathode used was 10 minute Sb on Mo with 0.26% QE.

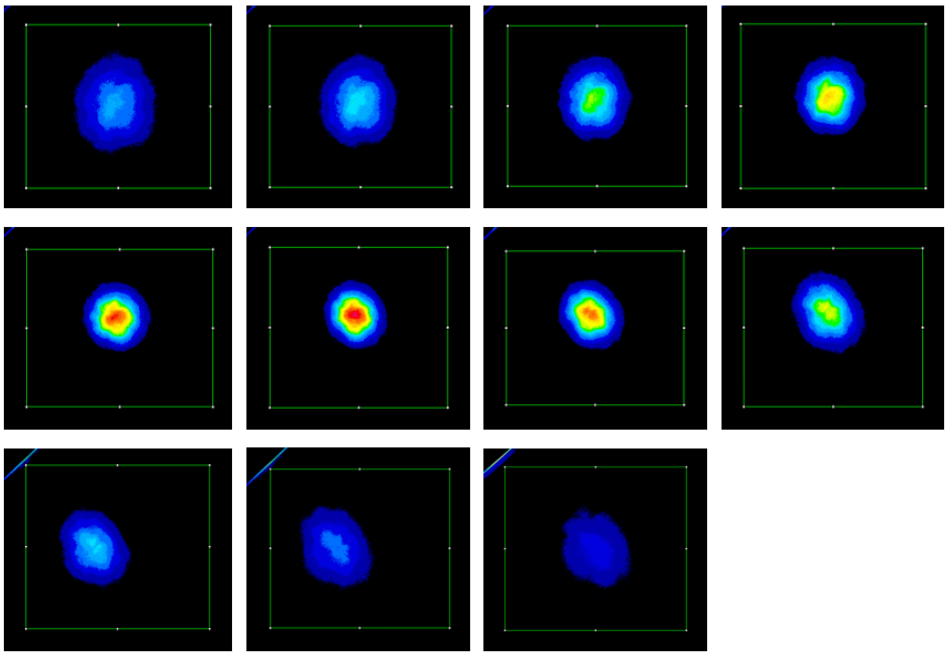

FIG. 60: Beam size variation on viewer 3 along the solenoid scan (laser 1, gun solenoid current 300 A).

To obtain the emittance, the scanning solenoid current (I), corresponding beam size σ_x and σ_y on the viewer and error in each beam size dx and dx (the fluctuation range of σ_x and σ_y of each scan) were used. By feeding the above data table into the ROOT program along with corresponding voltage, laser size, the distance between scanning solenoid and the viewer, the plots of σ_x vs. I^2, σ_y vs. I^2 and σ_x^2 vs. I^2, σ_y^2 vs. I^2 were obtained with a parabolic fit to them as shown in Fig. 61. The quality of the scan can be checked by how well the points are aligned with the fit. These plots provide the normalized beam emittance, the thermal angle, α, β, and γ in the x and y planes at the location of the scanning solenoid.

Since the beam is not perfectly circular for most of the cases, the geometric mean of the x and y normalized emittances ($\sqrt{\epsilon_x \epsilon_y}$) was used to obtain the final drift emittance.

GPT was used to model the beamline and compared with the measurements [44]. The 3D electric field map of the photo-gun and the 2D magnetic field map of the gun solenoid were used in the simulations. Similarly, the GPT "GDFMGO" program optimized the steering magnets to make the beam on-axis throughout the beamline.

The magnetic field map plays a critical role in GPT simulations. How far it extends in the z-direction, how far it extends radially, the step size, whether it abruptly ends, whether it is a 1D, 2D, or 3D field map are the most critical aspects. Since cathode solenoid generates a very high magnetic field, its tails extend to a very long distance. Nevertheless, when the magnetic field map extends only up to few meters (2 - 3 m) and ends abruptly with 4×10^{-4} T, that affects the accuracy of the emittance simulations. Therefore, it is essential to have an extended field map that ends smoothly. Also, when the beam gets large and off-axis, it sees more off-axis fields and sometimes falls out of the field map. Therefore it is essential to have a radial field that at least covers the beam pipe. 1D field map does not accurately represent the situations as GPT extrapolates it to a cylindrical symmetric field map. Thus, fields near the z-axis can only be correctly simulated.

In order to make the beam smaller throughout the beamline and match the measurement conditions, the first two focusing solenoids where used in the simulations with their field maps with almost the same settings. Further, the following beam parameters were used: MTE 0.130 eV, Gaussian temporal profile 21.24 ps (rms), and cathode placed at 0 m with all beam pipe radius. No space charge effects were applied since the beam current is minimal.

Similarly as before, the weighted laser profiles were generated for each laser QE combination and used as the initial distribution. Fig. 62 shows the laser and QE profiles corresponding to each measurement and Figs. 63, 64, 65, and 66 show the input image with its initial GPT particle distribution and its x and y Gaussian fit.

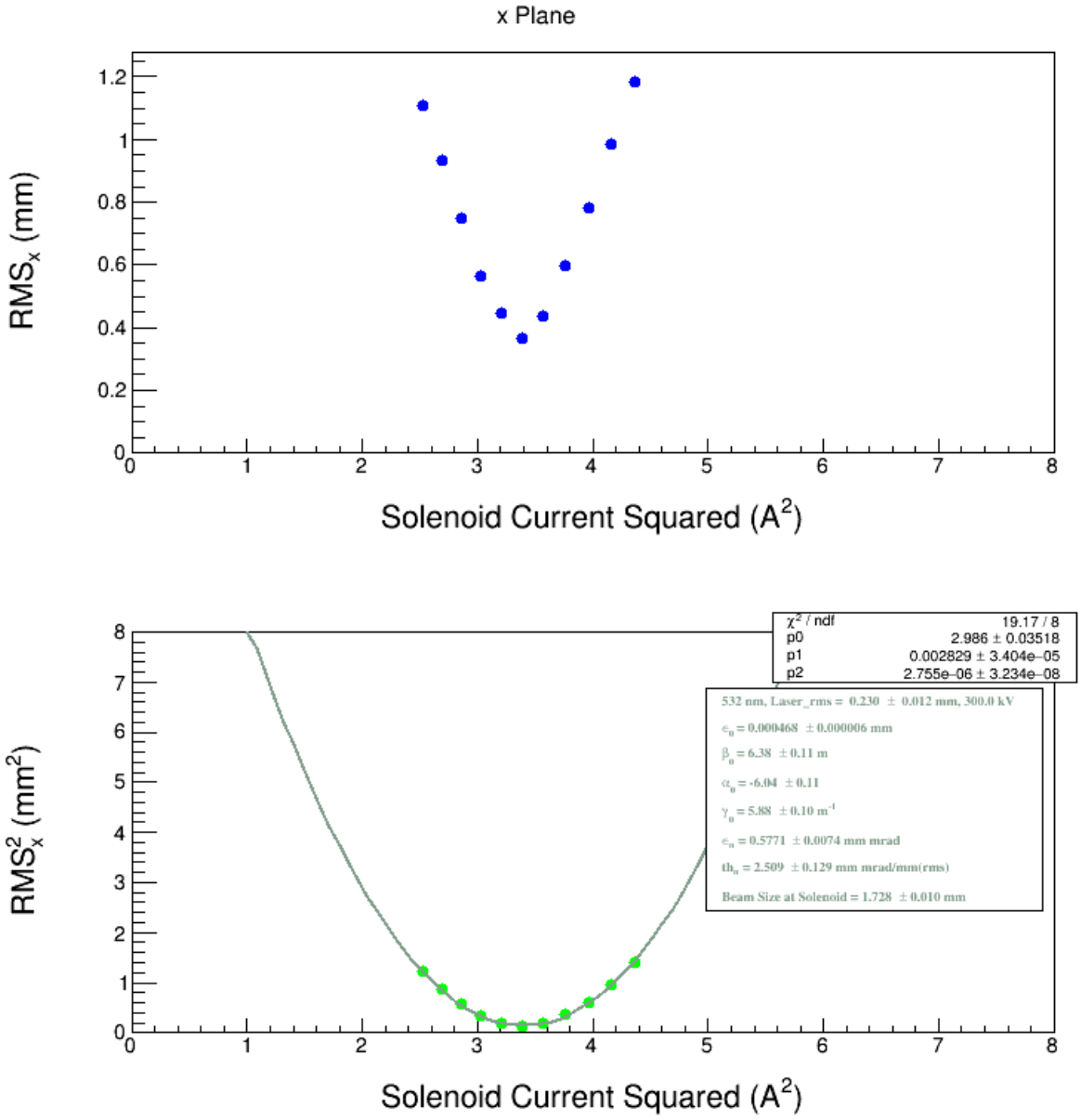

FIG. 61: σ_x vs I^2 and σ_x^2 vs I^2 with the fit.

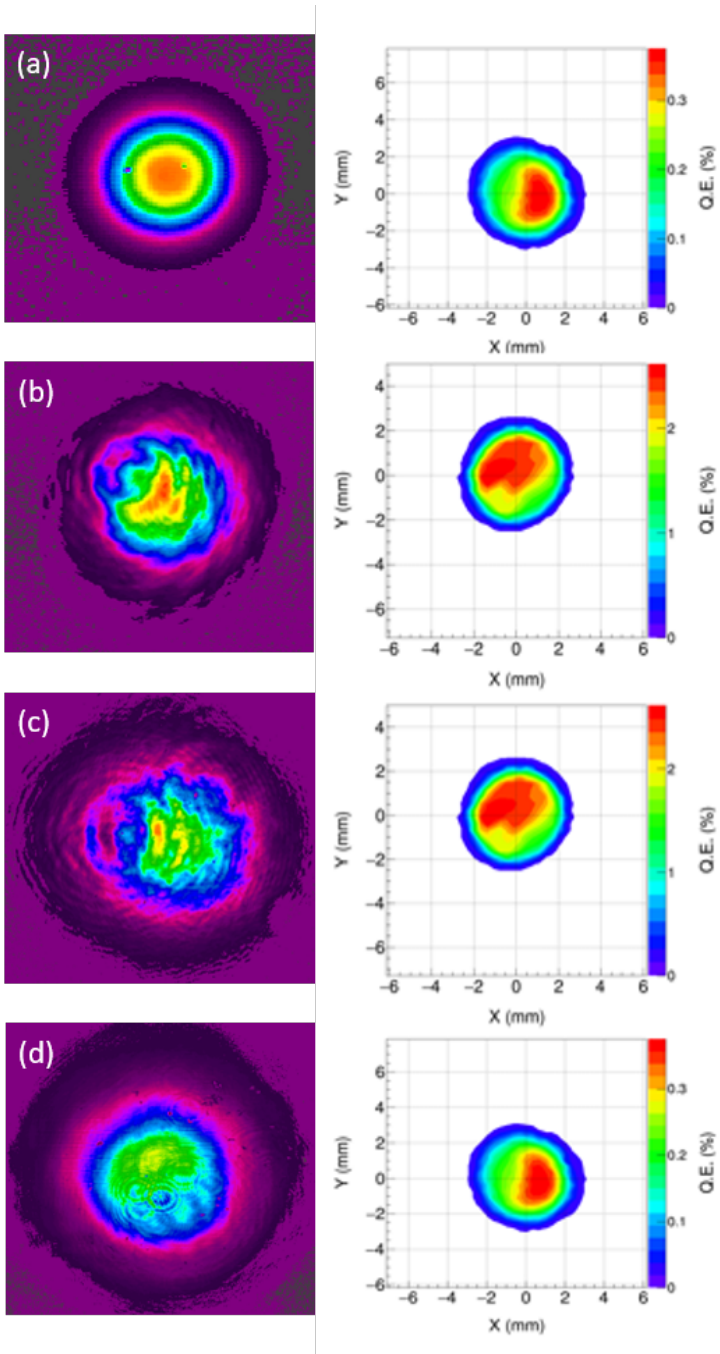

FIG. 62: (a) Laser 1 and QE of 90 minute Sb on GaAs, (b) Laser 2 and QE of 10 minute Sb on Mo, (c) Laser 3 and QE of 10 minute Sb on Mo, and (d) Laser 4 and QE of 90 minute Sb on GaAs.

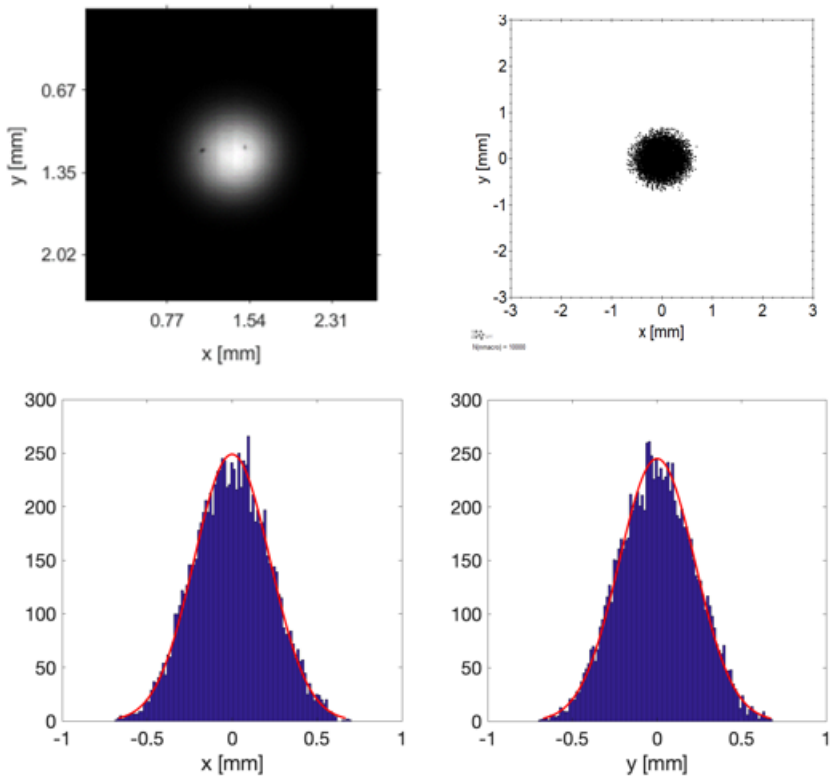

FIG. 63: For laser 1, GPT input gray-scale image (top left), initial particle distribution from the image (top right), x distribution (bottom left) and y distribution (bottom right) at the cathode with the Gaussian fit.

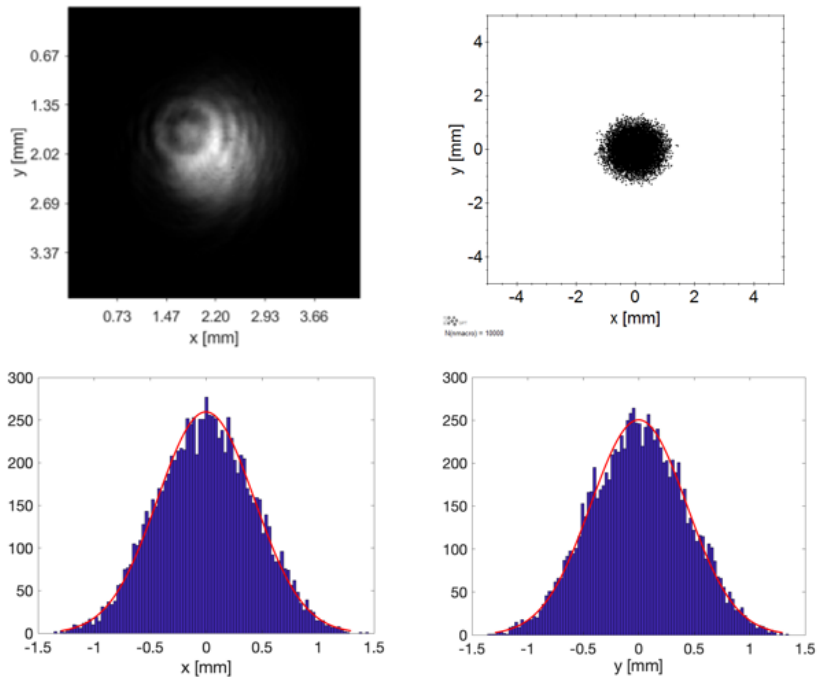

FIG. 64: For laser 2, GPT input gray-scale image (top left), initial particle distribution from the image (top right), x distribution (bottom left) and y distribution (bottom right) at the cathode with the Gaussian fit.

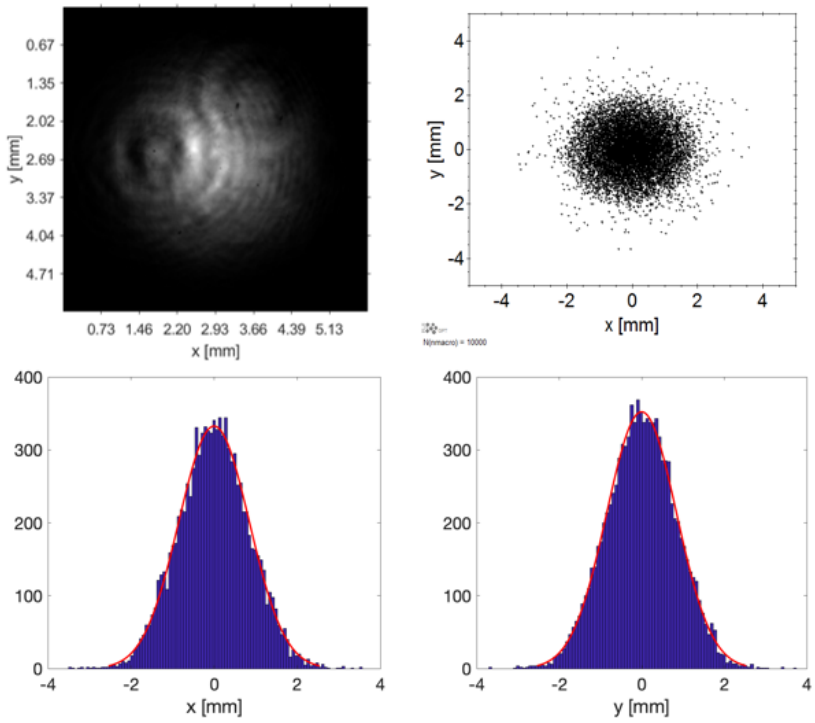

FIG. 65: For laser 3, GPT input gray-scale image (top left), initial particle distribution from the image (top right), x distribution (bottom left) and y distribution (bottom right) at the cathode with the Gaussian fit.

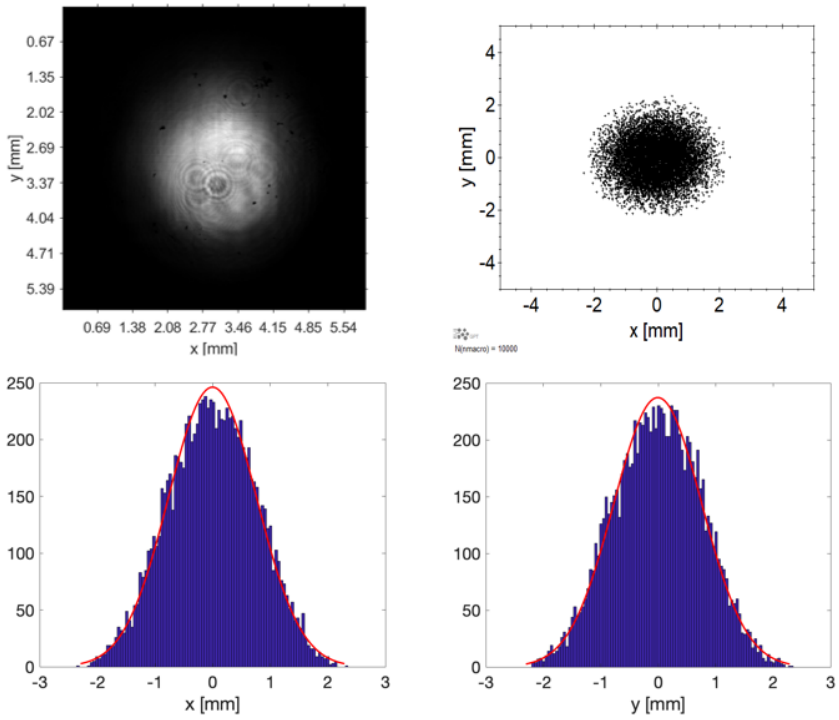

FIG. 66: For laser 4, GPT input gray-scale image (top left), initial particle distribution from the image (top right), x distribution (bottom left) and y distribution (bottom right) at the cathode with the Gaussian fit.

TABLE 3: Beam sizes at the cathode for each laser size obtained from the Gaussian fit.

Laser No	Beam size on the cathode	
	σ_x [mm]	σ_y [mm]
Laser 1	0.2228	0.2245
Laser 2	0.4317	0.4316
Laser 3	0.8477	0.8447
Laser 4	0.7631	0.7649

Table 3 shows the laser *rms* values obtained from each Gaussian fit. GPT inbuilt rms emittance routines, "nemixrms" and "nemiyrms" were used to obtain the total transverse emittance along the beamline. Further, "cnemixrms" and "nemirrms" were used to obtain the correlated emittance and uncorrelated emittance, respectively. The uncorrelated emittance is calculated by removing the $r - p_\phi$ coupling due to the solenoid field from the normalized emittance. Figure 67 shows the evolution of the drift, correlated and uncorrelated emittance for laser 2 when the cathode solenoid is at 250 A.

The drift emittance plot shows huge emittance variation from 0 - 2 m which is the region of the cathode solenoid field and 1st two focusing solenoid fields. This is an artifact of the numerical method used to calculate the emittance. When the solenoid field vanishes, emittance decreases and returns to a constant value, as shown from 2 - 4 m. When all the correlations are removed, emittance should be small and constant throughout the beamline. However, there is a slight bump between 0.5 - 1.2 m due to the region's distorted magnetic field. As predicted by theory, correlated emittance is more prominent than uncorrelated emittance.

Figure 68 illustrates the comparison between measurements and GPT simulations for all four laser sizes. Figure 69 shows how drift emittance varies with the beam size at the cathode for 150 A and 300 A cathode solenoid currents.

According to the plot, there is a clear linear dependence of the drift emittance on the applied cathode magnetic field, consistent with the equation. In addition, there is good agreement between measurements and simulations. We observed significant beam loss at

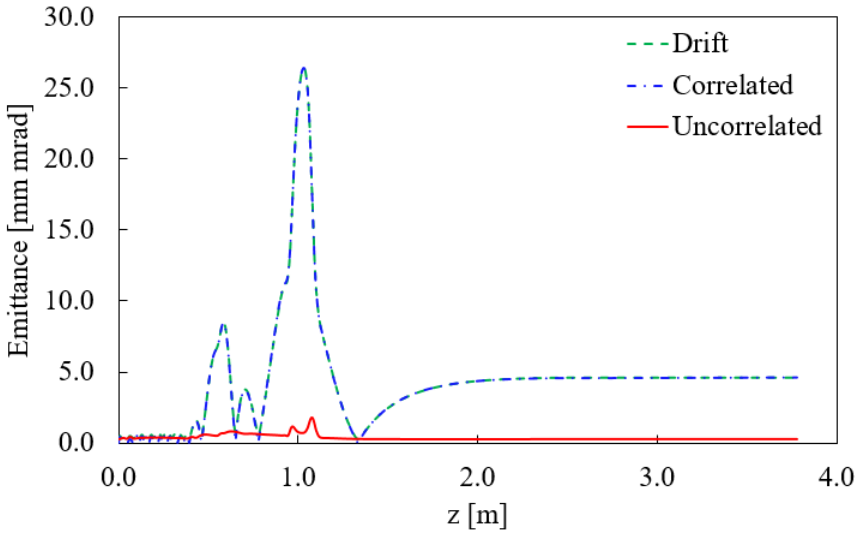

FIG. 67: The evolution of drift *rms* emittance (blue), correlated *rms* emittance (green dashed), and uncorrelated *rms* emittance (red) for laser 2 when the cathode solenoid is at 250 A.

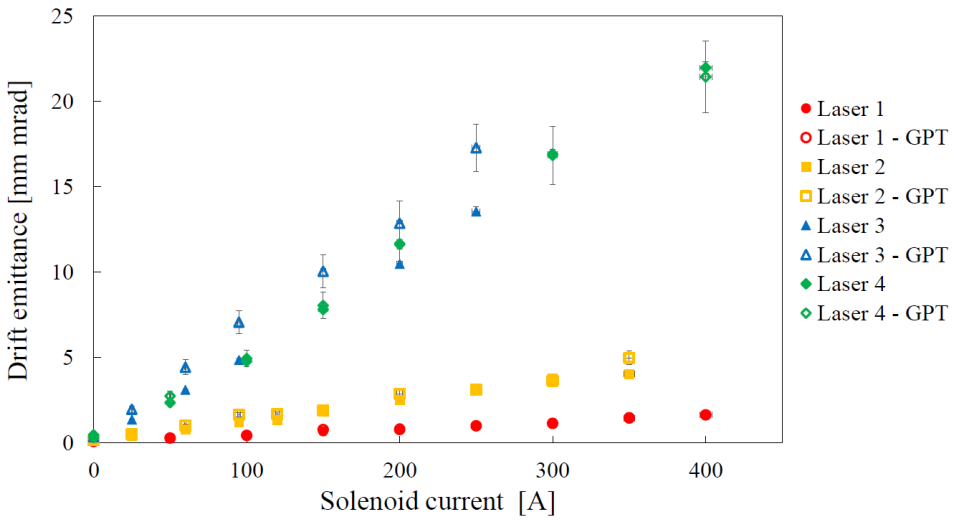

FIG. 68: Drift emittance measurements and corresponding GPT simulations for Laser 1 at 300 kV, Laser 2 at 200 kV, Laser 3 at 200 kV, and Laser 4 at 300 kV.

higher magnetic field strengths, as the beam size is large and beam energy is small. This caused difficulty in measuring the beam sizes accurately.

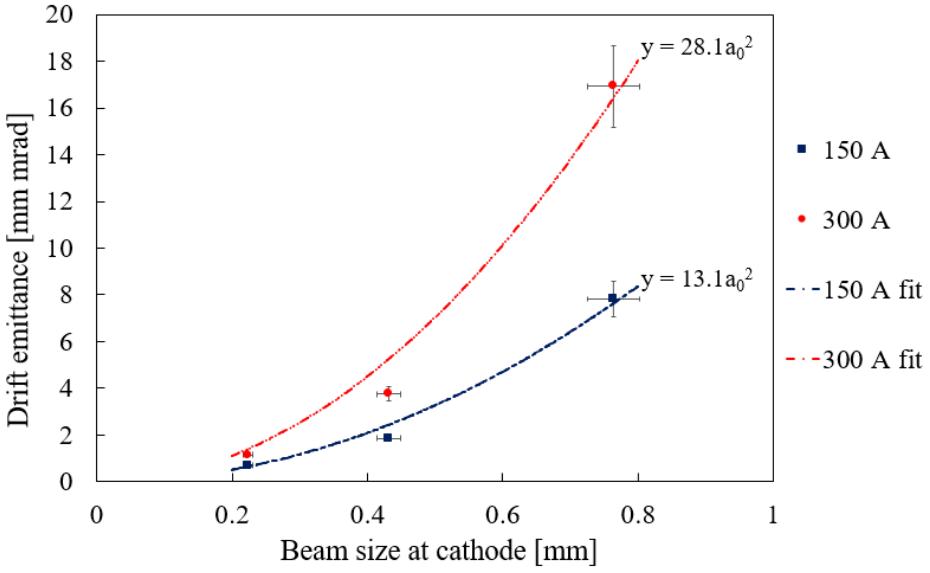

FIG. 69: Drift emittance variation with the beam size at the cathode for 150 A and 300 A.

5.4.1 ERROR ANALYSIS

The systematic error analysis was conducted as before, by identifying the possible sources which could cause the errors and assigning a error percentage for each with our past experience with those sources. For each source the resultant error of emittance were calculated using

$$\frac{\Delta\varepsilon}{\varepsilon} = \frac{|\varepsilon_1 - \varepsilon_2|}{\left(\frac{\varepsilon_1 + \varepsilon_2}{2}\right)}, \tag{129}$$

where, ε_1 and ε_2 represent the emittance values with and without the error, respectively. Thus, the total error can be calculated by

$$\left(\frac{\Delta\varepsilon}{\varepsilon}\right)_{\text{total}} = \sqrt{\left(\frac{\Delta\varepsilon_1}{\varepsilon_1}\right)^2 + \left(\frac{\Delta\varepsilon_2}{\varepsilon_2}\right)^2 + \left(\frac{\Delta\varepsilon_3}{\varepsilon_3}\right)^2 + \dots} \,. \tag{130}$$

Table 4 shows the sources that could cause the errors, their possible errors, calculated individual errors (from the + error value), and the total error for a few different laser spot sizes and magnetizations. According to those calculations, an average error was calculated on each source, see Table 5. In addition, the observed maximum and minimum beam size fluctuates on the EPICS screen was used as the error of beam size reading on the viewer. Further, 1% error was assumed for the magnetic field at the cathode.

Similarly, a systematic error analysis was conducted on GPT simulations. Tables 6, 7, 8, and 9 show the error calculations for all four laser sizes.

TABLE 4: Systematic error analysis on the measurements.

Source of error	Error	Laser 1 300 A [%]	Laser 2 0 A [%]	Laser 2 300 A [%]	Laser 3 250 A [%]	Laser 4 300 A [%]
Scanning solenoid current [mA]	± 5	0.4	0.5	0.3	0.4	0.3
Gun HV [kV]	± 1	0.6	0.8	0.8	0.8	0.6
Distance between solenoid and viewer [mm]	± 5	0.7	0.7	0.7	0.7	0.7
Scanning solenoid field map at 1 Amp [G]	± 0.5	0.7	0.7	0.7	0.7	0.7
Scanning solenoid effective length [mm]	± 0.5	0.7	0.7	0.7	0.7	0.7
Beam size stability on the viewer [mm]		0.5	1.1	0.2	1.3	0.6
Total		1.5	1.9	1.5	2.0	1.6

TABLE 5: Summary of systematic error analysis on the measurements.

Source of error	Average error [%]
Scanning solenoid current [mA]	0.4
Gun HV [kV]	0.7
Distance between solenoid and viewer [mm]	0.7
Scanning solenoid field map at 1 Amp [G]	0.7
Scanning solenoid effective length [mm]	0.7
Total	1.5

TABLE 6: Systematic error analysis on the simulations for the laser 1.

Cathode solenoid current [A]	Source of error			Total error [%]
	Beam size at the cathode (3% error) [%]	MTE (10% error) [%]	Cathode solenoid field map (1% error) [%]	
0	3.0	4.6	0.0	5.5
50	5.7	0.4	1.0	5.8
100	5.8	0.2	1.0	5.9
150	5.9	0.1	1.0	6.0
200	5.9	0.0	1.0	6.0
250	5.9	0.0	1.0	6.0
300	5.8	0.0	1.0	6.0
350	5.9	0.0	1.0	6.0
400	5.9	0.0	1.0	6.0

TABLE 7: Systematic error analysis on the simulations for the laser 2.

Cathode solenoid current [A]	Source of error			Total error [%]
	Beam size at the cathode (3% error) [%]	MTE (10% error) [%]	Cathode solenoid field map (1% error) [%]	
0	3.8	4.5	0.0	6.0
25	7.0	0.5	1.0	7.1
60	7.3	0.1	1.0	7.3
95	7.3	0.0	1.0	7.4
120	7.3	0.0	1.0	7.3
150	7.3	0.0	1.0	7.3
200	7.3	0.0	1.0	7.4
250	7.3	0.0	1.0	7.4
300	8.0	0.0	1.0	8.0
350	8.2	0.0	1.0	8.3

TABLE 8: Systematic error analysis on the simulations for the laser 3.

Cathode solenoid current [A]	Source of error			Total error [%]
	Beam size at the cathode (3% error) [%]	MTE (10% error) [%]	Cathode solenoid field map (1% error) [%]	
0	5.5	3.6	0.0	6.6
25	9.7	0.1	1.0	9.7
60	9.8	0.0	1.0	9.9
95	9.7	0.0	1.0	9.8
150	9.8	0.0	1.0	9.8
200	10.0	0.0	1.0	10.0
250	7.9	0.0	1.0	8.0

TABLE 9: Systematic error analysis on the simulations for the laser 4.

Cathode solenoid current [A]	Source of error			Total error [%]
	Beam size at the cathode (3% error) [%]	MTE (10% error) [%]	Cathode solenoid field map (1% error) [%]	
0	5.9	4.3	0.0	7.3
50	9.7	0.0	1.0	9.7
100	9.8	0.0	1.0	9.8
150	9.8	0.0	1.0	9.8
200	9.8	0.0	1.0	9.8
300	10.1	0.0	1.0	10.1
400	9.8	0.0	1.0	9.9

5.5 HIGH CURRENT RUN

Characterization of the magnetized electron beam was concluded by delivering a high current beam to the dump. Delivering a high current magnetized beam poses additional challenges when compared to a non-magnetized beam. The main challenge arises from the significant beam size gain after exiting the cathode solenoid, which causes beam loss and a rise of the vacuum levels. Although the multi-alkali cathodes are very robust, a relatively bad vacuum will still cause degradation of the QE.

Table 10 lists the beam parameters of the magnetized electron beam deliveries. The photocathode QE lifetime is defined as the time it takes for the initial QE to drop to QE/e

$$QE = QE_0 \; e^{-C/C_0}, \tag{131}$$

where e is the Euler's number, C is the charge, and C_0 is the lifetime. The first run on the table 11 (*) was delivered from a photocathode grown on GaAs substrate with 10 minute Sb deposition, and all the other runs were delivered from a photocathode grown on Mo substrate with 10 minute Sb deposition.

TABLE 10: Beam parameters for high current run.

Electron beam current [mA]	Gun HV [kV]	Cathode solenoid current [A]	Magnetic field at photocathode [G]	Laser spot size (rms) [mm]	Laser repetition rate [MHz]	Laser pulse width FWHM [ps]	Bunch charge [pC]
4.5	300	400	1514	0.4	dc	-	-
4.5	200	200	757	0.9	374.25	50	12
14	200	0	0	0.9	303.30	60	46
14	200	200	757	0.9	303.30	60	46
20	100	150	568	0.9	303.30	60	66
28	100	150	568	1.4	374.25	50	75

TABLE 11: Lifetime measurements.

Electron Beam current [mA]	Run time [hour]	Charge extracted [C]	Charge lifetime [C]
4.5	6	100	164*
4.5	38	620	No QE decay
14	16	880	No QE decay
14	92	4500	No QE decay
20	22	1440	No QE decay
28	57	5200	9400

Two high-voltage power supplies were used to energize the photo-gun: A 500 kV, 5 mA Cockcroft-Walton SF_6 gas-insulated high-voltage power supply and a Spellman high-voltage power supply capable of 225 kV and 30 mA with a power limit of 3 kW. The highest beam current produced was 28 mA with a cumulative extracted charge of 5200 C and an estimated $1/e$ charge lifetime of 9400 C. For this run, a 1.4 mm (rms) laser spot was used with a 50 ps (FWHM) pulse width and 374.25 MHz repetition rate. The cathode magnetic field was set at 568 G. The bunch charge of the beam was 75 pC.

The photocathode grown on Mo showed the most extended operational lifetime even with a short Sb deposition time over the same photocathode grown on GaAs wafer substrate. The QE evolution while delivering the three highest beam current runs is shown in Fig. 70. Decay in the QE was only observed for the highest current run at 28 mA.

According to the previous work, ionized residual gasses striking the photocathode (ion back bombardment), and chemical desorption due to heating caused by the high laser power needed to deliver high beam currents, identified to be the dominant mechanisms for QE decay [22]. The desorbed atoms can further get ionized by the emitted electrons and generate ions that can continue the ion back bombardment. The superior beam operational lifetime achieved from the sample prepared on the Mo substrate, which has high thermal conductivity, supports the theory that minimizing heating is essential for continuous delivery of high beam currents from an alkali antimonide photocathode.

Figure 71 shows the delivered beam current versus time for the three highest current runs. The trend down in photocurrent after 24 hours is likely due to photocathode heating and associated bandgap shift, chemical changes (such as dissociation), which indicates the need for photocathode cooling for higher average current delivery. Another possibility is an enhanced ion bombardment due to worsening vacuum due to beam halo at this very high current.

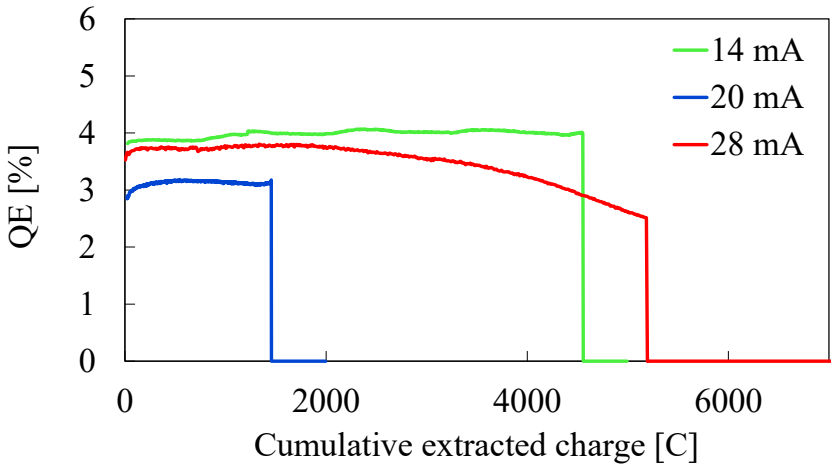

FIG. 70: QE vs. cumulative extracted charge.

As described in [18], uninterrupted high current beam delivery from the photo-gun was only possible when a positive bias voltage (+1000 VDC) was applied to the anode electrode.

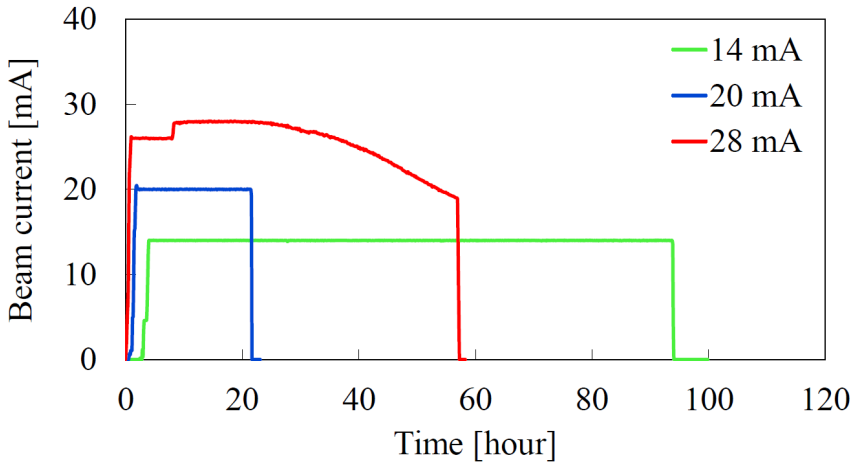

FIG. 71: Beam current variation with the time.

CHAPTER 6

CHARACTERIZATION OF THE SPACE CHARGE DOMINATED MAGNETIZED ELECTRON BEAM

6.1 AS A FUNCTION OF CATHODE MAGNETIC FIELD

The space charge effect of the magnetized electron beam was first characterized as a function cathode magnetic field. Measurements were taken by increasing the laser power at the cathode while keeping the other parameters constant and reading the average current at the dump for different cathode solenoid currents 0, 100, and 200 A. Before the experiment, the focusing solenoids and steering magnets were used to make the beam centered and transport the maximum beam possible to the dump. For a fixed QE value relation between laser power and average current is given by Eq. 2. By using $I_{\text{avg}} = Q_{\text{extracted}} f$ initial bunch charge and extracted bunch charge can be determined.

As mentioned in the second chapter, the Spellman power supply was used to energize the photo-gun with 225 kV biased voltage. The laser was set to 50 kHz and 75 ps (FWHM). Laser power was increased in small steps from 0 to a maximum of 30 mW. Figure 72 shows the laser spot at its maximum laser power.

Figure 73 shows the delivered charge and apparent QE as a function of laser pulse energy for different cathode solenoid currents. For each cathode solenoid current, QE falls rapidly with increasing laser power, implying that the space charge limitations were reached immediately. Measurements were taken in the order of 200 A, 100 A, and 0 A cathode solenoid currents. QE dropped from 6.3 to 4.7 after 200 A measurements due to bad vacuum and hence the ion back bombardment and as a result of heating and hence the chemical desorption. In order to reduce the ion back bombardment and protect the photocathode, the anode was biased with 1000 V after 100 A measurements.

Furthermore, the space charge limit was reached at 0.3 nC and increased for a maximum extracted charge of 0.7 nC. However, the charge beyond 0.3 nC is likely to originate from the edge of the Gaussian laser profile. Also, the oscillatory behavior seen at higher pulse energies likely stems from beam loss. The limited beamline aperture and insufficient strength of the

focusing solenoids prevented clean transportation of the beam to the dump. Moreover, up to 100 nJ, magnetization has a significant effect on the space charge limitations. Higher magnetization extracted more charge by mitigating the space charge effect [46].

FIG. 72: Laser spot at maximum laser power.

Figure 74 shows the EPICS screens of the (a) 0 A , (b) 100 A, and (c) 200 A at maximum current, ion pumps readings, and downstream (ds) and upstream (us) ion collector readings. According to Fig. 74 beam loss occurred throughout the beamline. Further, the ds ion collector reading for 0 A case is larger than 100 A and 200 A, implying that beam loss is larger for non-magnetized beam than the magnetized beam.

Simulations were performed using GPT software. The "GDFMGO" solver program was used for corrector optimization to maximize the charge extraction and make the beam centered. The beamline solenoids were used with their field maps and beam pipe radii throughout the beamline were also included. Other beam parameters were set as same as in the

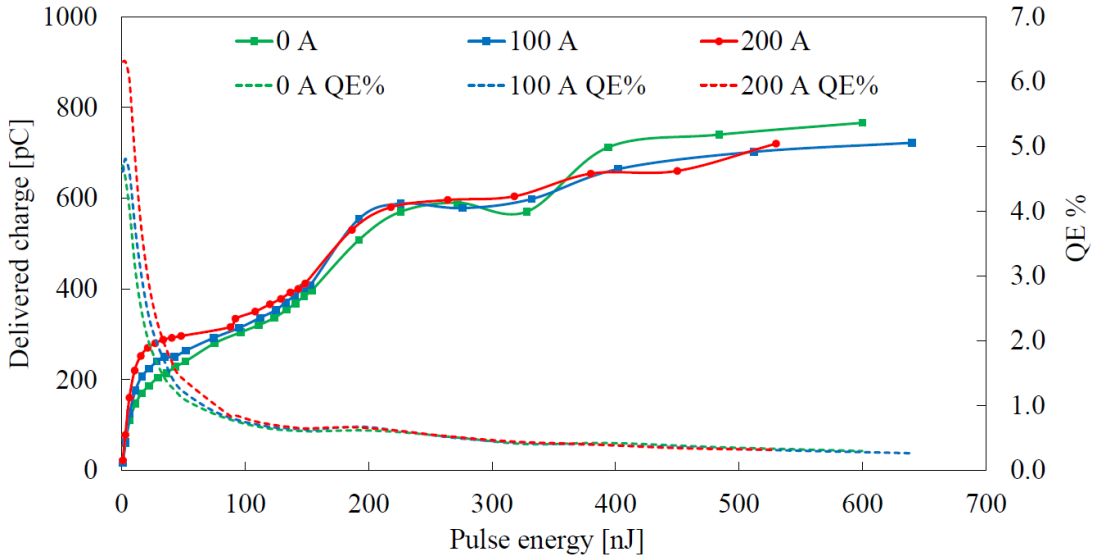

FIG. 73: Delivered charge at the dump vs laser pulse energy and corresponding QE for 0 A, 100 A, and 200 A solenoid currents.

(a) (b) (c)

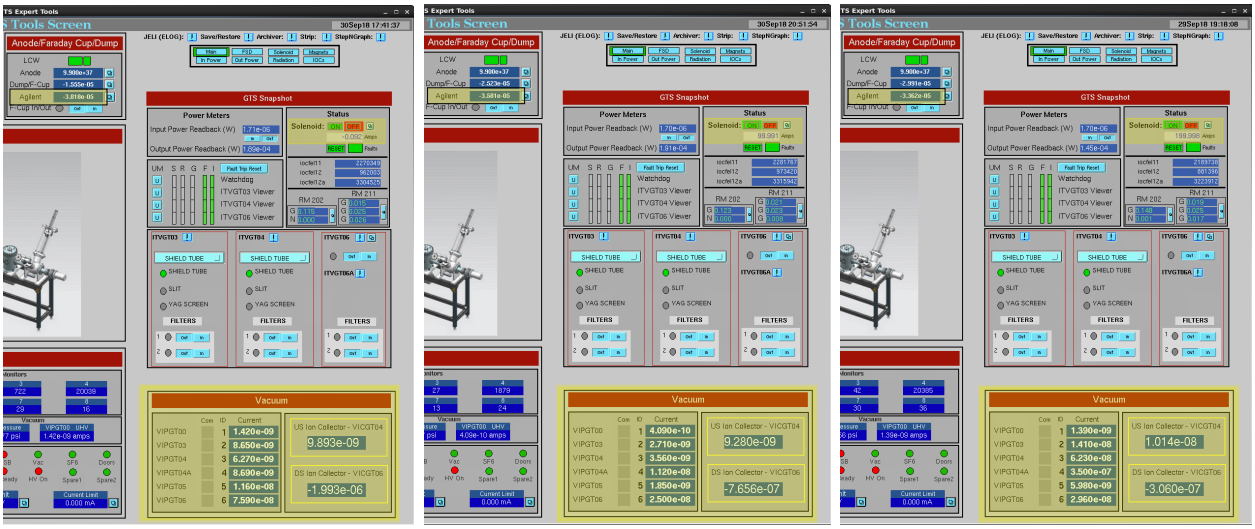

FIG. 74: EPICS screens indicating the cathode solenoid field, average current at the dump and vacuum levels for the maximum laser power for (a) 0 A, (b) 100 A, and (c) 200 A cathode solenoid currents.

measurements. However, instead of laser power, bunch charges calculate from each laser power using Eq. 2 and $I_{\text{avg}} = Q_{\text{extracted}} f$ were used as the independent variable and tracked the delivered charge at the dump. Further, as before, a gray-scale bitmap image of the weighted laser profile was implemented as the initial particle distribution since all the laser spots were not proper Gaussian.

Figure 75 shows the (a) laser profile, (b) QE profile, (c) GPT input gray-scale image, (d) initial particle distribution from the image, (e) x distribution at the cathode with the Gaussian fit, and (f) y distribution at the cathode with the Gaussian fit. According to the Gaussian fit, the laser rms size was 1.2559 mm in x and 1.2167 mm in y.

Figure 76 illustrates the delivered charge at the dump as a function of the initial bunch charge (calculated from incident laser pulse energy and QE) and the corresponding GPT simulations for different cathode solenoid currents. GPT simulations show some agreement at 0 A but a large discrepancy at 100 A and 200 A, which will discuss next. Further, GPT does not show any notable effect of magnetization on the space charge current limitation.

Although GPT does not show any notable effect of magnetization on space charge current limitation, it shows higher beam extraction achievable for magnetized beam than for non-magnetized beam. This is mainly because the cathode solenoid focuses the beam from the beginning of beam flight, minimizing the beam loss. Figure 77 illustrates the simulated beam trajectory (left) and the beam loss along the beamline for 0 A, 100 A, and 200 A cathode solenoid currents (right). Nevertheless, as depicted in Fig. 76, much higher beam extraction was estimated for cathode solenoid current at 100 A than at 200 A because of mismatch oscillation that resulted from non-uniform cathode magnetic field Fig. 43. Thus, the beam size is smaller in 100 A case than in 200 A, and the beam loss varies accordingly.

Nonetheless, Fig. 78 shows GPT simulations of delivered charge for different cathode solenoid currents at 1 cm, after the anode and at the dump when the gun is at 225 kV, 75 ps (FWHM) pulse width, 1.2 mm (rms) beam size, 6 nC initial bunch charge and focusing solenoids are optimized for maximum charge delivery. At 1 cm the charge extracted for all the solenoid currents is the same, which implying that the charge extracted does not depend on the magnetization strength. Further, the charge delivered through the anode aperture and charge collected at the dump is purely dependent on the beam size variation with the solenoid current due to mismatch oscillations.

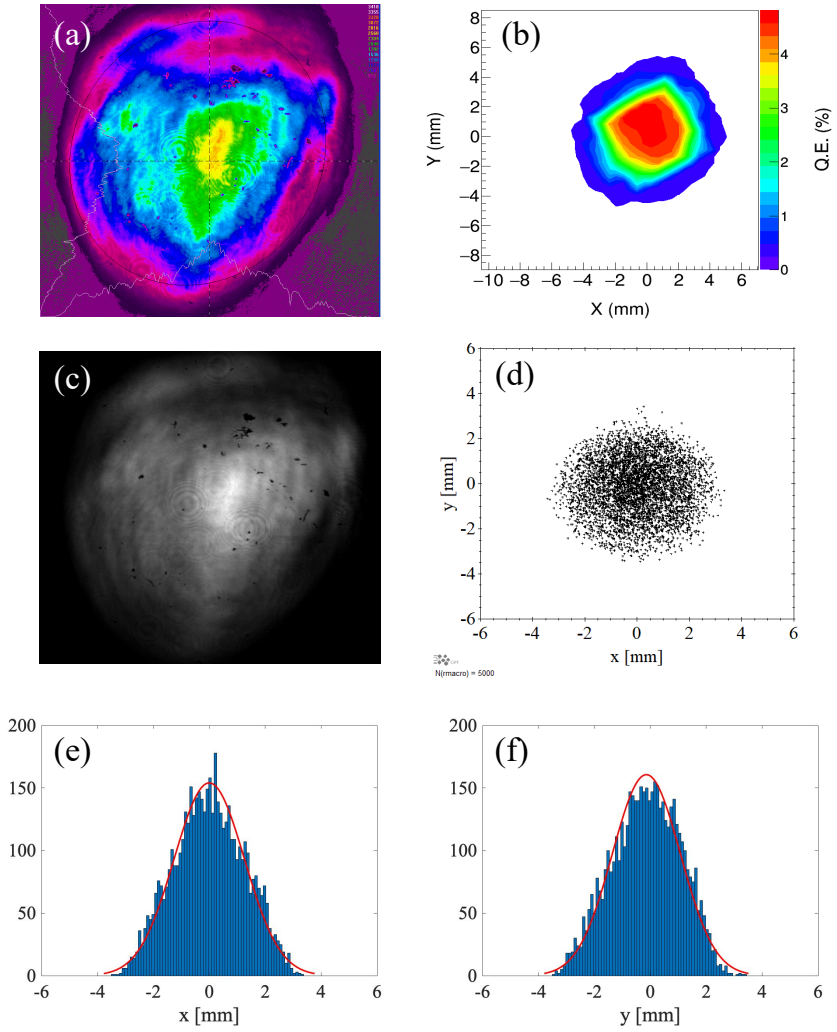

FIG. 75: (a) Laser profile. (b) QE profile. (c) GPT input gray-scale image. (d) Initial particle distribution from the image. (e) x distribution at the cathode with the Gaussian fit. (f) y distribution at the cathode with the Gaussian fit.

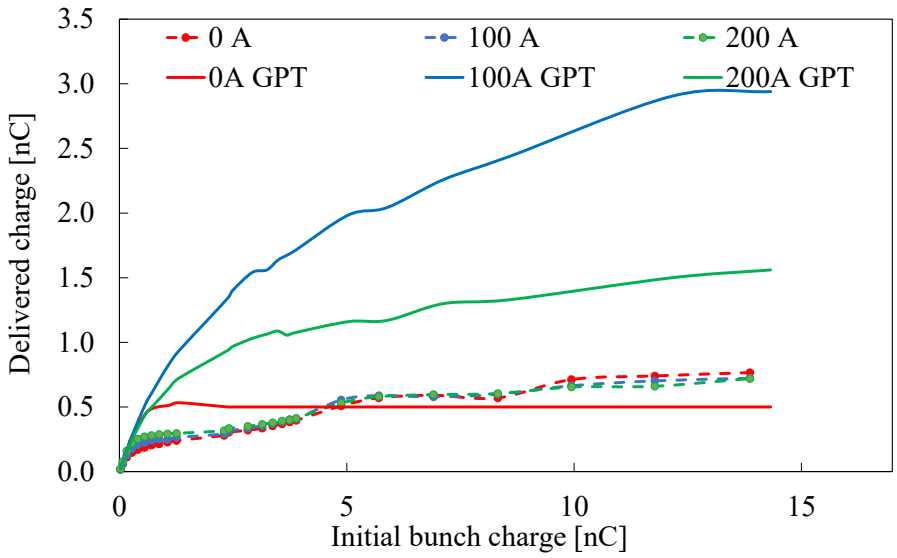

FIG. 76: Delivered charge at the dump vs initial bunch charge for 0, 100 and 200 A cathode solenoid currents (225 kV, 50 kHz, 75 ps (FWHM), 1.2 mm (rms)).

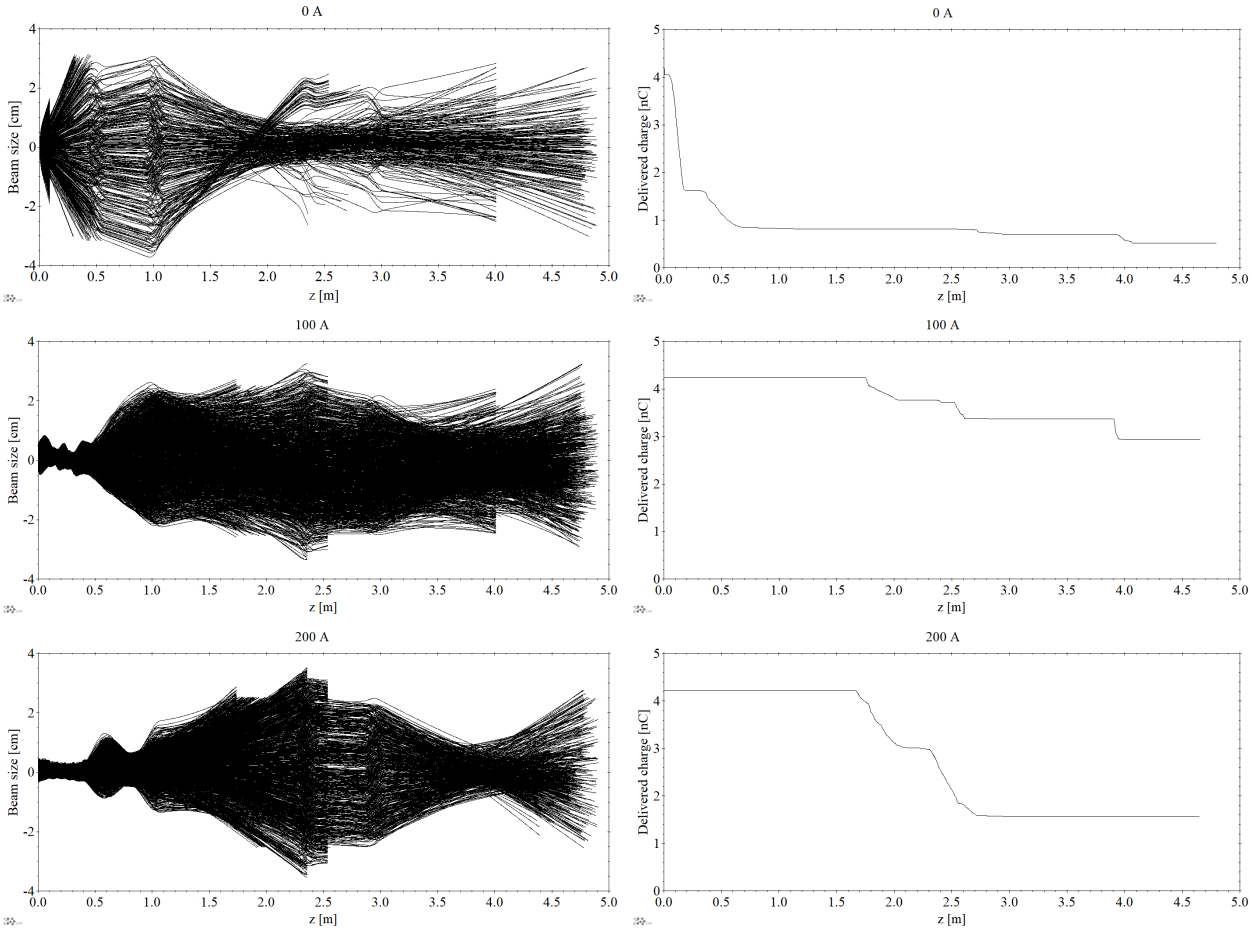

FIG. 77: Beam trajectory (left) Beam loss (right) along the beamline for 0 A, 100 A, and 200 A.

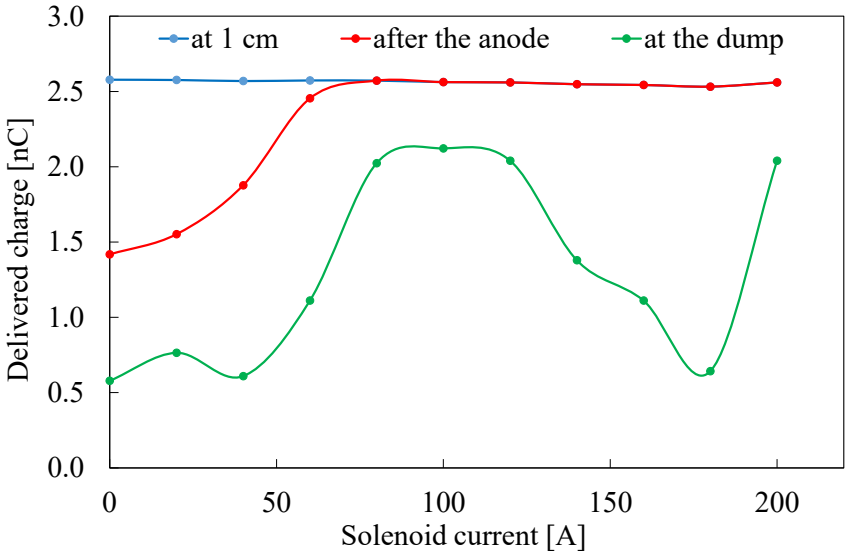

FIG. 78: GPT simulations of delivered charge for different cathode solenoid currents at 1 cm from the cathode, after the anode and at the dump. (225 kV, 50 kHz, 75 ps (FWHM), 1.2 mm (rms), 6 nC initial bunch charge).

6.2 AS A FUNCTION OF GUN VOLTAGE

According to Child's law, the charge extracted from the photocathode depends on the gun voltage Eq. 105. Hence, the above experimental procedure was repeated using various gun voltages (200, 150, and 100 kV) for magnetized and non-magnetized beams, and simulations were performed using GPT software with the same beam parameters and digitized laser profile. Figure 79 shows (a) laser profile, (b) QE profile, (c) GPT input gray-scale image, (d) initial particle distribution from the image, (e) x distribution at the cathode with the Gaussian fit, and (f) y distribution at the cathode with the Gaussian fit. According to the Gaussian fit, the laser rms size was 1.1655 mm in x and 1.1668 mm in y. Figure 80 illustrates the measured charge vs. expected bunch charge (top) and corresponding GPT simulations (bottom) for different gun high voltages for magnetized and non-magnetized beam (0 A and 150 A). These plots show the expected results. Namely, higher gun voltage permits the delivery of a higher bunch charge beam.

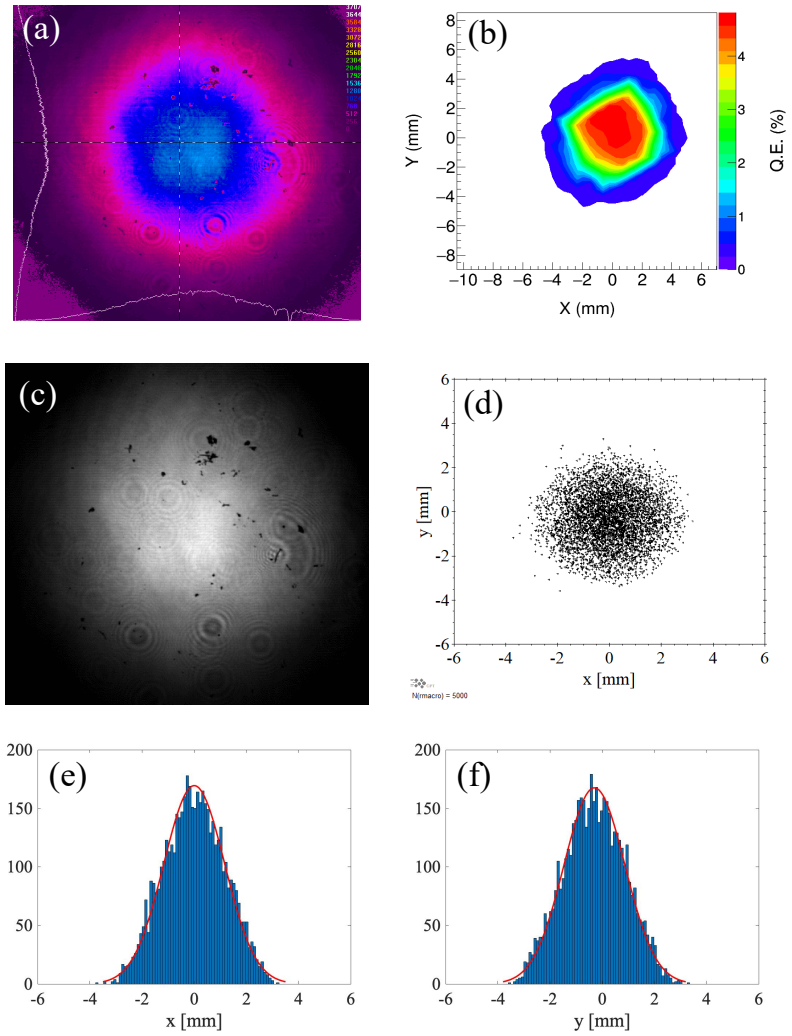

FIG. 79: (a) Laser profile. (b) QE profile. (c) GPT input gray-scale image. (d) Initial particle distribution from the image. (e) x distribution at the cathode with the Gaussian fit. (f) y distribution at the cathode with the Gaussian fit.

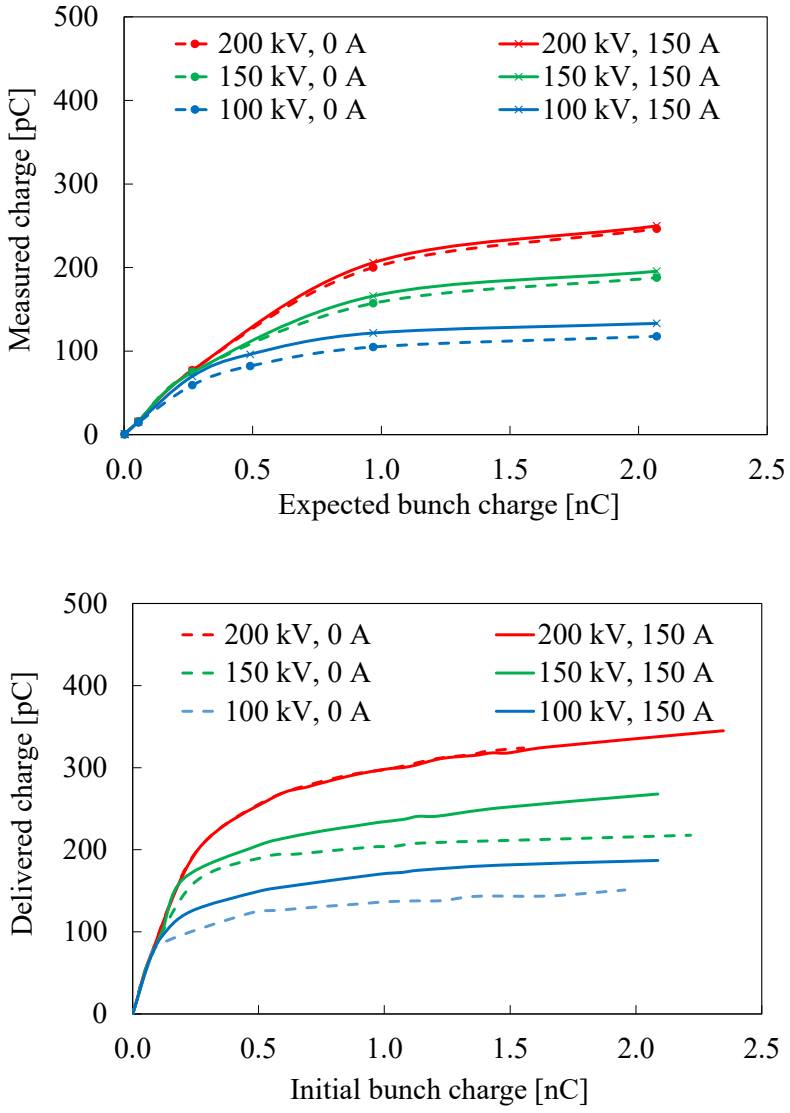

FIG. 80: Measured charge vs expected bunch charge (top) and corresponding GPT simulations (bottom) for different gun high-voltages for magnetized and non-magnetized beam (50 kHz, 1 ps, 1.16 mm (rms)).

6.3 AS A FUNCTION OF BUNCH DIMENSIONS

As discussed in chapter 4, the Coulomb repulsive forces inside a bunch are inversely proportional to its dimensions, *i.e.*, the transverse and longitudinal bunch sizes. Hence, the above experimental procedure was repeated using a variety of laser spot sizes (1.00, 0.50, and 0.25 mm), and laser pulse widths (1 ps, and 120 ps) for magnetized and non-magnetized beam and simulations were performed using GPT software with same beam parameters and digitized laser profile. Figure 81, 82, and 83 show (a) laser profile, (b) QE profile, (c) GPT input gray-scale image, (d) initial particle distribution from the image, (e) x distribution at the cathode with the Gaussian fit, and (f) y distribution at the cathode with the Gaussian fit for the three different laser spot sizes used. According to the Gaussian fit the laser rms size for Fig. 81 was 0.8105 mm in x and 0.8162 mm in y, for Fig. 82 0.4392 mm for both x and y, and for Fig. 83 0.2410 mm for both x and y. Figure 84 illustrates the measured charge vs. expected bunch charge (top) and corresponding GPT simulations (bottom) for different laser spot sizes for magnetized and non-magnetized beam (0 A and 150 A).

Further, Fig. 79, and 85 show (a) laser profile, (b) QE profile, (c) GPT input gray-scale image, (d) initial particle distribution from the image, (e) x distribution at the cathode with the Gaussian fit, and (f) y distribution at the cathode with the Gaussian fit for the two different laser pulse widths used. According to the Gaussian fit, the laser rms size for Fig. 85 was 1.1421 mm in x and 1.1210 mm in y . Figure 86 illustrates the measured charge vs. expected bunch charge (top) and corresponding GPT simulations (bottom) for different laser pulse widths for magnetized and non-magnetized beam (0 A and 150 A).

Hence, Fig. 84 and Fig. 86 agree with the Coulomb repulsive force equation where, by increasing the bunch dimensions, the space charge force can be suppressed to increase the extracted charge.

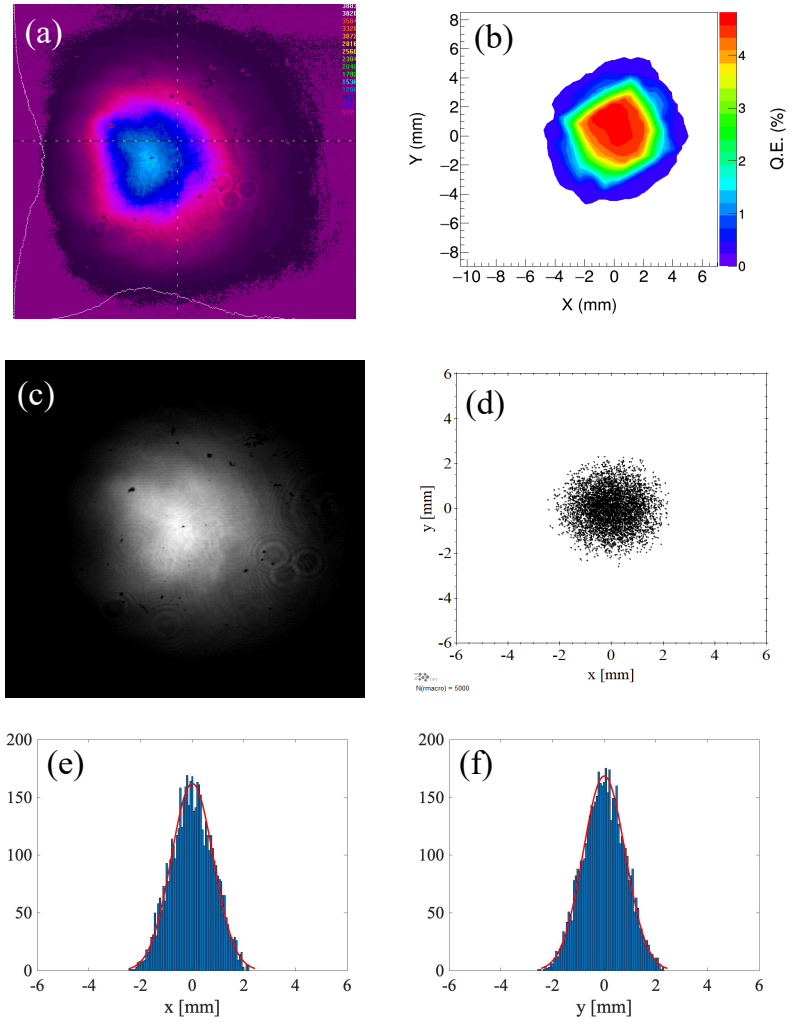

FIG. 81: (a) Laser profile. (b) QE profile. (c) GPT input gray-scale image. (d) Initial particle distribution from the image. (e) x distribution at the cathode with the Gaussian fit. (f) y distribution at the cathode with the Gaussian fit.

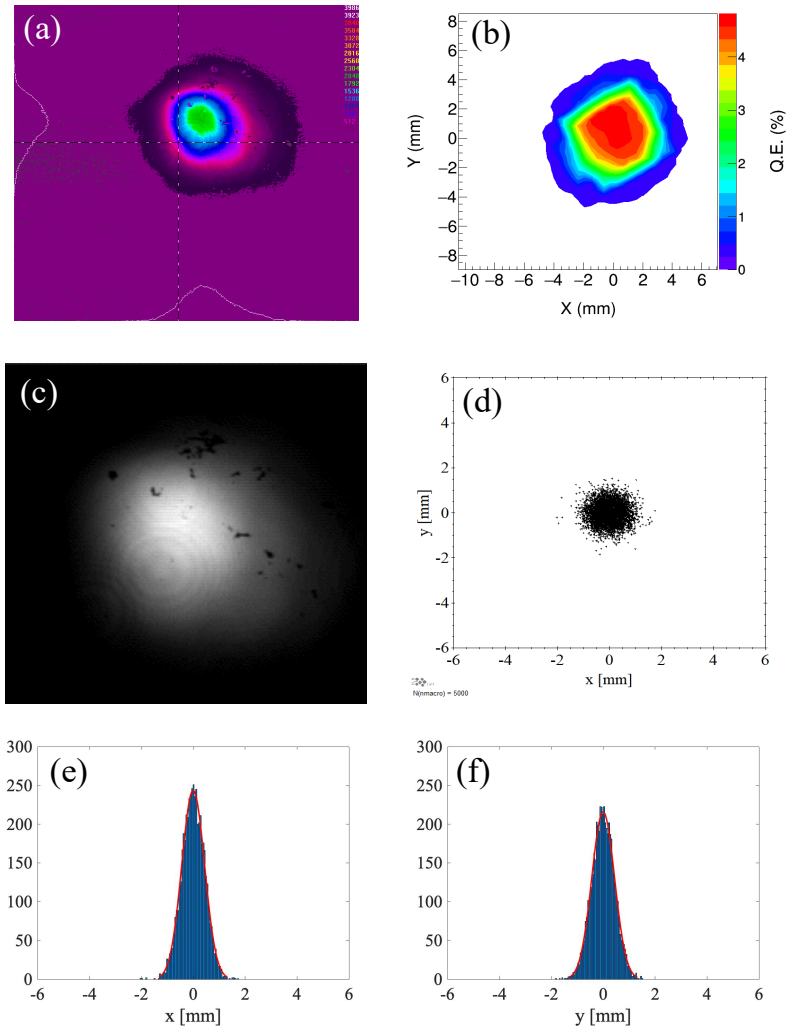

FIG. 82: (a) Laser profile. (b) QE profile. (c) GPT input gray-scale image. (d) Initial particle distribution from the image. (e) x distribution at the cathode with the Gaussian fit. (f) y distribution at the cathode with the Gaussian fit.

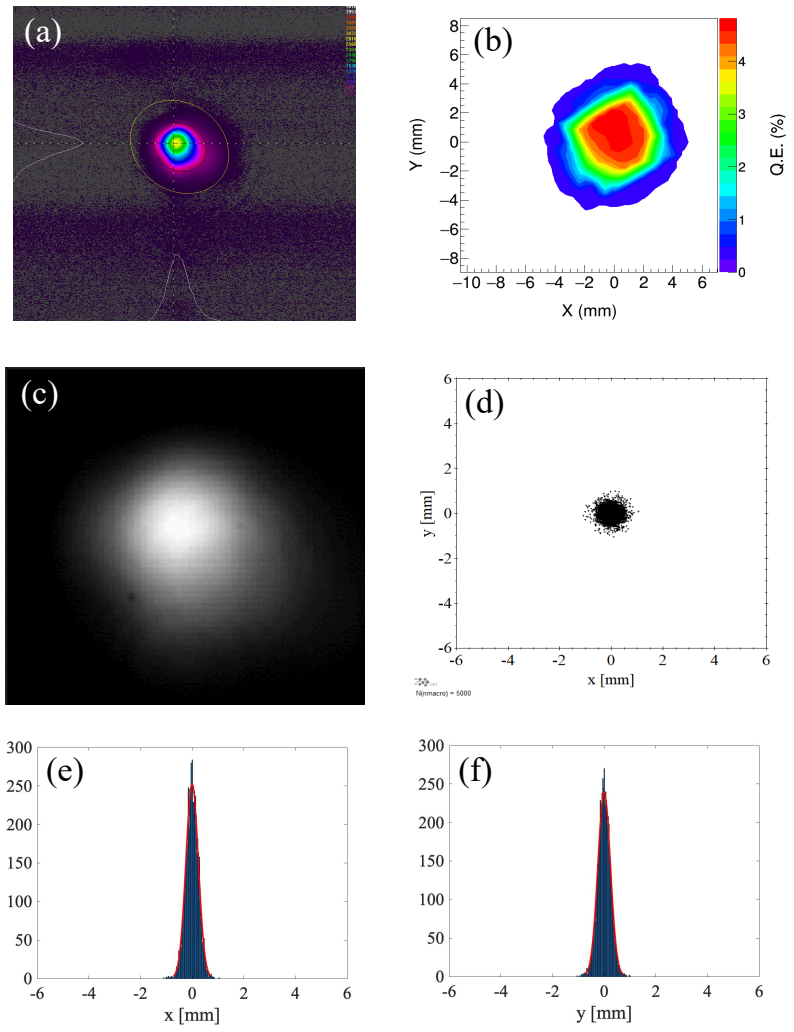

FIG. 83: (a) Laser profile. (b) QE profile. (c) GPT input gray-scale image. (d) Initial particle distribution from the image. (e) x distribution at the cathode with the Gaussian fit. (f) y distribution at the cathode with the Gaussian fit.

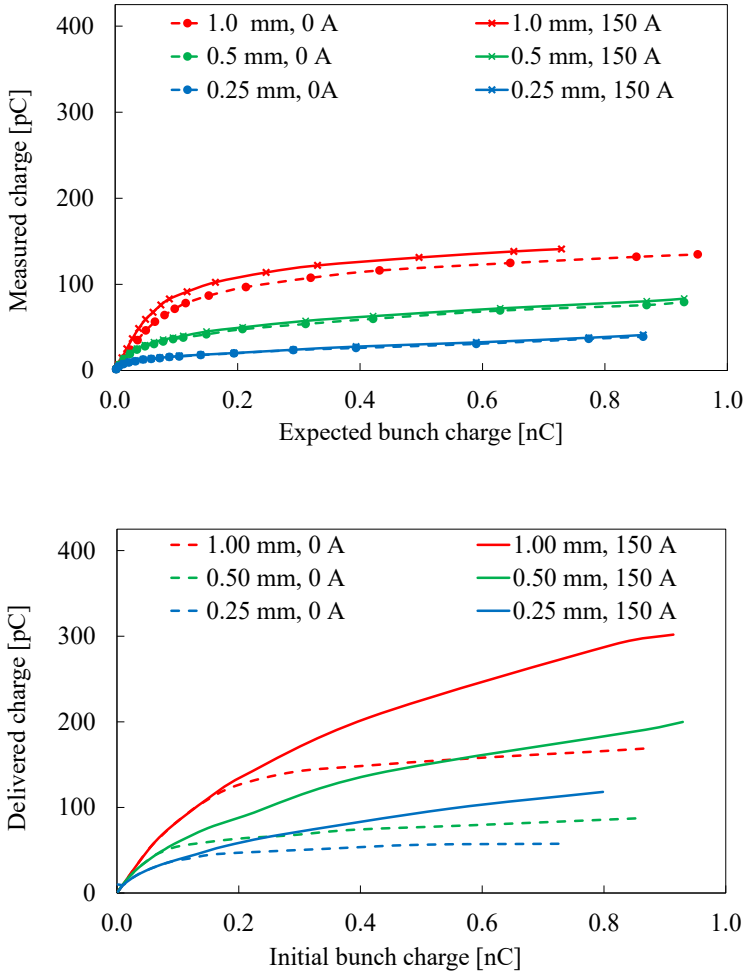

FIG. 84: Measured charge vs expected bunch charge (top) and corresponding GPT simulations (bottom) for different laser spot sizes for magnetized and non-magnetized beam (100 kV, 50 kHz, 70 ps (FWHM)).

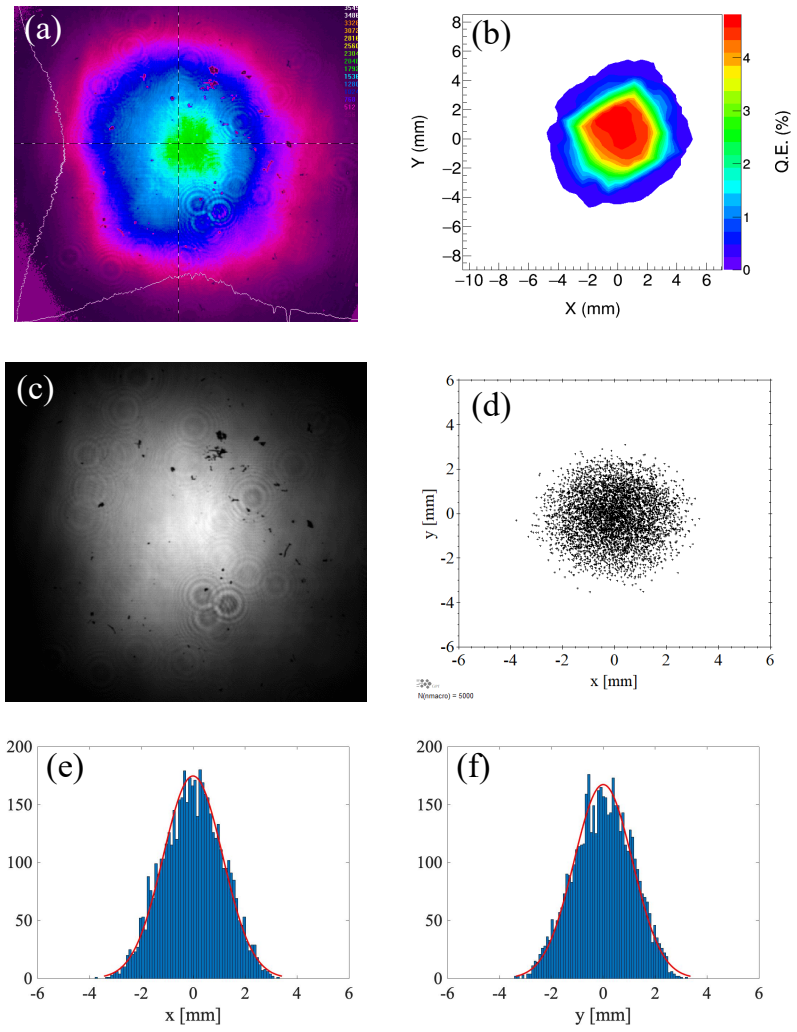

FIG. 85: (a) Laser profile. (b) QE profile. (c) GPT input gray-scale image. (d) Initial particle distribution from the image. (e) x distribution at the cathode with the Gaussian fit. (f) y distribution at the cathode with the Gaussian fit.

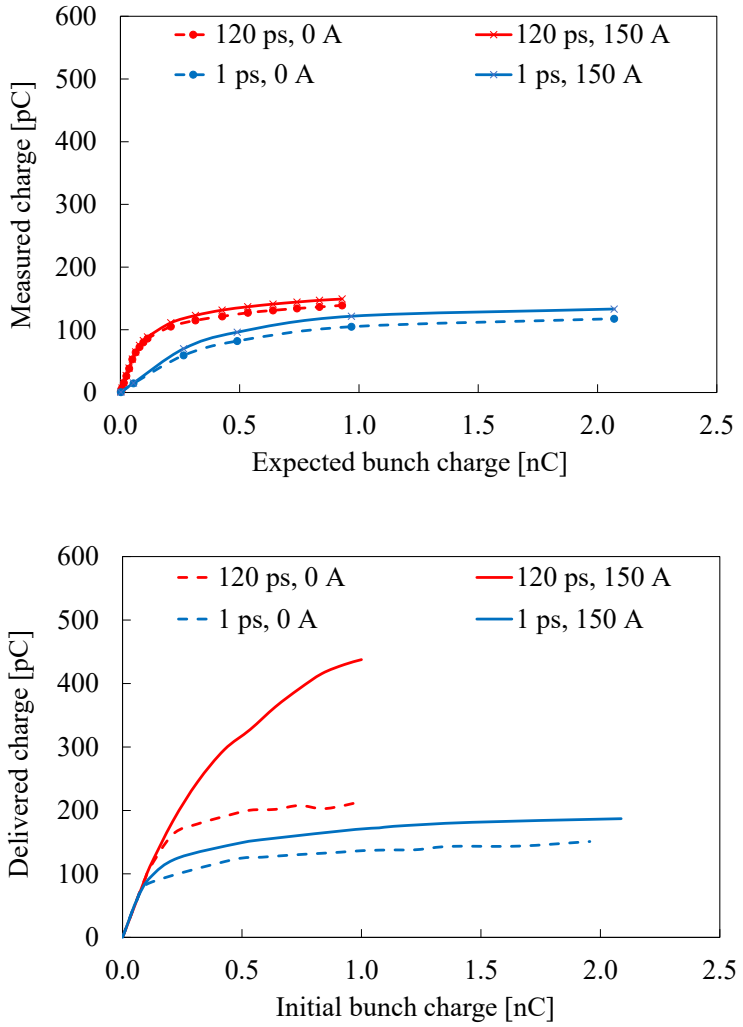

FIG. 86: Measured charge vs expected bunch charge (top) and corresponding GPT simulations (bottom) for different laser pulse widths for magnetized and non-magnetized beam (100 kV, 50 kHz, 1.15 mm (rms)).

CHAPTER 7

REDESIGN OF THE 300 KV PHOTO-GUN FOR HIGH BUNCH CHARGE OPERATIONS

DC high-voltage photo-guns are capable of providing reliable CW beam with high average current (∼100 mA) and low emittance (< 1 mm mrad) for a variety of accelerator applications. Jefferson Lab's Continuous Electron Beam Accelerator Facility (CEBAF) is one such application that uses DC high voltage photo-gun to produce highly polarized electron beams at current 100 μA from GaAs based photocathode [18]. FELs, Energy Recovery Linacs (ERLs), and electron cooling beamlines are some other applications that use DC high voltage photo-guns to provide unpolarized electron beams with high bunch charge and high average current. The majority of these guns, including ours, employ Pierce geometry at the cathode front to focus the beam, inverted insulator geometry to connect the high voltage cable to the cathode electrode and protect it from arcing, and a triple point junction shield to minimize the electric field at the insulator-metal-vacuum interface known as the triple point junction. However, the Pierce geometry reduces the E_z at the cathode. Thus it increases the space charge effects and reduces the charge extraction. Besides, inverted insulator and triple point junction screening electrode combine to introduce asymmetric electric fields in between the anode-cathode gap, which then result in deflecting the beam vertically at the exit of the anode, difficulty in beam steering and ultimately beam losses [18, 47, 48, 49]. This chapter discusses the redesign of our photo-gun to resolve the above design issues, and obtain a higher E_z at the cathode while keeping the beam centered and minimizing the electric field at the triple point junction and its performance.

7.1 EXISTING ELECTROSTATIC DESIGN

Gun designing is an optimization between achieving desired high voltage and maintaining required mechanical features and vacuum levels. For our case, it achieving reliable operation at 300 kV high voltage with high-quality beam and 10^{-12} Torr scale vacuum without field emission and high voltage breakdown. For voltages > 100 kV, field emission, and high voltage breakdown are often the main limiting factors related to reliable DC photo-gun operation.

Field emission mainly depends on the electric field strength inside the gun chamber, determined by the applied high voltage, cathode size, radius of curvatures of the components, anode-cathode gap, and the distance to the vacuum chamber walls. According to past experience, the field emission can be negligible when the electric field strength inside the gun chamber is ≤-10 MV/m after the high voltage conditioning [18].

High voltage breakdown (arcing) mainly occurs along with the high voltage cable termination. The transverse component of the electric field near the triple point junction can drag charged particles towards the insulator surface, inducing a secondary electron emission avalanche, which can then discharge gas that, once ionized, can lead to breakdown. Also, charge accumulation on the insulator surface can lead to breakdown by changing the electric field distribution near the insulator surface. This can be prevented by using a screening electrode that reduces the field strength at the triple point junction. Adequately designed triple point junction screening electrode can also linearize the potential across the insulator [50]. However, since this amplifies the field asymmetry in between the anode-cathode gap and the beam deflection at the exit of the anode, the dimensions of the screening electrode should be chosen to minimize both field strength at the triple point junction and beam deflection.

In order to design, optimize geometries, solve electrostatic fields and obtain the field maps of the photo-gun, the CST Studio Suite's electromagnetic field solver was used (see Appendix B) [51]. Since the whole design is cylindrically asymmetric, a 3D modeling software like CST can help obtain more accurate results than many 2D electrostatic solver software.

Figure 87 shows the 3D CST model of the existing photo-gun design considering the above aspects. It mainly includes a spherical cathode electrode with 1.2 cm front face and 25° Pierce focusing geometry, an electrically isolated anode with slightly curved front face to match to the Pierce geometry of the cathode front, placed at 9 cm away from the cathode front, inverted ceramic insulator, triple point junction shield, and an array of eight NEG pump modules.

Figure 88 shows the electrostatic fields inside the gun chamber when applying a 350 kV at the cathode electrode, 0 V at the anode, and 0 V at the outer chamber. The color code represents the field strength in V/m. Inside the cathode electrode, the electric field is zero. The electric field at the cathode front is -2.5 MV/m which is relatively small to deliver nC beam. The highest fields can be seen where the radius of curvature is lower, but they are almost within the range of 0 to -10 MV/m for reliable operation.

Figure 89 shows the location of the triple point junction (left), and a closer look at the electrostatic fields at the triple point junction (right). The design of the screening electrode

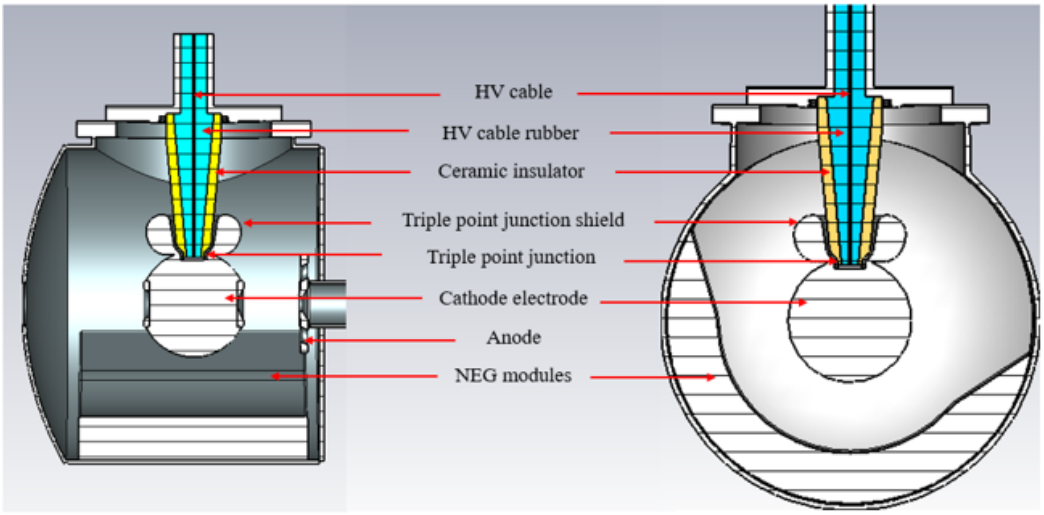

FIG. 87: Side view cross section with the anode-cathode gap (left). Front view cross section looking from the anode (right).

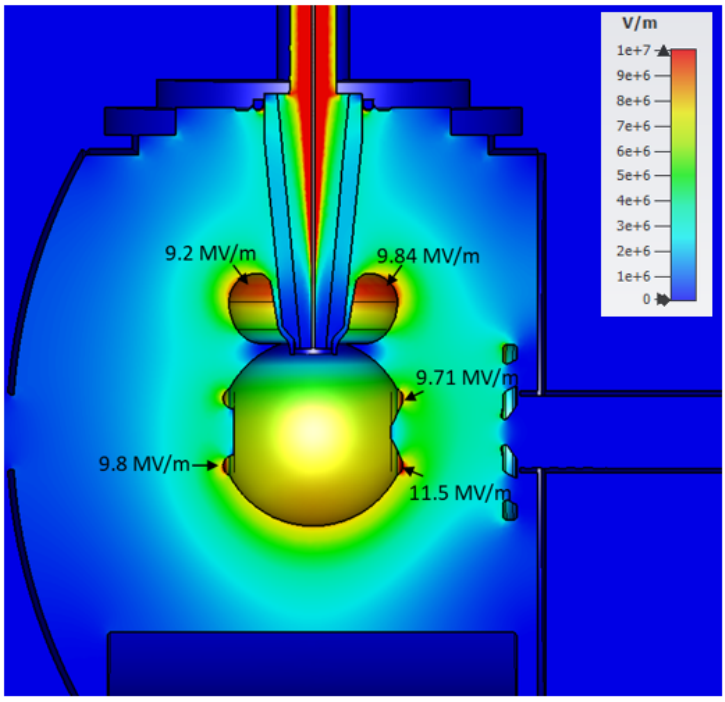

FIG. 88: Electrostatic design of the existing photo-gun at 350 kV at the cathode, 0 V at the anode. The color represents the electric field strength in V/m.

includes an iterative approach when deciding the height and the outer radius. The height of the screening electrode influences the potential along the insulator, especially at the interface between the insulator and the high voltage plug. A taller screening electrode creates a more linear change in the potential, but it will increase the field strength at its cusp because it has moved closer to the grounded vacuum chamber wall. The outer radius influences the electric field between the anode-cathode gap. Thus, it should be smaller than the spherical electrode radius to minimize distortions [52]. This screening electrode model was able to reduce the electric field at the triple point junction to ∼-10 MV/m (Fig. 89 (right)) from ∼-100 MV/m with no screening electrode as in Fig. 90.

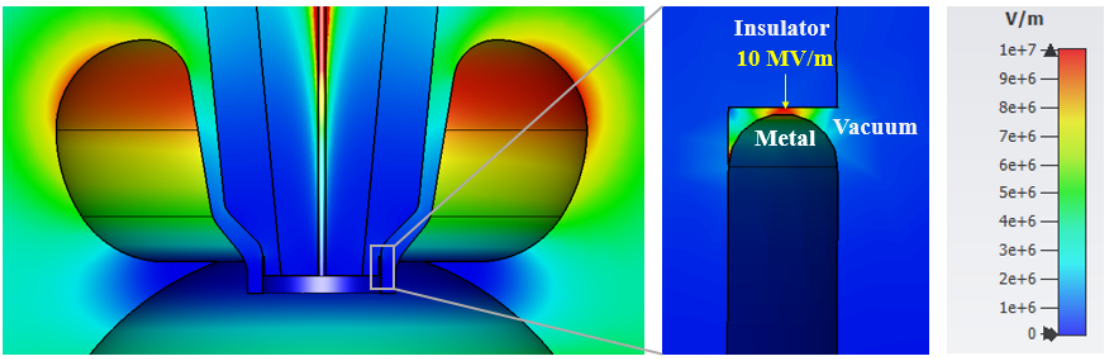

FIG. 89: Electric fields at the triple point junction when the photo-gun biased at 350 kV at the cathode, 0 V at the anode. The color represents the electric field strength in V/m.

Figure 91 compares the potential drops along with the interface between the high-voltage rubber cable plug and the ceramic insulator with and without the screening electrode for cathode electrode biased at 350 kV. The potential drop is more uniform along the insulator surface with the screening electrode.

Figure 92 shows the electric potential distribution inside the gun chamber where the color code represents the potential strength in V.

Figure 93 shows the longitudinal electric field E_z variation along the z-axis between the anode-cathode gap when biased at 350 kV. Figure 94 (left) shows the E_x variations along

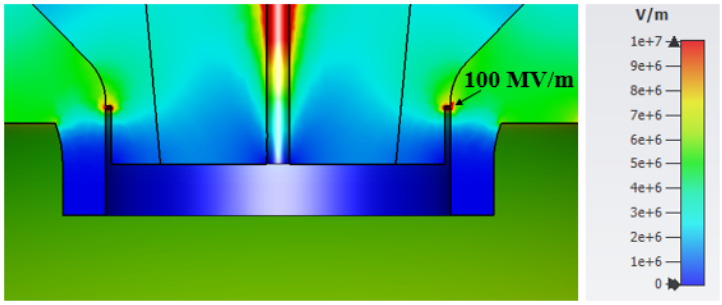

FIG. 90: Electric fields at the triple point junction when the photo-gun biased at 350 kV at the cathode, 0 V at the anode with no screening electrode. The color represents the electric field strength in V/m.

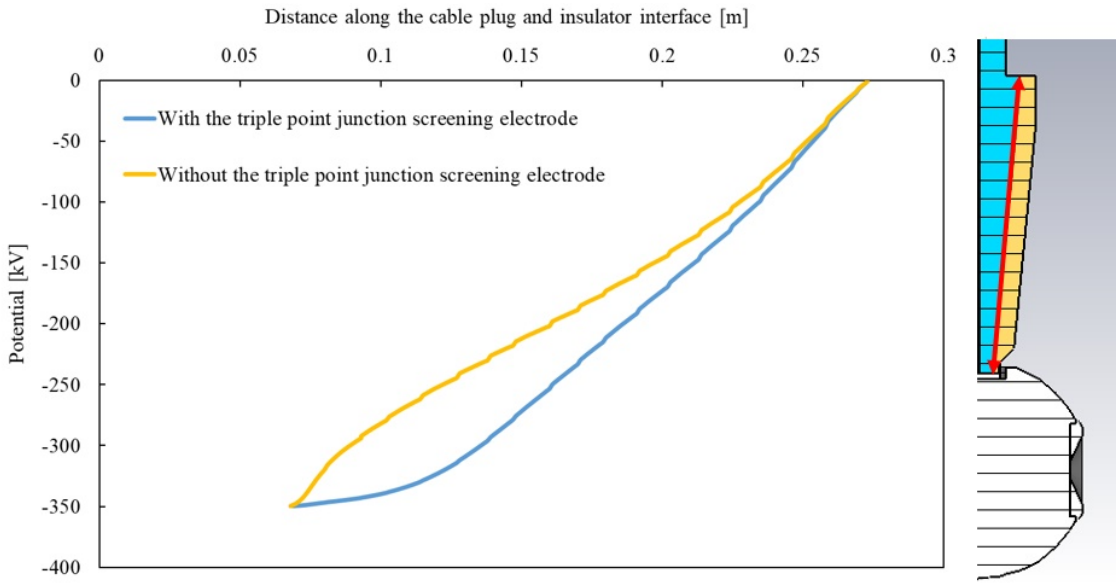

FIG. 91: The comparison of the potential drops along the interface between the high voltage rubber cable plug and the ceramic insulator (red arrow) with and without the triple point junction screening electrode for cathode electrode biased at 350 kV.

the dotted colored lines in the horizontal plane between the anode-cathode gap when biased at 350 kV, where each color line position is indicated with respect to the x-axis. Figure 94 (right) shows the E_y variations along the dotted colored lines in the vertical plane between the anode-cathode gap when biased at 350 kV, where each color line position is indicated with respect to the y-axis. The effect of the Pierce geometry can be seen in all of them where E_z reached its maximum not at the cathode front but ∼2 cm and E_x and E_y fields focused at the same position. E_x shows asymmetry in the horizontal plane, especially ∼9 cm, which is mainly due to the asymmetry in placing the NEG pumps at the bottom of our gun chamber (Fig. 87) as its activation feedthrough was in the way. E_y shows huge asymmetry in the y plane mainly due to the insulator and screening electrode.

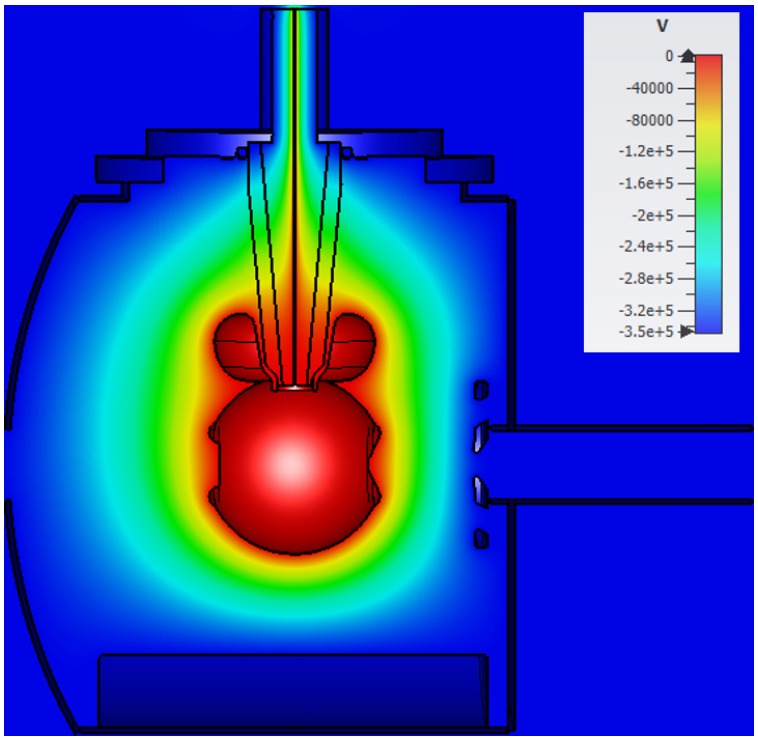

FIG. 92: Potential distribution of the existing photo-gun at 350 kV at the cathode, 0 V at the anode. The color represents the potential in V.

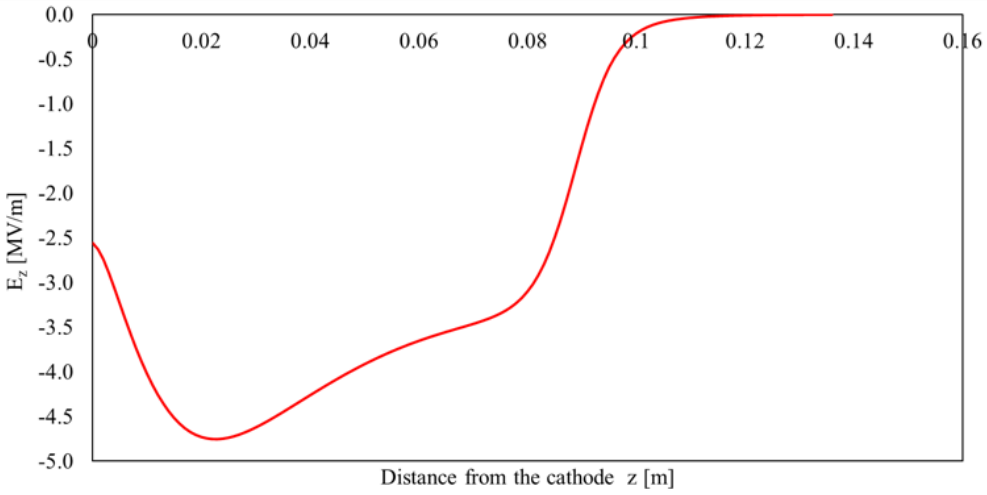

FIG. 93: The E_z vs z between the anode cathode gap when biased at 350 kV.

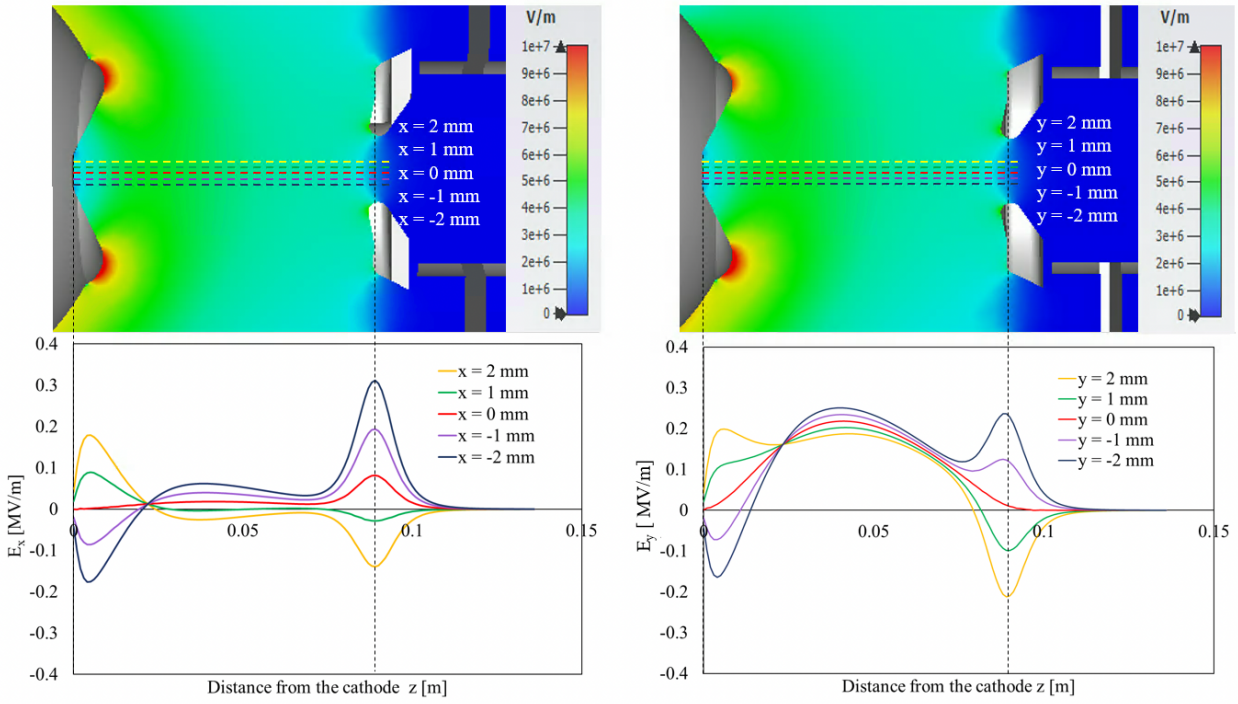

FIG. 94: E_x (left), E_y (right) variations along the dotted colored lines between the anode cathode gap when biased at 350 kV where each color line position is indicated with respect to the x-axis (left) and y-axis (right). The color represents the electric field strength in V/m.

In order to investigate the beam trajectories with the photo-gun design, GPT program was used [44]. The 3D electric field maps generated from CST were implemented in GPT with initial beam conditions and beamline components.

Figure 95 shows the beam trajectory of the non-magnetized beam along the z-axis for 1 m from the cathode in the x plane (left) and y plane (right). Simulations were done with 300 kV high voltage, 1 pC bunch charge, 75 ps FWHM Gaussian pulse width, 1 mm (rms) laser spot size, 3 cm beam pipe radius, no space charge calculations and no other beamline element, *i.e.*, steering magnets and focusing lenses. The trajectories show that the beam deflects $\sim$ 3 mm at z=1 m in the negative x-direction and $\sim$ 3.3 cm at z=1 m in the negative y-direction. The steering magnets should be employed just at the exit of the gun chamber in order to correct this deflection and minimize beam loss.

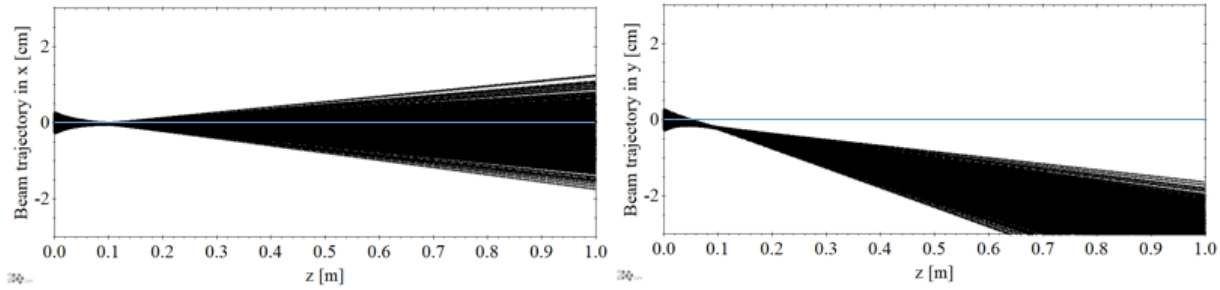

FIG. 95: Beam trajectories x plane (left), y plane (right).

The main research aim of designing this gun was to build a reliable compact (relatively small surface area) DC high-voltage photo-gun operating at 300 kV, which works favorably in achieving good vacuum levels compared to the photo-gun designs that employ large cylindrical insulators. Our team had succeeded in operating this photo-gun for over 1000 cumulative hours at 300 kV bias voltage with alkali-antimonide photocathodes and became the highest bias voltage ever achieved with an inverted-insulator design.

The accelerating electric field (E_z) at the photocathode sets the limit on the maximum charge density extractable from the photocathode. The maximum charge density supported

by the E_z is given by

$$\frac{d^2q}{dxdy} \approx \epsilon_0 E_z, \tag{132}$$

where ϵ_0 is the vacuum permittivity [53]. However, according to the experiments conducted so far, it seems unfeasible to deliver nC bunched charge beam with ∼-2.5 MV/m E_z at the photocathode. Thus, to reach that goal, the existing DC high voltage photo-gun was modified to increase E_z at the cathode and to correct the beam deflection exerted by the non-symmetric nature of the inverted insulator photo-gun, thus making the beam exit the anode centered while minimizing the electric field at triple point junction and field emission.

7.2 MODIFIED ELECTROSTATIC DESIGN

The E_z at the cathode mainly depends on the anode-cathode gap and, in our case, also with the Pierce geometry. Decreasing the anode-cathode gap can increase the E_z at the cathode, but the closer they get leads to a significant risk of field emission. Thus, the gap size is a trade-off between obtaining higher E_z and lowering the field emission.

Figure 96 shows how E_z varies with the anode-cathode gap from 4 cm to 9 cm without the Pierce geometry (flat cathode front and flat anode front). The cathode is placed at 0 m with an applied high voltage of 350 kV.

The plot shows a considerable increase in E_z at the cathode, ∼-5.5 MV/m from the original design, -2.5 MV/m just by removing the Pierce geometry, and it gradually increases with decreasing anode-cathode gap. Though the 4 cm gap gives the highest E_z at the cathode, it approaches the -10 MV/m limit. Therefore, in order to avoid the field emission risk, we settled with a 5 cm gap with no Pierce geometry, which provides -7.8 MV/m E_z at the cathode.

The next focus is on the beam deflection. Figure 97 shows the beam deflection in x (left) and y (right) directions with changing anode-cathode gap without the Pierce geometry. Here, the 3D field maps obtained from CST for each case were imposed into GPT program for beam simulations. Simulations were done with 300 kV high voltage, 1 pC bunch charge, 25 ps (rms) Gaussian pulse width, 1 mm (rms) laser spot size, 3 cm beam pipe radius, no space charge calculations, and no other beamline element, *i.e.*, steering magnets and focusing lenses. According to the plot, deflection in the x-direction has a minor impact on the anode-cathode gap. Conversely, deflection in the y-direction shows a significant impact from the anode-cathode gap. However, ultimately, lowering the gap lowers the beam deflection in both x and y-directions. Figure 98 illustrates how normalized emittance in x (left) and in

y (right) depend on the anode-cathode gap and Pierce geometry compared to the original design. When the anode-cathode gap decreases, the x and y normalized emittance approach to an expected value indicates good beam quality. This would be mainly due to the lower beam deflection with the reduced gap.

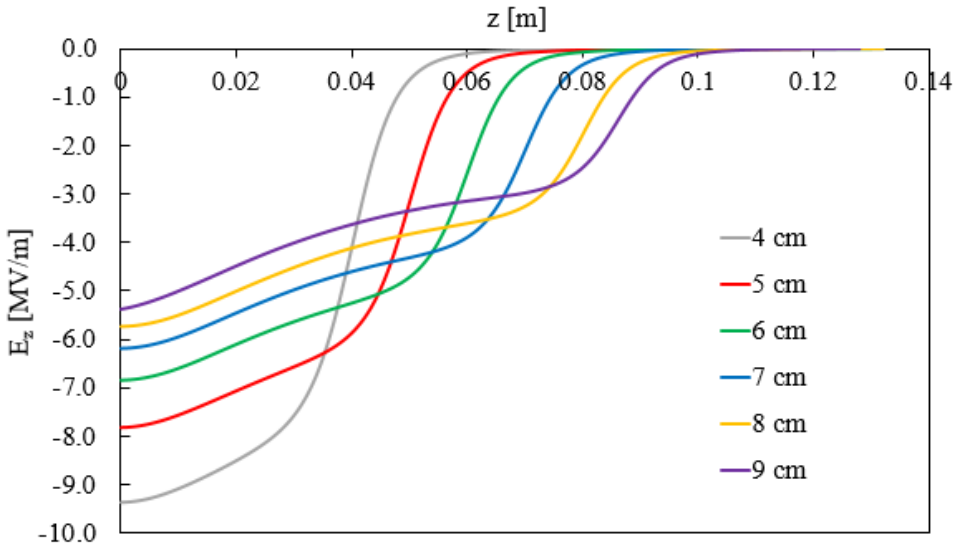

FIG. 96: E_z variation with anode-cathode gap for 350 kV.

Figure 99 shows how NEG modules and triple point junction screening electrodes affect the beam deflection in 5 cm anode-cathode gap design x-direction (left) and y-direction (right) (the scale is not the same in two plots). The left plot shows that the asymmetry in placing NEG modules is the main reason for the beam deflection in the x-direction. Removing them or replacing them with thinner stripes can fix this problem. The right plot shows that the triple point junction screening electrode is the main reason for the deflection in the y-direction.

Table 12 shows the electric field strength at the cathode and on the cathode electrode for different anode-cathode gaps with and without the NEG modules. It shows that removing

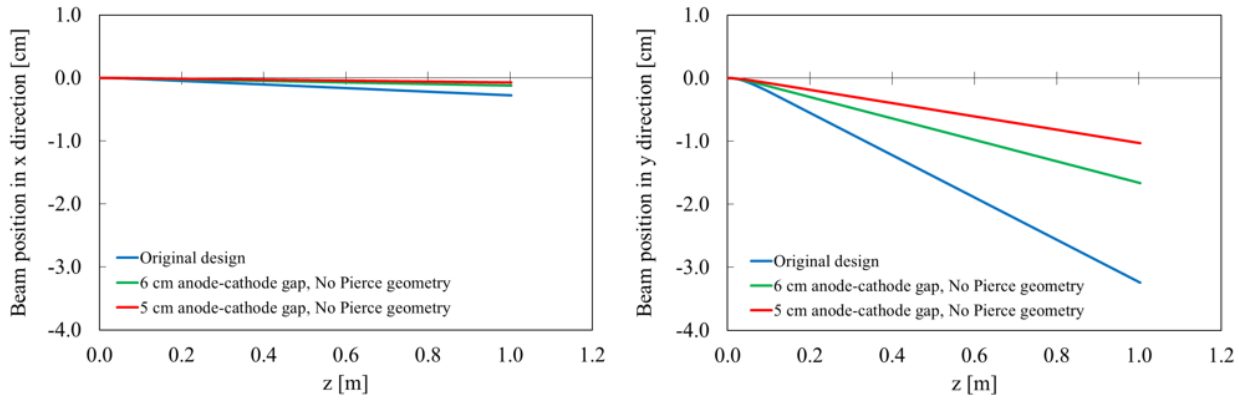

FIG. 97: Beam deflection with different anode-cathode gaps x-deflection (left). y-deflection (right).

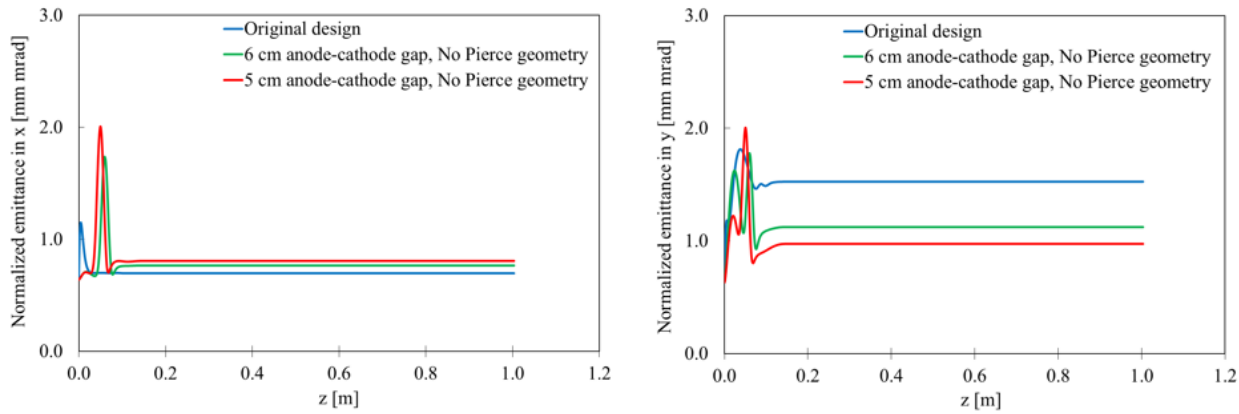

FIG. 98: Normalized emittance variation with different anode-cathode gaps x-deflection (left). y-deflection (right).

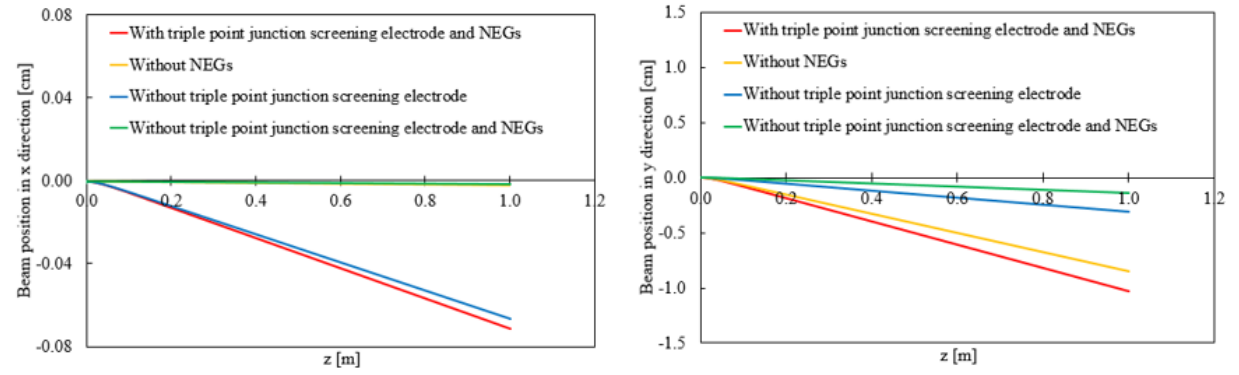

FIG. 99: Contribution of the different components to the beam deflection in 5 cm anode-cathode gap design x-deflection (left). y-deflection (right).

NEG modules reduces the electric field everywhere, but it is a negligible amount.

After thoroughly examining the design, a simple method that can cancel the effect from the triple point junction screening electrode was discovered, which is by shifting the anode. Figure 100 shows how beam deflection varies with anode shift (left) in x and (right) in y-directions, and Fig. 101 illustrates a closer look at how the beam deflects in the y-direction with the anode shift.

TABLE 12: Electric field values at 350 kV.

Design description	Pierce geometry	With NEGs		Without NEGs	
		E_z at the cathode [MV/m]	Max E on the cathode electrode [MV/m]	E_z at the cathode [MV/m]	Max E on the cathode electrode [MV/m]
Original design	Included	2.55	11.5	-	-
6 cm gap	Removed	7.01	10.2	6.93	9.31
5 cm gap	Removed	7.98	10.1	7.93	9.52

Since the anode was shifted only in the vertical direction, there is no effect on the deflection in the x-direction. However, it is very much sensitive to deflection in the y-direction. The right plot shows that the beam deflection in the y-direction originated due to the asymmetry in the electric field from the inverted insulator geometry, and the triple point junction screening electrode can essentially be canceled by shifting the anode $\sim$1.6 mm in the vertically downward direction. Figure 102 illustrates how normalized emittance depends on the anode shift in x (left) and in y (right). It established that at $\sim$ -1.6 mm shift, both x and y normalized emittances reach an expected value.

However, it is not easy to shift the whole anode as it breaks the symmetry of anode mounting flanges and the laser path. Therefore, after confirming how much shift is needed, a new model design from SolidWorks, shifting the anode aperture -1.6 mm while keeping

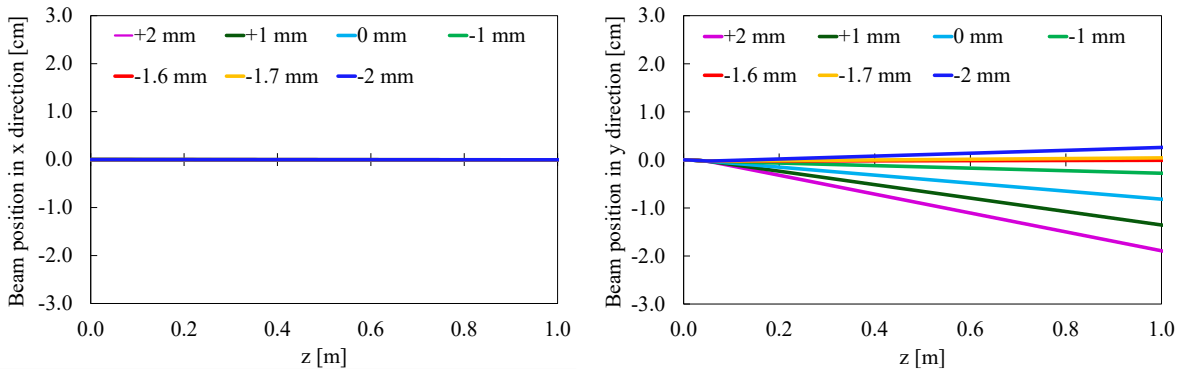

FIG. 100: Beam deflection varies with anode shift x-deflection (left). y-deflection (right).

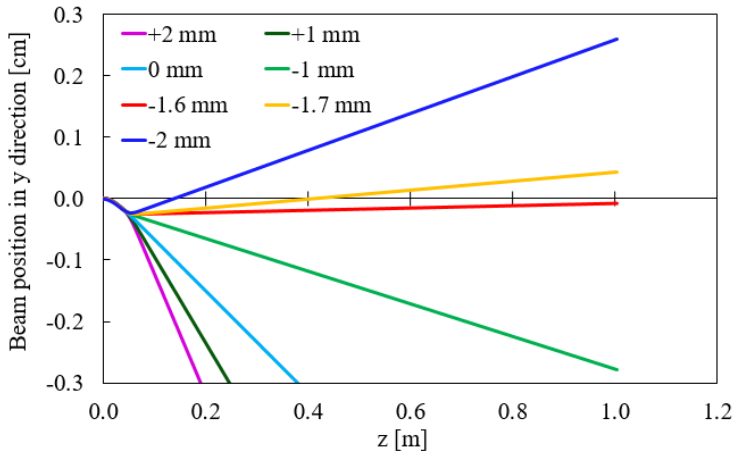

FIG. 101: Closer look of the beam deflection in y-deflection.

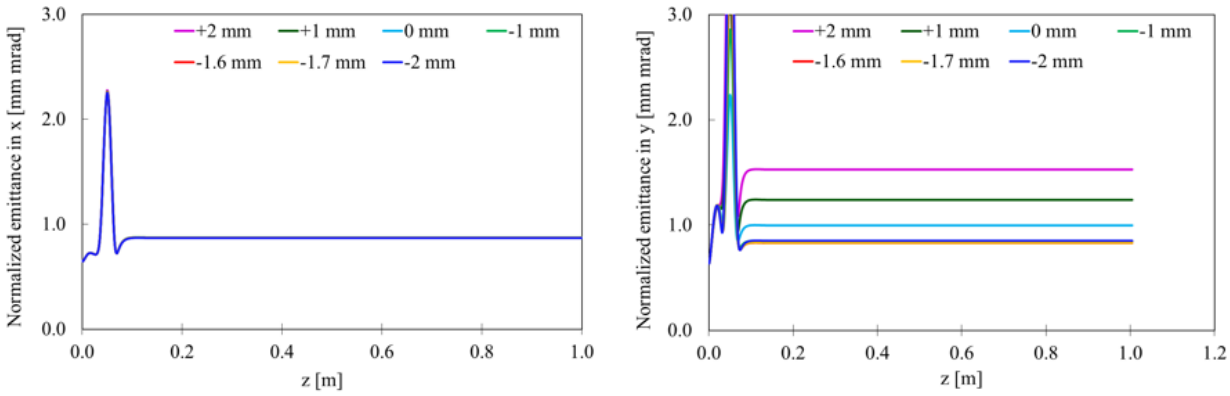

FIG. 102: Normalized emittance variation with the anode shift x (left) and y (right).

the anode centered and aligned with the cathode and beam pipe, was designed. Figure 103 shows the effect between shifting the whole anode and only the anode aperture -1.6 mm. The plots show that both give almost the same results.

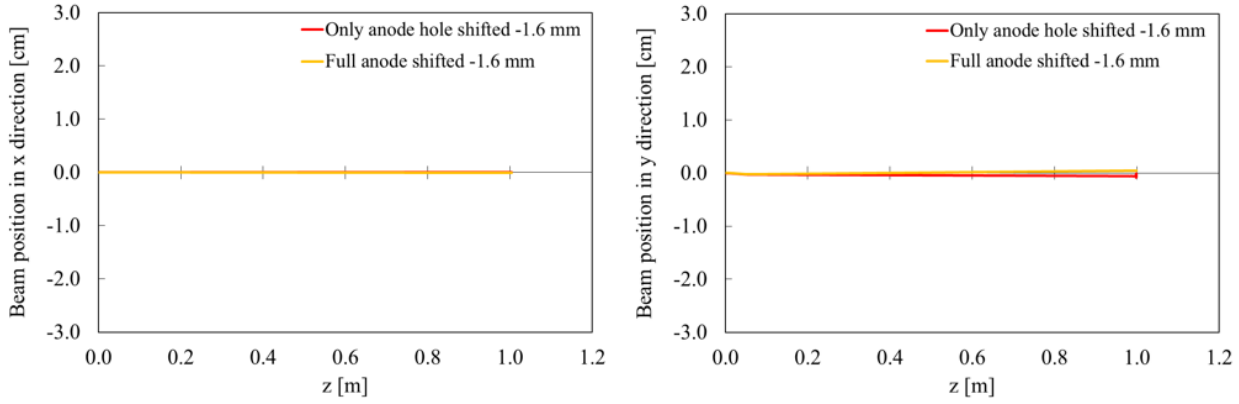

FIG. 103: Beam deflection by shifting the whole anode and only the anode hole x deflection (left). y deflection (right).

Figure 104 shows the final mechanical design of the gun with flat anode front and cathode front, 5 cm anode-cathode gap, and anode with -1.6 mm shifted aperture, and Fig. 105 shows the CST model modified according to the mechanical design. Figure 106 (a) shows the cathode electrode with the triple point junction screening electrode, (b) the flat cathode front, and (c) the anode mounting model with the flange connecting to the beam pipe. The mounting model was decided to have fewer metallic surfaces than a whole pipe that favors reducing field emission.

Figure 107 shows the electrostatic field distribution inside the gun chamber for 350 kV biased cathode and 0 V biased anode. The design was able to maintain almost -10 MV/m electric field strength limit everywhere inside the chamber. Though the electric field strength near the anode edge is -11 MV/m, it is 0 V biased. Therefore it will not trigger field emission.

Figure 108 shows the potential distribution inside the gun chamber for a 350 kV biased

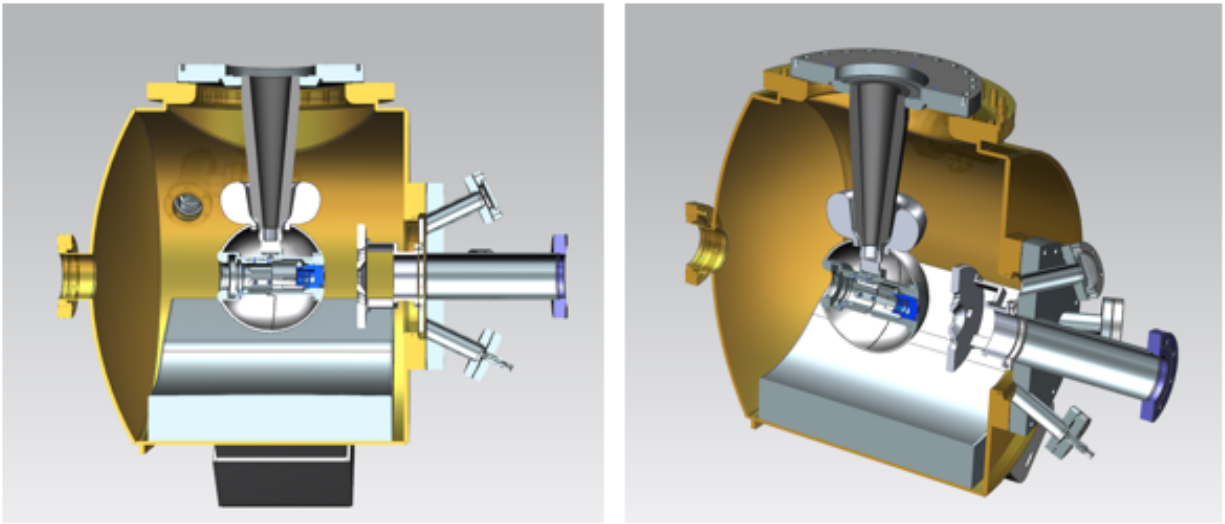

FIG. 104: Final mechanical design.

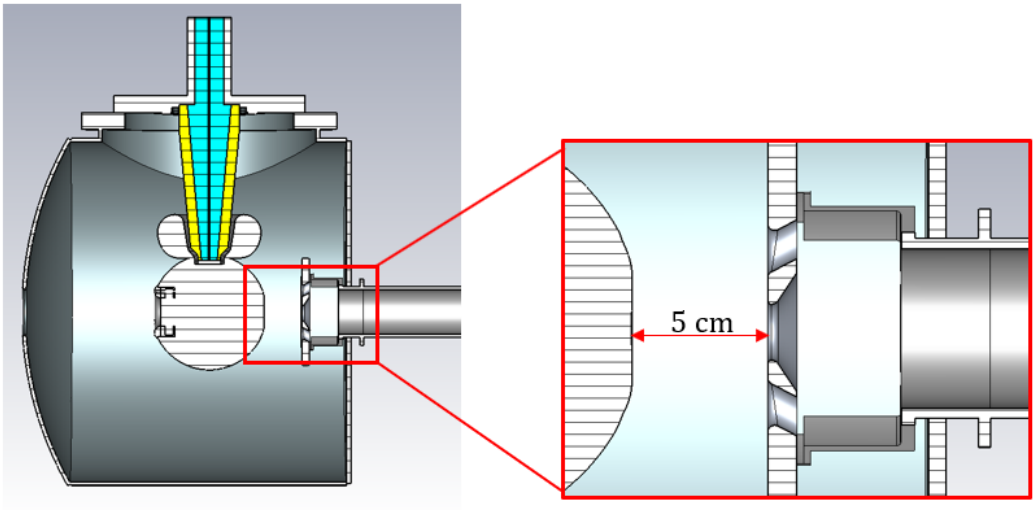

FIG. 105: CST model of the final design.

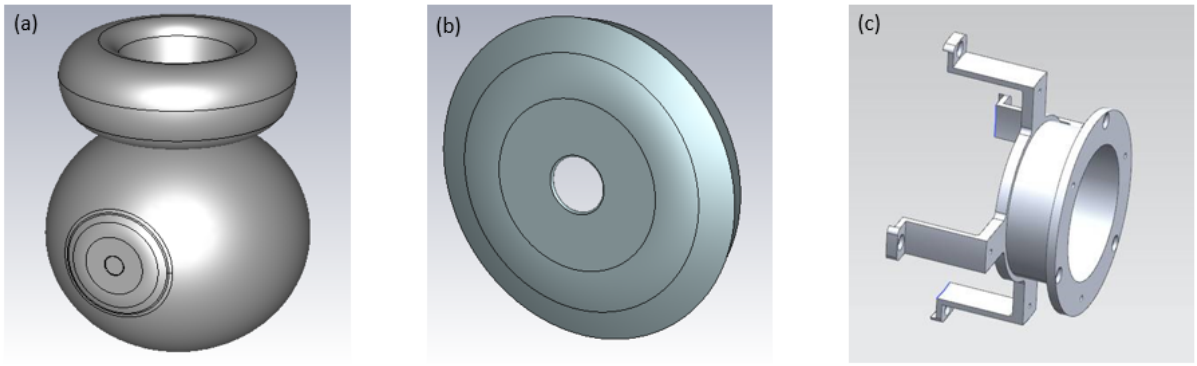

FIG. 106: (a) Cathode electrode with the triple point junction screening electrode. (b) Flat cathode front. (c) Anode mounting model.

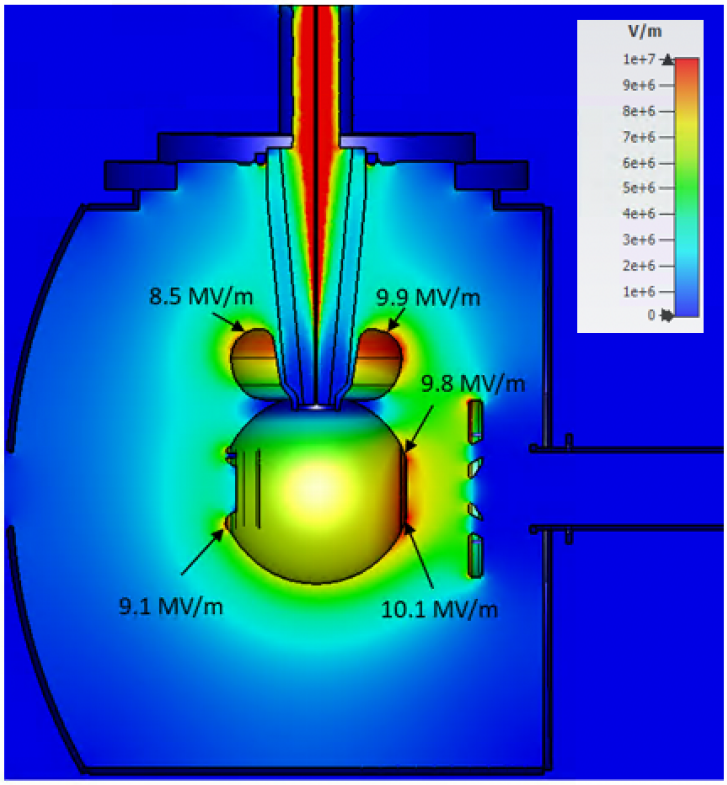

FIG. 107: Electrostatic field distribution for 350 kV biased cathode and 0 V biased anode. The color represents the electric field strength in V/m.

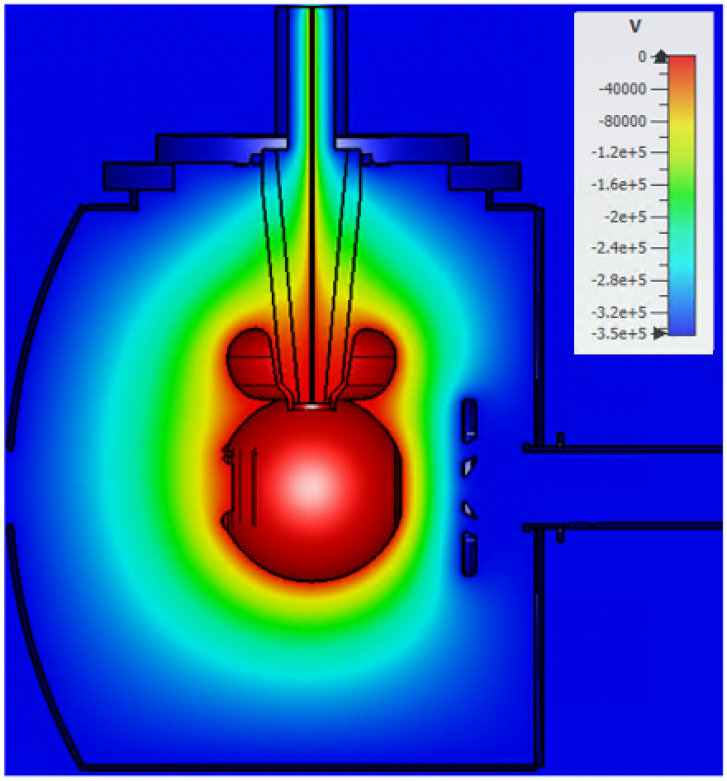

FIG. 108: Potential distribution for 350 kV biased cathode and 0 V biased anode. The color represents the potential in V.

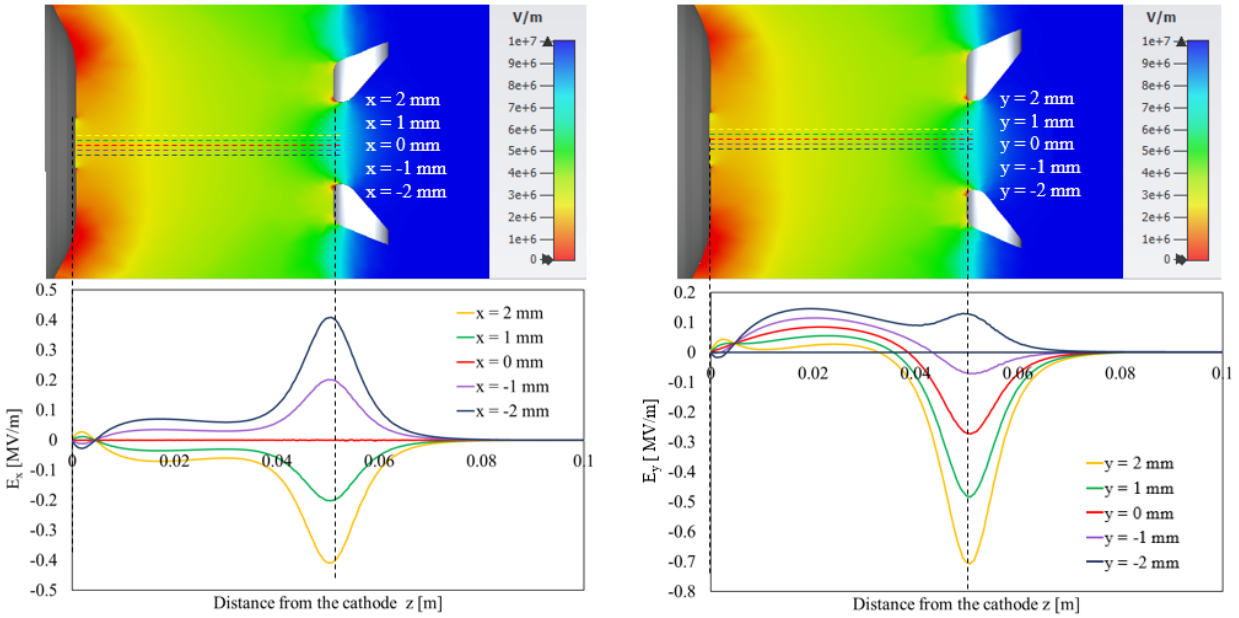

FIG. 109: E_x (left), E_y (right) variations along the dotted colored lines between the anode cathode gap when biased at 350 kV where each color line position is indicated with respect to the x axis (left) and y axis (right). The color represents the electric field strength in V/m.

cathode and 0 V biased anode. The horizontal (left) and vertical (right) electric field variations between the anode-cathode gap of the modified gun are illustrated in Fig. 109. The color map (top left graph) shows the E_x distribution within the anode-cathode gap, and the bottom left graph shows the magnitude of E_x along each of the colored dotted lines shown on the field map. The top right graph and the bottom right graph show the same for E_y. In both, the vertical position of each dotted line is indicated with respect to the axis. According to the left plots, the E_x is symmetric along the axis, but the right plots show that E_y is distorted first due to the inverted insulator and triple point junction screening electrode and then due to the shifted anode.

Figure 110 shows the beam trajectories in the x-direction (left) and in the y-directions (right). With the shifted anode beam is on-axis in both directions. Figure 111 shows the GPT simulations on the extracted charge at the cathode for different bunch charges from the existing gun at 225 kV and the modified gun at 300 kV for 0 A, 100 A, and 200 A. According to the results, the charge extracted from the photo-gun has doubled with the modified gun.

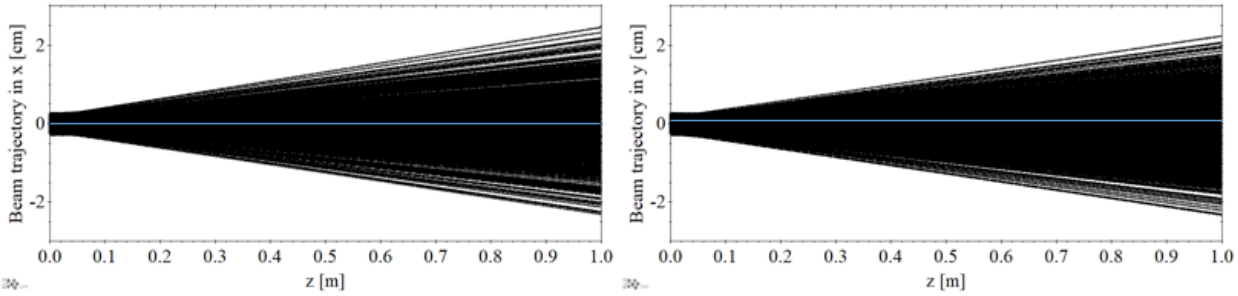

FIG. 110: Beam trajectory x (left) and y (right) directions.

In order to reduce the beam loss, the beamline should be modified by removing the components that have small beampipe apertures (*i.e.*, differential pump module) and add more Faraday cups to track the beam loss along the beamline. Fig. 112 illustrates the delivered charge at the dump for a few different cathode solenoid currents with the modified beamline. The results indicate that choosing a cathode solenoid current with the lowest beam

size throughout the beamline can deliver a higher bunch charge than before. Figure 113 illustrates how beam trajectory looks like and how beam loss occurs along the beamline for 0 A, 30 A, 180 A, and 200 A cathode solenoid currents.

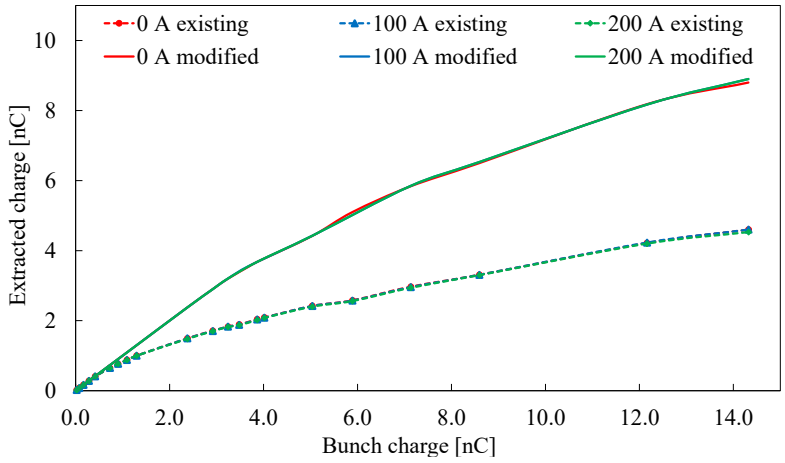

FIG. 111: Extracted charge at the cathode vs bunch charge from the existing gun and the modified gun for 0 A, 100 A, and 200 A (50 kHz, 75 ps (FWHM), 1.2 mm (rms)).

Figure 114 shows the new cathode front and anode, polished to a mirror-like surface condition with sandpapers, diamond polishing, and finally barrel polishing. Fig. 115 is the anode assembly and thin NEG stripes attached to the gun chamber. Fig. 116 shows the cathode electrode assembly.

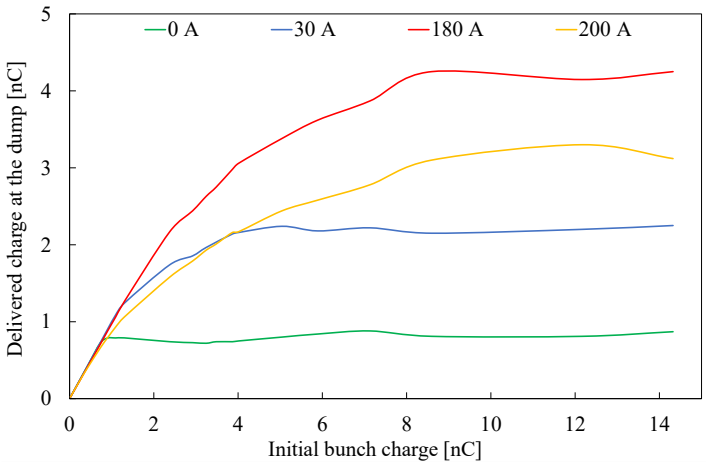

FIG. 112: Charge collected at the dump vs bunch charge from the modified gun for 0 A, 30 A, 180 A, and 200 A (300 kV, 50 kHz, 75 ps (FWHM), 1.2 mm (rms)).

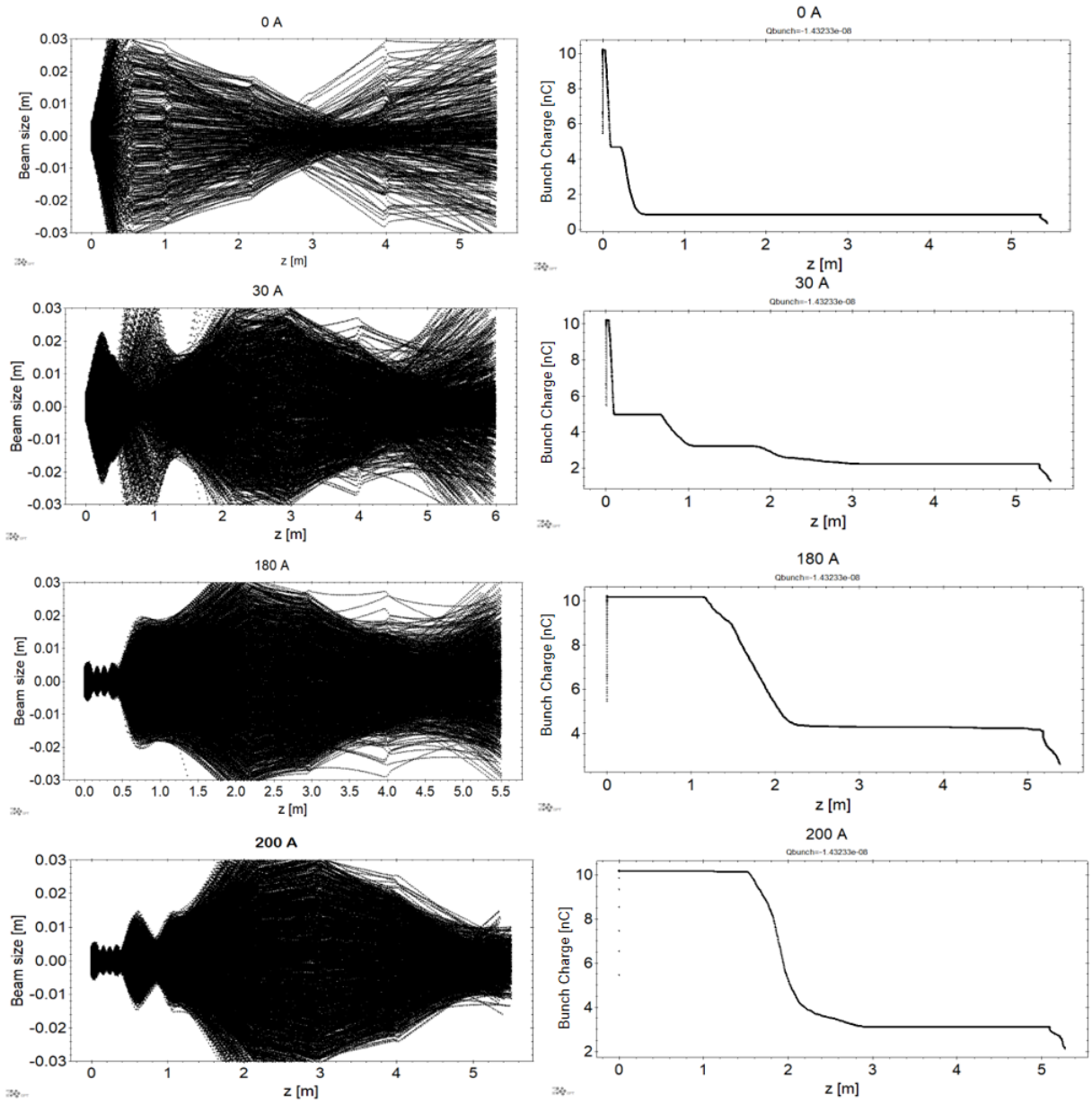

FIG. 113: Beam trajectory (left) and beam loss along the beamline (right) for 0 A, 30 A, 180 A, and 200 A.

FIG. 114: Flat cathode front (left) and flat anode plate mounted on to the outer flange (right).

FIG. 115: Anode assembly and thin NEG stripes at the bottom of the gun chamber.

FIG. 116: Image of the modified cathode electrode front (left) and back (right).

The following approach explores whether the electric field reform that occurred due to the anode shift would be replicated by tilting the anode. As demonstrated in Fig. 117, first, the anode was tilted for a few degrees left and right with respect to the y axis and ran CST simulation to obtain the electric field distributions for each case. Next, those field maps were used in GPT to do the beamline simulations.

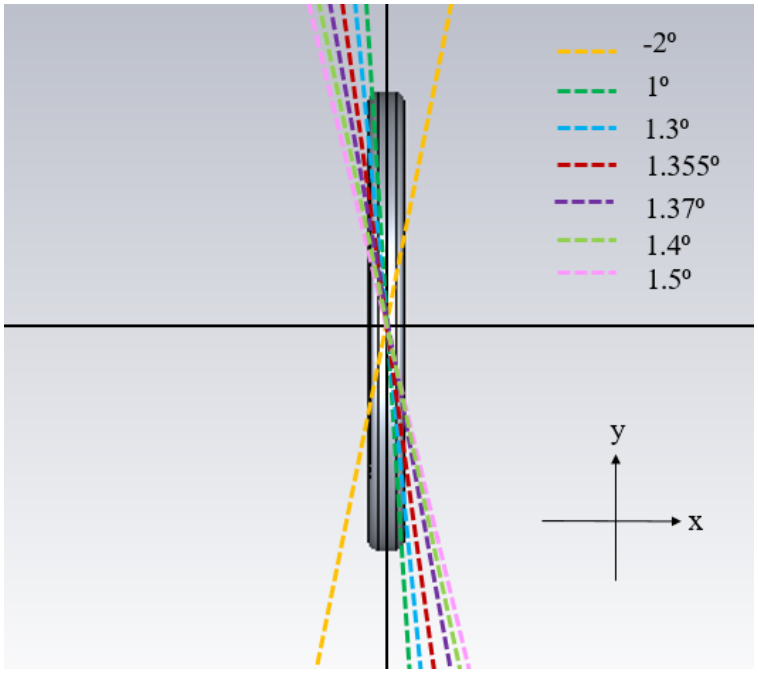

FIG. 117: Illustration of anode tilted angles.

Figure 118 shows how the beam deflects with the tilt in x (left) and in y (right). The left plot shows no effect on beam trajectory in the horizontal direction due to the tilt. However, the right plot shows that the beam trajectory is very sensitive to anode tilt and comes on axis when the tilt is 1.355°. Figure 119 shows a closer look at how the beam deflects with different anode tilts. Especially compared to 0°, a 1.355° makes a huge difference to the beam trajectory.

Figure 120 illustrates how normalized emittance left in x and right in y-directions. When

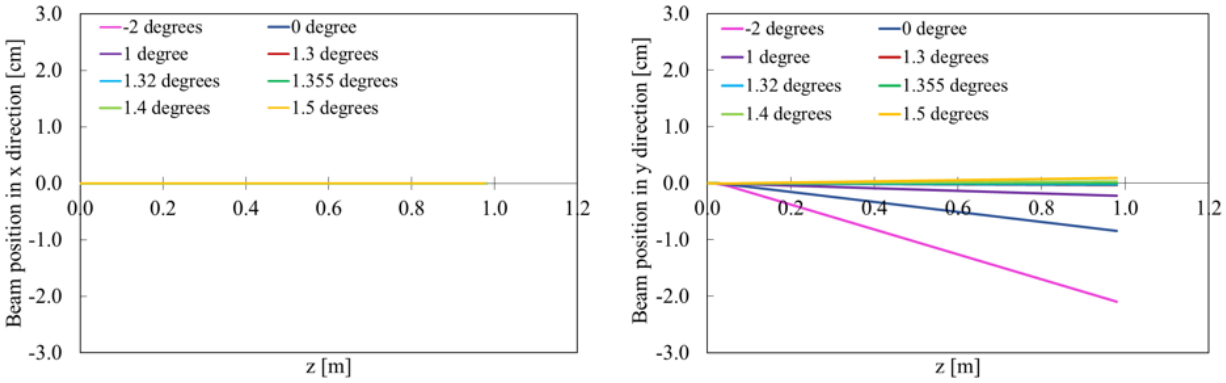

FIG. 118: Beam deflection varies with anode tilt x-deflection (left). y-deflection (right).

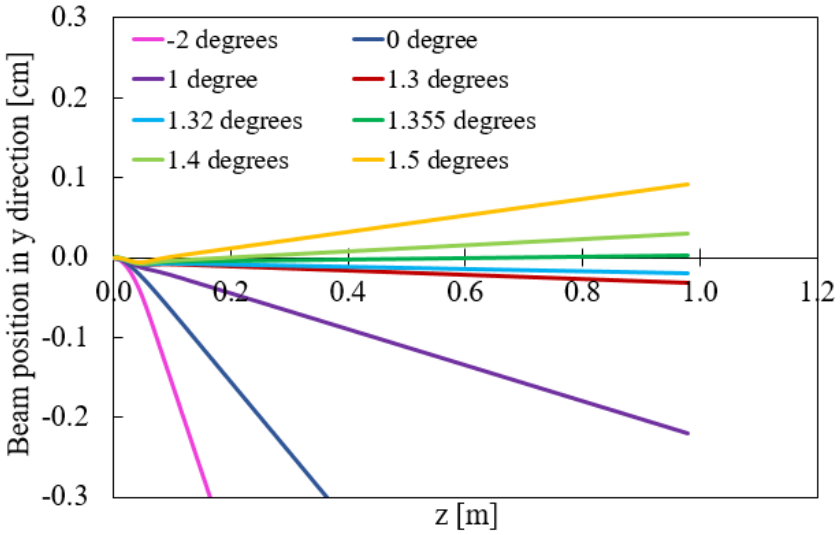

FIG. 119: Closer look of the vertical deflection with the tilt.

the beam is on-axis, both x and y normalized emittance reached the same value per the theory. Figure 121 shows the CST model of the 1.355° titled anode without its mounting flange.

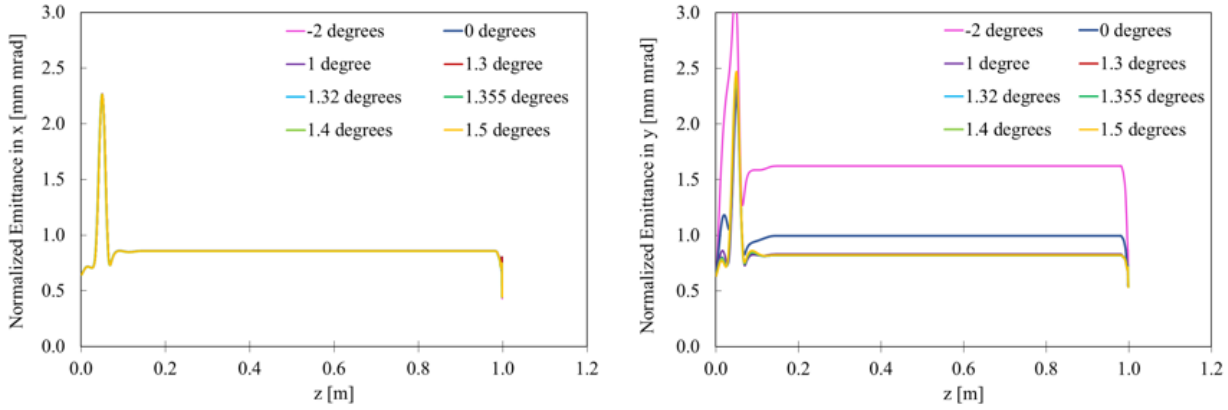

FIG. 120: Normalized emittance variation with the anode tilt x (left) and y (right).

Figure 122 illustrates how the electric field is distributed inside the gun chamber when the cathode is biased at 350 kV, and the anode is biased at 0 V. This design also managed to maintain ∼-10 MV/m limit everywhere inside the chamber. Anode edge shows higher electric field strength, but it will not trigger field emission since it is biased at 0 V. Figure 123 shows how potential is distributed inside the gun chamber when the cathode is biased at 350 kV anode is biased at 0 V.

The horizontal (left) and vertical (right) electric field variations between the anode-cathode gap of the modified gun are illustrated in Fig. 124. The color map (top left graph) shows the E_x distribution within the anode-cathode gap, and the bottom left graph shows the magnitude of E_x along each of the colored dotted lines shown on the field map. The top right graph and the bottom right graph show the same for E_y. In both, the vertical position of each dotted line is indicated with respect to the axis. According to the left plots, the E_x is symmetric along the axis, but right plots show that E_y is distorted first due to the inverted insulator and triple point junction screening electrode and then due to the titled anode.

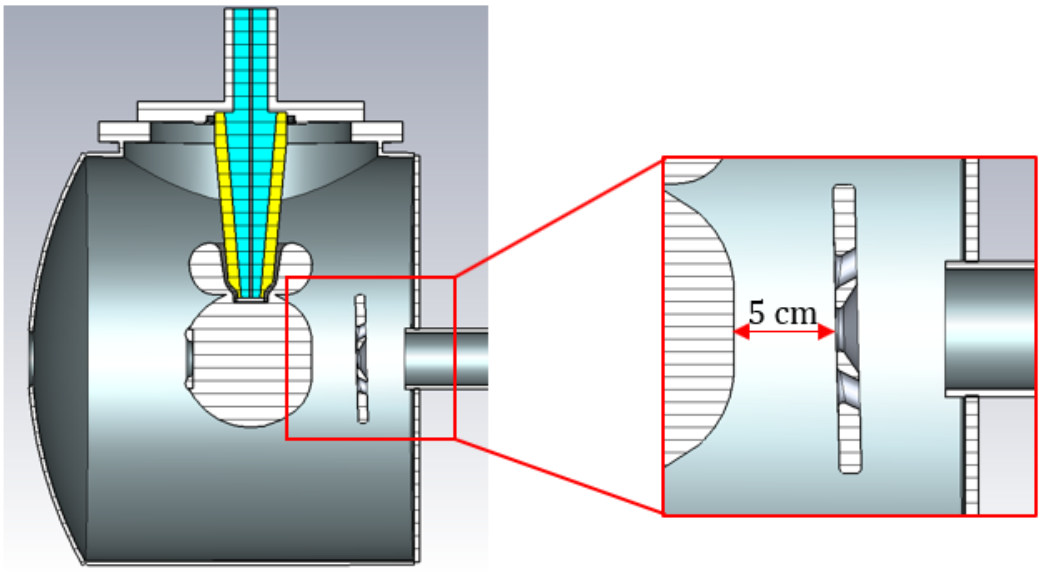

FIG. 121: CST design with the 1.355° tilted anode.

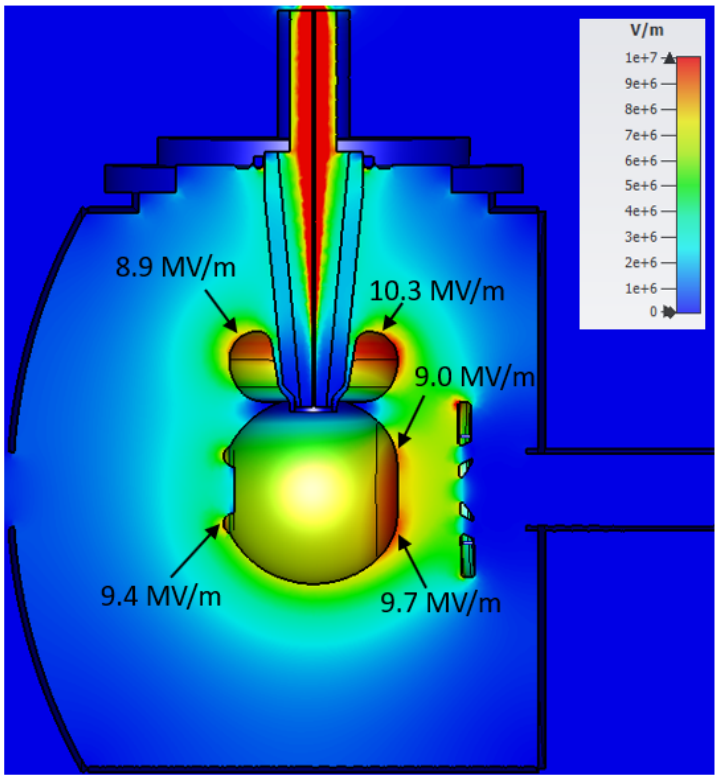

FIG. 122: Electric field distribution inside the gun chamber when cathode is biased at 350 kV and anode is biased at 0 V. The color represents the electric field strength in V/m.

Figure 125 shows the beam trajectories (left) in the x-direction and (right) in the y-directions. With the tilted anode beam in on-axis in both directions. This tilting anode would be an easy fix for an existing photo-gun with a similar design and similar issues than making a new anode with shifted anode hole.

FIG. 123: Potential variation inside the gun chamber when cathode is biased at 350 kV and anode is biased at 0 V. The color represents the potential in V.

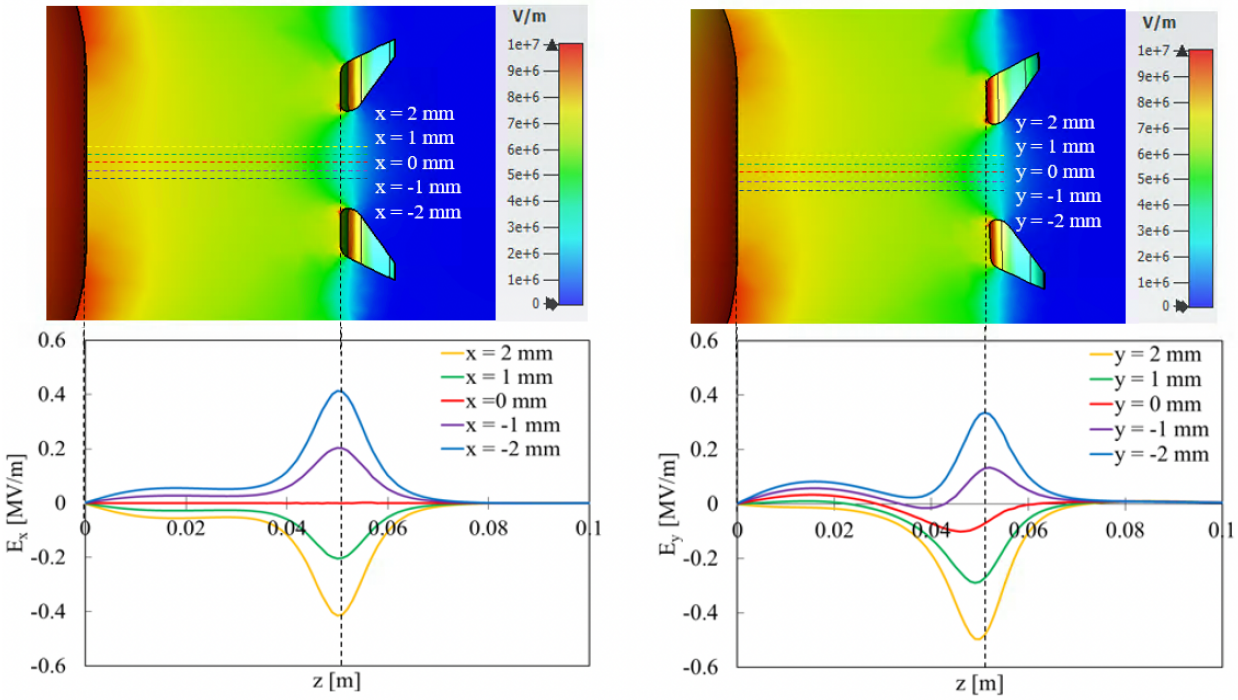

FIG. 124: E_x (left), E_y (right) variations along the dotted colored lines between the anode cathode gap when biased at 350 kV where each color line position is indicated with respect to the x axis (left) and y axis (right). The color represents the electric field strength in V/m.

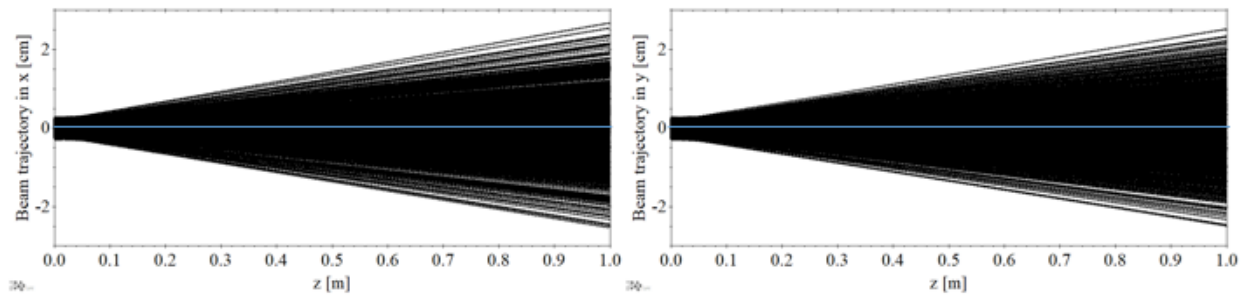

FIG. 125: Beam trajectory x (left) and y (right) directions with the tilted anode.

CHAPTER 8

CONCLUSIONS

The first part of the thesis presents the generation, characterization, and simulation of the magnetized bunch electron beam initiated as a part of the JLEIC magnetized electron cooler project to obtain the required ultra-high luminosity. A high current, high bunch charge magnetized electron source was successfully developed and commissioned at Thomas Jefferson National Accelerator Facility's Gun Test Stand using a new compact 300 kV DC high voltage photo-gun with an inverted insulator geometry and alkali-antimonide photocathode immersed in a magnetic field.

The magnetized electron beam was successfully characterized on beam size variations, rotation angle variations as a function of the magnetic field at the photocathode. Beam size variations with the cathode solenoid field showed an oscillatory behavior known as the "mismatch oscillation", which occurs due to the non-uniform magnetic field. This also affected the rotation angle to become a large angle for some cathode solenoid fields. Further, the emittance associated with the magnetized electron beam was studied and measured as a function of the magnetic field at the photocathode, laser spot size, and gun high voltage. Although beam loss at the higher magnetic field strengths prevented us from reaching the desired emittance values, the trend agreed with the theory.

A sustained high average current magnetized beam up to 28 mA was demonstrated for a cathode magnetic field 568 G with a cumulative extracted charge of 5 kC and an estimated 1/e charge lifetime of 9.4 kC. The superior thermal conductivity of the Mo substrate improved charge lifetime over the same photocathode grown on a GaAs wafer substrate. Further, this study showed that the applied magnetic field prevents arcing and stops beamline ions from entering the gun and contributes to the decay of the photocathode. High bunch charge magnetized beams up to 0.7 nC at 50 kHz repetition rate were also successfully generated, with space charge limitations and significant beam loss. Table 13 summarizes the initial goals and what we have achieved through this research project.

The beamline was successfully modeled using ASTRA and GPT software by employing the electric field map of the photo-gun generated using CST Studio Suite's electromagnetic field solver and magnetic field map of the cathode solenoid generated using Opera software.

TABLE 13: Magnetized electron beam requirements and demonstrated results.

Parameter	JLEIC requirement	Demonstrated
Magnetic field at the cathode [kG]	0.5	1.5
Bunch length [ps]	60 (Flat top)	25-60 (Gaussian rms)
Repetition rate [MHz]	43.3	100 – 374.3
Laser spot radius [mm]	3.1 (Flat top)	1.4 mm (Gaussian rms)
Normalized drift emittance [mm mrad]	36	26
Transverse normalized emittance [mm mrad]	<19	<2
Average current [mA]	140 (400 kV)	28 (50 ps (FWHM), 74.8 pC, 374.25 MHz, 100 kV, 0.57 kG)
Bunch charge [nC]	3.2	0.7 (75 ps (FWHM), 25 kHz, 225 kV, 0.76 kG)

MATLAB software was used as the post-processing tool. Simulations showed a good agreement with the beam size, rotation angle, and emittance measurements. Further, it verified the conservation of canonical angular momentum. These simulation tools were convenient in explaining the mismatch oscillations, larger rotation angles, and the difference between the correlated and uncorrelated emittances. Further, the importance of the photocathode position inside the cathode electrode was discovered while bench-marking the simulations against the beam size measurements. Experimentally this can affect the E_z at the photocathode, focusing inside the gun chamber hence poor beam quality.

The second part of the thesis focuses on the space charge effect in the magnetized electron beam. A new laser source was installed specifically for this experiment to deliver nC bunch charge (high power and varying repetition rate up to 50 kHz) with a low average current. Measurements were taken by varying the laser power and tracking the average current at the dump for different cathode solenoid currents. Further, these measurements were repeated for different gun high voltages, laser spot sizes, and laser pulse widths. GPT simulation was performed for all measurements. Both measurements and simulation showed a little notable effect of magnetization on space charge current limitation. In addition, both agreed that the space charges current limitation can be reduced by using a higher gun voltage with a larger laser spot size at the cathode and longer pulse width, regardless of the beam being magnetized. The limited beamline aperture and insufficient strength of the focusing solenoids caused significant beam loss. GPT simulation indicated that more beams could be extracted with magnetized beam than the non-magnetized beam because of the cathode solenoid focusing. Further, simulations provided evidence that the beam loss also depends on the cathode solenoid current due to the mismatch oscillation. This study significantly contributes to high bunch charge magnetized beam applications to optimize their parameters for better results.

The low extracted charge is mainly due to the modest longitudinal electric field (E_z) at the photocathode as well as beam loss. Thus, to reach the few nC high bunch charge goal, the existing DC photo-gun was modified to obtain a higher E_z at the cathode for high bunch charge operations while keeping the beam centered using CST Studio Suite's electromagnetic field solver. It has increased E_z up to -7.8 MV/m from -2.5 MV/m by removing the Pierce geometry and decreasing the anode-cathode gap to 5 cm from 9 cm. A simple way to eliminate the beam deflection exerted by the non-symmetric nature of the inverted insulator photo-gun was discovered just by lowering the anode aperture by -1.6 mm. This will be a massive advantage for all the photo-guns, including CEBAF with

inverted insulator geometry, to minimize the beam loss at the exit of the anode. Further, the charge extracted from the cathode increased with the modified gun (from 4.6 nC to 10.2 nC for the maximum initial bunch charge). This beam deflection can also be corrected by tilting the anode.

8.1 SUMMARY

According to our limited data, the magnetization does not affect the space charge current limitation, which concludes that the charge extracted from the photocathode cannot be increased or decreased by using a magnetized electron beam. Further, a magnetized beam behaves the same way as a non-magnetized beam: charge extracted increases with higher gun voltage, larger beam spot size at the cathode, and long pulse width, which points that these parameters can be optimized for magnetized beam the same way as the non-magnetized beam for better results. Additionally, beam focusing, in addition to the magnetization, leads to less beam loss and delivers a higher average current than the non-magnetized beam.

Overall, this project provides insights and challenges associated with developing the magnetized electron source with a high average current and high bunch charge for the EIC cooler design and other magnetized beam applications.

8.2 FUTURE WORK

Future work on this project mainly involves the delivery of high bunch charge (a few nC) with a modified photo-gun. The modified cathode front plate, anode with shifted aperture, and anode mounting have been already made and polished to mirror-like condition with sandpapers, diamond paste, and finally with barrel polishing. Currently, the gun has been assembled in the vacuum room with brand new GaAs and Mo photocathodes. The next step is to modify the beamline by removing and replacing some of the components that have a small aperture that causes huge beam loss and install a Faraday cup at the exit of the gun to measure the average current and thus the bunch charge extracted from the photocathode before the beam loss.

The next objective is to use the photo-gun and the beamline to explore different photocathode compounds, substrates, and photocathode cooling techniques to improve operational lifetime.

Another focus is to model the CEBAF photo-gun with shifted anode and tilted anode to decide which method is more suitable to cancel its beam deflection while preserving the best beam quality.

BIBLIOGRAPHY

[1] T. Feder, "Brookhaven facility to be transformed into electron–ion collider," Phys. Today **73**, 22–25 (2020), https://doi.org/10.1063/PT.3.4427 .

[2] W. Herr and B. Muratori, "Concept of luminosity," in *CERN Accelerator School and DESY Zeuthen: Accelerator Physics* (2003).

[3] S. Nagaitsev, "EIC hadron beam cooling," (2019), unpublished.

[4] G. I. Budker, "Efficient method for damping of particle oscillations in proton and antiproton storage ring," Atomnaya Energiya **22** (1967).

[5] V. V. Parkhomchuk and A. N. Skrinsky, "Electron cooling: physics and prospective applications," **54**, 919–947 (1991).

[6] S. Nagaitsev, D. Broemmelsiek, A. Burov, K. Carlson, C. Gattuso, M. Hu, T. Kroc, L. Prost, S. Pruss, M. Sutherland, C. W. Schmidt, A. Shemyakin, V. Tupikov, A. Warner, G. Kazakevich, and S. Seletskiy, "Experimental demonstration of relativistic electron cooling," Phys. Rev. Lett. **96**, 044801 (2006).

[7] A. V. Fedotov, Z. Altinbas, S. Belomestnykh, I. Ben-Zvi, M. Blaskiewicz, M. Brennan, D. Bruno, C. Brutus, M. Costanzo, A. Drees, W. Fischer, J. Fite, M. Gaowei, D. Gassner, X. Gu, J. Halinski, K. Hamdi, L. Hammons, M. Harvey, T. Hayes, R. Hulsart, P. Inacker, J. Jamilkowski, Y. Jing, J. Kewisch, P. Kankiya, D. Kayran, R. Lehn, C. J. Liaw, V. Litvinenko, C. Liu, J. Ma, G. Mahler, M. Mapes, A. Marusic, K. Mernick, C. Mi, R. Michnoff, T. Miller, M. Minty, G. Narayan, S. Nayak, L. Nguyen, M. Paniccia, I. Pinayev, S. Polizzo, V. Ptitsyn, T. Rao, G. Robert-Demolaize, T. Roser, J. Sandberg, V. Schoefer, C. Schultheiss, S. Seletskiy, F. Severino, T. Shrey, L. Smart, K. Smith, H. Song, A. Sukhanov, R. Than, P. Thieberger, S. Trabocchi, J. Tuozzolo, P. Wanderer, E. Wang, G. Wang, D. Weiss, B. Xiao, T. Xin, W. Xu, A. Zaltsman, H. Zhao, and Z. Zhao, "Experimental demonstration of hadron beam cooling using radio-frequency accelerated electron bunches," Phys. Rev. Lett. **124**, 084801 (2020).

[8] Y. Derbenev, "Theory of electron cooling," (2017), arXiv:1703.09735 .

[9] Y. Derbenev and A. N. Skrinskii, "Magnetization effects in electron cooling," Sov. J. Plasma Phys. **4**, 273–278 (1978).

[10] M. A. Al Mamun, P. A. Adderley, J. F. Benesch, B. Bullard, J. R. Delayen, J. M. Grames, J. Guo, F. E. Hannon, J. C. Hansknecht, C. Hernandez-Garcia, R. Kazimi, G. A. Krafft, M. Poelker, R. S. Suleiman, M. G. Tiefenback, Y. Wang, S. Zhang, and S. Wijethunga, "Production of magnetized electron beam from a DC high voltage photogun," in *9th International Particle Accelerator Conference, Vancouver, BC, Canada* (2018).

[11] A. Halavanau, P. Piot, D. Edstrom Jr., and A. Romanov, "Magnetized and flat beam generation at the Fermilab's FAST facility," in *9th International Particle Accelerator Conference, Vancouver, BC, Canada* (2018).

[12] A. Romanov, C. Baffes, D. Broemmelsiek, Darren Crawford, N. Eddy, Jr Edstrom, E. Harms, J. Hurd, M. Kucera, J. Leibfritz, I. Rakhno, J. Reid, Jiafeng Ruan, James Santucci, Vladimir Shiltsev, Giulio Stancari, R. Thurman-Keup, A. Valishev, and Arden Warner, "Commissioning and operation of FAST electron linac at Fermilab," in *9th International Particle Accelerator Conference, Vancouver, BC, Canada* (2018) arXiv:1811.04027 [physics.acc-ph] .

[13] Y.-E Sun, P. Piot, K.-J. Kim, N. Barov, S. Lidia, J. Santucci, R. Tikhoplav, and J. Wennerberg, "Generation of angular-momentum-dominated electron beams from a photoinjector," Phys. Rev. ST Accel. Beams **7**, 123501 (2004).

[14] J. Smedley and M. Poelker, "USPAS course on photocathode physics," (2011).

[15] B. Dunham, J. Barley, A. Bartnik, I. Bazarov, L. Cultrera, J. Dobbins, G. Hoffstaetter, B. Johnson, R. Kaplan, S. Karkare, V. Kostroun, Y. Li, M. Liepe, X. Liu, F. Loehl, J. Maxson, P. Quigley, J. Reilly, D. Rice, D. Sabol, E. Smith, K. Smolenski, M. Tigner, V. Vesherevich, D. Widger, and Z. Zhao, "Record high-average current from a high-brightness photoinjector," Appl. Phys. Lett. **102**, 034105 (2013).

[16] X. Gu, Z. Altinbas, S. Badea, D. Bruno, L. Cannizzo, M. Costanzo, A. Drees, A. V. Fedotov, W. Fischer, D. Gassner, M. Gaowei, P. Inacker, J. Jamilkowski, D. Kayran, J. Kewisch, C. J. Liaw, C. Liu, M. Mapes, K. Mernick, C. Mi, T. A. Miller, M. Minty, L. Nguyen, V. Ptitsyn, J. Sandberg, V. Schoefer, S. Seletskiy, L. Smart, A. Sukhanov, P. Thieberger, J. Tuozzolo, E. Wang, A. Zaltsman, He Zhao, Zhi Zhao, A. Bartnik, and K. Smolenski, "Stable operation of a high-voltage high-current DC photoemission gun for the bunched beam electron cooler in RHIC," Phys. Rev. Accel. Beams **23**, 013401 (2020).

[17] M. A. Mamun, A. Elmustafa, M. Stutzman, P. Adderley, and M. Poelker, "Effect of heat treatments and coatings on the out-gassing rate of stainless steel chambers," J. Vac. Sci. Technol. **32**, 021604 (2014).

[18] C. Hernandez-Garcia, P. Adderley, B. Bullard, J. Benesch, J. Grames, J. Gubeli, F. Hannon, J. Hansknecht, J. Jordan, R. Kazimi, G. A. Krafft, M. A. Mamun, M. Poelker, M. L. Stutzman, R. Suleiman, M. Tiefenback, Y. Wang, S. Zhang, H. Baumgart, G. Palacios-Serrano, S. Wijethunga, J. Yoskowitz, C. A. Valerio Lizarraga, R. Montoya Soto, and A. Canales Ramos, "Compact −300 kV DC inverted insulator photogun with biased anode and alkali-antimonide photocathode," Phys. Rev. Accel. Beams **22**, 113401 (2019).

[19] C. Hernandez-Garcia, D. Bullard, F. Hannon, Y. Wang, and M. Poelker, "High voltage performance of a DC photoemission electron gun with centrifugal barrel-polished electrodes," Rev. Sci. Instrum. **88**, 093303 (2017).

[20] C. Hernandes-Garcia, "GTS 600 kV gas insulated power supply maintenance and safety," (2017), Jefferson Lab Operational Safety Procedure.

[21] Y. Wang, M. A. Mamun, P. Adderley, B. Bullard, J. Grames, J. Hansknecht, C. Hernandez-Garcia, R. Kazimi, G. A. Krafft, G. Palacios-Serrano, M. Poelker, M. L. Stutzman, R. Suleiman, M. Tiefenback, S. Wijethunga, J. Yoskowitz, and S. Zhang, "Thermal emittance and lifetime of alkali-antimonide photocathodes grown on GaAs and molybdenum substrates evaluated in a −300 kV DC photogun," Phys. Rev. Accel. Beams **23**, 103401 (2020).

[22] R. R. Mammei, R. Suleiman, J. Feingold, P. A. Adderley, J. Clark, S. Covert, J. Grames, J. Hansknecht, D. Machie, M. Poelker, T. Rao, J. Smedley, J. Walsh, J. L. McCarter, and M. Ruiz-Osés, "Charge lifetime measurements at high average current using a CsK_2Sb photocathode inside a DC high voltage photogun," Phys. Rev. ST Accel. Beams **16**, 033401 (2013).

[23] J. Benesch D. Bullard J. Grames J. Guo F. Hannon-J. Hansknecht C. Hernandez-Garcia R. Kazimi G. Krafft1 M. A. Mamun M. Poelker R. Suleiman M. Tiefenback S. Zhang, P. Adderley and Y. Wang, "High current high charge magnetized and bunched electron beam from a DC photogun for JLEIC cooler," in *10^{th} International Particle Accelerator Conference, Melbourne, Australia* (2019).

[24] *Spiricon Laser Beam Diagnostics*, https://www.ophiropt.com/user_files/laser/beam_profilers/lbausbuser.pdf.

[25] H. Wiedemann, *Particle Accelerator Physics*, 4th ed. (Springer, Switzerland, 2015).

[26] G. A. Krafft, "Accelerator physics," (2021), unpublished.

[27] K. Flöttmann, "Some basic features of the beam emittance," Phys. Rev. ST Accel. Beams **6**, 034202 (2003).

[28] I. V. Bazarov, B. M. Dunham, Y. Li, X. Liu, D. G. Ouzounov, C. K. Sinclair, F. Hannon, and T. Miyajima, "Thermal emittance and response time measurements of negative electron affinity photocathodes," J. Appl. Phys. **103**, 054901 (2008).

[29] T. Melkumyan, "Transverse beam emittance measurement via solenoid scan," (2017), unpublished.

[30] A. T. Green, *Development of a python-based emittance calculator at Fermilab science technology (FAST) facility*, Master's thesis, Northern Illinois U. (2016).

[31] R. Li, "Discussion of phase space and emittances," (2016), unpublished.

[32] V. Kumar, "Understanding the focusing of charged particle beams in a solenoid magnetic field," Am. J. Phys. **77**, 737 (2009).

[33] M. Reiser, *Theory and Design of Charged Particle Beams* (Wiley-VCH, Weinheim, 2007).

[34] D. H. Dowell, "Sources of emittance in rf photocathode injectors: intrinsic emittance, space charge forces due to non-uniformities, rf and solenoid effects," (2016), arXiv:1610.01242 [physics.acc-ph] .

[35] F. Hannon and M. Stefani, "Transverse uncorrelated emittance diagnostic for magnetized electron beams," Phys. Rev. Accel. Beams **22**, 102801 (2019).

[36] M. Ferrario, M. Migliorati, and L. Palumbo, "Space charge effects," Proceedings of the CAS-CERN Accelerator School, Geneva (2014).

[37] I. Langmuir, "The effect of space charge and residual gases on thermionic currents in high vacuum," Phys. Rev. **2**, 450–486 (1913).

[38] Y. Y. Lau, "Simple theory for the two-dimensional Child-Langmuir law," Phys. Rev. Lett. **87**, 278301 (2001).

[39] L. K. Ang and P. Zhang, "Ultrashort-pulse Child-Langmuir law in the quantum and relativistic regimes," Phys. Rev. Lett. **98**, 164802 (2007).

[40] Y. Feng and J. P. Verboncoeur, "Transition from Fowler-Nordheim field emission to space charge limited current density," Phys. Plasmas **13**, 073105 (2006), https://doi.org/10.1063/1.2226977 .

[41] *MATLAB*, `https://www.mathworks.com/products/matlab.html`.

[42] F.E. Hannon G.A. Krafft J. Benesch R. Suleiman M. Poelker-J.R. Delayen S.A.K. Wijethunga, M.A. Mamun, "Simulation study of the magnetized electron beam," in *9^{th} International Particle Accelerator Conference, Vancouver, BC, Canada* (2018).

[43] K. Flöttmann, *A Space Charge Tracking Algorithm (ASTRA).*

[44] S.B. Van Der Geer and M.J. de Loos, *General Particle Tracer (GPT).*

[45] `https://root.cern/`.

[46] G. A. Krafft M. A. Mamun R. Suleiman M. Poelker S. Zhang J. Benesch S. A. K. Wijethunga, J. R. Delayen, "Space charge effect in low energy magnetized electron beam," in *12^{th} International Particle Accelerator Conference, Campinas, SP, Brazil* (2021).

[47] P. Adderley, J. Clark, J. Grames, J. Hansknecht, K. Surles-Law, D. Machie, M. Poelker, M. Stutzman, and R. Suleiman, "Load-locked DC high voltage GaAs photogun with an inverted-geometry ceramic insulator," Phys. Rev. ST Accel. Beams **13**, 10101 (2009).

[48] G. Palacios-Serrano, F. Hannon, C. Hernandez-Garcia, M. Poelker, and H. Baumgart, "Electrostatic design and conditioning of a triple point junction shield for a 200 kV DC high voltage photogun," Rev. Sci. Instrum. **89**, 104703 (2018), https://doi.org/10.1063/1.5048700 .

[49] N. Nishimori, R. Nagai, S. Matsuba, R. Hajima, M. Yamamoto, Y. Honda, T. Miyajima, H. Iijima, M. Kuriki, and M. Kuwahara, "Experimental investigation of an optimum configuration for a high-voltage photoemission gun for operation at 500 kV," Phys. Rev. ST Accel. Beams **17**, 053401 (2014).

[50] C. Hernandez-Garcia, M. Poelker, and J. Hansknecht, "High voltage studies of inverted-geometry ceramic insulators for a 350 kV DC polarized electron gun," IEEE Trans. Dielectr. Electr. Insul. **23**, 418–427 (2016).

[51] *CST Microwave Studio*, `https://www.3ds.com/products-services/simulia/products/cst-studio-suite`.

[52] B. Bullard J. Benesch J. Grames F. Hannon C. Hernandez-Garcia J. Hansknecht G. Krafft R. Kazimi M. Poelker M. A. Mamun R. Suleiman G. Palacios M. Tiefenback Y. Wang, P. Adderley and S. Zhang, "300 kV DC high voltage photogun with inverted insulator geometry and CsK_2Sb photocathode," in *9^{th} International Particle Accelerator Conference, Vancouver, BC, Canada* (2018).

[53] I. V. Bazarov, B. M. Dunham, and C. K. Sinclair, "Maximum achievable beam brightness from photoinjectors," Phys. Rev. Lett. **102**, 104801 (2009).

APPENDIX A

DIGITIZING THE WEIGHTED LASER PROFILE

GPT can implement a gray-scale bitmap image of the laser profile as the initial particle distribution using the "SetXYdistbmp" command. Each image pixel is treated as a rectangular surface area with a uniformly distributed chance of emitting particles, given by the pixel color. Black pixels have zero chance of emitting particles, white pixels have the maximum chance, and gray-scale values are linearly interpolated in between. Since our QE profiles are also not uniform and decayed over time, the weighted laser profile was generated by mapping with QE profile onto the laser profile and normalizing it. Following is the pseudo-code for digitizing the weighted laser image.

- Save the .cma file of the laser from Spiricon software and convert it to a gray-scale matrix.
- Find the pixel to mm ratio and the center of the laser profile from the Spiricon software.
- Reduce the matrix such that the center of the matrix aligns with the center of the laser profile so later it can be aligned with the center of the QE matrix.
- Since the laser hits the photocathode with an angle of 25° in the horizontal direction, the aspect ratio of the matrix has to be changed such that,

$$\frac{dx}{dy} = \frac{x/\cos 25^\circ}{y}. \tag{133}$$

- The QE scan gives a table with x, y, and intensity. Plot a surface plot with the above table and save it as an image.
- Convert this saved image to a matrix to obtain the pixel to mm ratio.
- Reduce the matrix such that the center of the QE scan is the center of the image.
- MATLAB reads this as an RGB image, and the matrix comes as three matrices corresponding to the red, green, and blue. Thus, re-scale that three matrices separately to match the pixel to mm ratio of the laser matrix.

- Resize three matrices to match the size of the laser matrix such that only the area in the QE scan where laser hits remain.
- Concatenate the three matrices and convert them to gray-scale.
- Multiply the laser matrix and QE matrix by point by point method and normalized to 1.
- Convert the matrix into an 8-bit gray-scale image.

APPENDIX B

CST MODELLING OF THE PHOTO-GUN

CST Studio Suite's electromagnetic field solver is a fully featured software package for electromagnetic analysis and design electrostatic, magneto-static, stationary current, and low-frequency devices. Following is the CST procedure used to re-design the photo-gun.

- Import the simplified 3D photo-gun model designed using Solidworks software to CST.
- Remove the Pierce geometry and modified the cathode front plate and anode plate using modeling tools and shapes.
- Select the appropriate material for each component, *i.e.*, Perfect Electrical Conductor (PEC) for all metal components, non-conducting material with corresponding ϵ and σ for the insulator, and rest is the vacuum.
- Divide the model into separate mesh groups according to its importance in the sensitivity of the EM fields (*i.e.*, the minimum step width at the cathode front face, for the vacuum between the anode-cathode gap, triple point junction).
- Set up the background material (*i.e.*, vacuum).
- Set up the boundaries.
- Set up the potential in each component (*i.e.*, Cathode 350 kV, Anode 0 V or 1 kV, and everywhere else also 0 V).
- Use a low-frequency solver with reasonable accuracy to obtain the EM fields.
- Use CST post-processing tool to export the 3D field map of the photo-gun.

VITA

W. M. Sajini Anushika Kumari Wijethunga
Department of Physics
Old Dominion University
Norfolk, VA 23529

EDUCATION:

- 2017-2021 Ph.D. Candidate (Physics), Old Dominion University, Norfolk, Virginia, USA
- 2017 Master of Science (Physics), Old Dominion University, Norfolk, Virginia, USA
- 2015 Bachelor of Science (Physics), University of Peradeniya, Sri Lanka

AWARDS:

- Jefferson Science Associates graduate fellowship for the year 2019-2020

RECENT PUBLICATIONS:

- S.A.K. Wijethunga, *et. al.*, "Space charge effect in low energy magnetized electron beam", in Proceedings of International Particle Accelerator Conference virtual edition, Campinas, Brazil (2021).
- S.A.K. Wijethunga, *et. al.*, "Re-design of the Jefferson Lab 300 kV DC high voltage photo-gun for high bunch charge operations", in Proceedings of International Particle Accelerator Conference virtual edition, Campinas, Brazil (2021).
- Y. Wang, S.A.K. Wijethunga, *et. al.*, "Thermal emittance and lifetime of alkali-antimonide photocathodes grown on GaAs and Mo substrates evaluated in a 300 kV DC photo-gun", Phys. Rev. Accel. Beams 23, 103401 (2020).
- C. Hernandez-Garcia, S.A.K. Wijethunga, *et. al.*, "Compact 300 kV a DC inverted insulator photo-gun with biased anode and alkali-antimonide photocathode", Phys. Rev. Accel. Beams 22, 113401 (2019).

Typeset using LaTeX.